

**Development of Self-Powered Wireless Structural Health
Monitoring (SHM) for Wind Turbine Blades**

**A THESIS
SUBMITTED TO THE FACULTY OF THE GRADUATE SCHOOL
OF THE UNIVERSITY OF MINNESOTA
BY**

Dong-Won Lim

**IN PARTIAL FULFILLMENT OF THE REQUIREMENTS
FOR THE DEGREE OF
DOCTOR OF PHILOSOPHY**

Professor Susan C. Mantell and Professor Peter J. Seiler

January, 2015

© Dong-Won Lim 2015
ALL RIGHTS RESERVED

Acknowledgements

First, I would like to extend my sincere gratitude to my advisers Prof. Susan Mantell and Prof. Peter Seiler for allowing me to grow as a research scientist and for supporting my research. Without their guidance, I would never have even been able to finish my dissertation. I would also like to thank Prof. Kim Stelson and Prof. Rusen Yang. They have always been willing to listen to my problems and help. I am grateful to all committee members for letting my defense be an enjoyable moment and for their insightful comments.

I have been fortunate to work with Prof. Frank Kelso, with whom I taught various classes. He envisioned better teaching from the research. Working with him has been an invaluable experience for me. His patient listening and advising made my research burden light. I am indebted to Prof. Henryk Stolarski for his advice and finite element code which enhanced my research. I would like to thank Prof. Yang and Ren Zhu for helping my experimental work forward. I am obliged to all lab mates and colleagues for providing a cheerful and supportive environment. In particular, I would like to thank Hanxiao Ge and Dr. Adam Gladen, who are not only excellent researchers but also good friends.

Last, but never least, I want to express special thanks to my wife Chahee and my family for their love over the years. Her daily lunch box was not only just a meal for the day, but also the vibrant encouragement for me to move on. Her thoughtful consideration and faithful support made me finish my research. And happy smiles from my children Joonsop and Joonhee gave me a source of energy for the day. Thanks to my parents, who have been consistently supporting me in many respects. They have been joyful for my little achievement.

Abstract

Wind turbine blade failure can lead to unexpected power interruptions. Monitoring wind turbine blades is important to ensure seamless electricity delivery from power generation to consumers. Structural health monitoring (SHM) enables early recognition of structural problems so that the safety and reliability of operation can be enhanced. This dissertation focuses on the development of a wireless SHM system for wind turbine blades.

Wireless SHM is uniquely appropriate for wind turbine blades. The sensor is comprised of a piezoelectric energy harvester (EH) and a telemetry unit. The sensor node is mounted on the blade surface. As the blade rotates, the blade flexes, and the energy harvester captures the strain energy on the blade surface. Once sufficient electricity is captured, a pulse is sent from the sensing node to a gateway. Then, a central monitoring algorithm processes a series of pulses received from all three blades. This wireless SHM, which uses commercially available components, can be retrofitted to existing turbines.

The harvested energy for sensing can be estimated in terms of two factors: the available strain energy and conversion efficiency. The available strain energy was evaluated using the FAST (Fatigue, Aerodynamics, Structures, and Turbulence) simulator. Three typical sizes of wind turbines with three levels of turbulence intensity were simulated. Edgewise and flapwise strain over the blade span were calculated. For both cases, the maximum strain occurs at approximately half of the first modal frequency of blades ($< 1\text{Hz}$) and is located at a distance of $\sim 20\text{-}33\%$ of the blade length from the hub. The conversion efficiency was studied analytically and experimentally. An experimental set-up was designed to mimic the expected strain frequency and amplitude for rotor blades. From a series of experiments, the efficiency of a piezoelectric EH at a typical rotor speed (0.2 Hz) was approximately 0.5% . Even with the expected low strain energy amplitude level ($400\mu\text{-strain}$) and frequency (0.2Hz) and the limited EH efficiency (0.5%), the power requirement for sending one measurement ($280\ \mu\text{J}$) can be achieved in 10 minutes.

Designing a detection algorithm is challenging due to this low sampling rate. A new sensing approach—the timing of pulses from the transmitter—was introduced. This

pulse timing, which is tied to the charging time, is indicative of the structural health. The SHM system exploits the inherent triple redundancy of the three blades. The timing data of the three blades are compared to discern an outlier, corresponding to a damaged blade. This algorithm is based on an assumption that only one blade fails at the early stage of damage. Two types of post-processing of pulses were investigated: (1) comparing the ratios of signal timings (i.e. transmission ratio); and (2) comparing the difference between signal timings (i.e. residuals). For either method, damage is indicated when the energy ratio or residual exceeds a threshold level. When residuals are used to detect damage, performance measures such as the false alarm rate and detection probability can also be imposed.

The SHM algorithms were evaluated using strain energy data from a 2.5 MW wind turbine. For the transmission ratio algorithm a 10% threshold is required to detect a 20% loss of local stiffness. For the residual stochastic method, a 20-40% loss in stiffness can be detected with a 90% detection probability and 0.7% false alarming rate in approximately 50-200 days, where noise is estimated from raw strain data.

Contents

Acknowledgements	i
Abstract	ii
List of Tables	viii
List of Figures	ix
1 Introduction	1
1.1 Why is a wind turbine blade important?	2
1.1.1 Impact of Blade Reliability	2
1.1.2 Design with Composite Materials	3
1.1.3 Loading Conditions for Wind Turbine Blades	5
1.1.4 Restrictions on Sensing Approaches	6
1.2 Review of Current SHM Technologies	7
1.2.1 Existing SHM Methods	7
1.2.2 Wireless Sensor Network for SHM	8
1.3 Thesis Objectives	11
1.4 Thesis Contributions	12
2 Wind Turbine Blades as a Strain Energy Source for an EH	13
2.1 Summary	13
2.2 Introduction	13
2.3 Background	14
2.3.1 Sensors and Telemetry for SHM	14

2.3.2	Feasibility of Energy Harvesting	15
2.4	Methods	17
2.5	Results and Discussion	20
2.6	Conclusion	23
3	Efficiency of Energy Conversion for Low Broadband Excitation	26
3.1	Introduction	26
3.2	Model for EH efficiency	28
3.3	Estimating Input Energy	30
3.3.1	Harmonic Excitation	31
3.3.2	Random Excitation	32
3.4	Experiments for the Conversion Efficiency	32
3.4.1	Experiment Design and Set-up	33
3.5	Experimental Results	35
3.5.1	Harmonic Excitation	36
3.5.2	Random Excitation	37
3.6	Conclusions	39
4	Wireless SHM of Blades Using an EH as a Sensor	40
4.1	Summary	40
4.2	Introduction	41
4.3	Background	42
4.3.1	Health Monitoring of Wind Turbine Blades	42
4.3.2	Energy Harvester as a Sensor	43
4.3.3	Available Strain Energy	45
4.4	Approach	47
4.4.1	Damage Model	47
4.4.2	Triple Redundancy Fault Detection	49
4.5	Results and Discussion	52
4.5.1	Eolos Wind Turbine	52
4.5.2	Data Process using a Ratio Factor (Healthy Blades)	53
4.5.3	SHM Simulation for a Unhealthy Blade	54
4.6	Conclusion	55

5	Algorithm for the Wireless SHM of Blades Using EHs	57
5.1	Summary	57
5.2	Introduction	58
5.3	Overview of Wireless SHM System	60
5.4	SHM Design for Probabilistic Performance	64
5.4.1	Energy Harvester as a Sensor—Problem Set-up	64
5.4.2	Threshold Design	67
5.4.3	Probabilistic Analysis at the Decision Time, τ_d	70
5.5	Case Study: Application of SHM	73
5.5.1	Damage Model: Estimate Degradation Parameter g_D	73
5.5.2	Characterization of the strain data: \bar{B} and σ	76
5.5.3	Results	78
5.6	Summary and Conclusions	81
6	Conclusions & Future Work	85
7	References	89
Appendix A. Examples and Validation for Energy Harvesting		100
A.1	Examples of Input Energy Calculation	100
A.2	Validation of the Experiment Set-up	102
Appendix B. Strain Energy Estimation		106
B.1	Least Square Estimation	106
B.2	Propagation Error of Estimation	109
Appendix C. Monthly statistics for residuals		111
C.1	Statistics Results	111
Appendix D. Matlab Codes		118
D.1	Pulse Calculation (EH an Telemetry)	118
D.2	Strain Energy Estimation	120
D.3	Harvested EH Strain Energy Simulation	121
D.4	Eolos Strain Calibration	122

D.5	Eolos Strain Data Import	123
D.6	Strain Data Error Correction	125
D.7	Find Strain Residual Variance	128
D.8	Synthetic Damage Simulation for Eolos Data	132
D.9	SHM Design by Threshold and Decision Time	136

List of Tables

1.1	Failure rates, down time, and maintenance cost of wind turbine main components	4
1.2	Comparison of Sensors for Wireless SHM	9
2.1	Three Typical Wind Turbines Properties	18
2.2	Max. Strain of the NREL Offshore (5 MW)	22
2.3	Max. Strain of the CART3 (600 kW)	23
2.4	Max. Strain of the WindPACT (1.5 MW)	24
3.1	Energy Harvester Efficiency for Various Input Frequencies	37
5.1	Degradation Parameter g_D	76
C.1	Monthly σ and \bar{B} for the SHM system design	112

List of Figures

1.1	Increasing size of wind turbines over the last three decades is compared to a commercial jet airplane and an American football field at the same scale from [1].	5
1.2	EH-Link layout from the Lord Microstrain, Inc. [2]	10
2.1	Schematic showing (a) sensor nodes mounted on blade, (b) node with energy harvester and telemetry, and (c) data acquisition and health monitoring.	15
2.2	Blade Coordinate System (left) [3] and Cross-sectional Shape of Blade (right): Max. Strain Locations	19
2.3	Strain vs. Time at 15.9 m from hub (Left) and Single sided amplitude spectrum in frequency of each flexing mode (Right): Data shown for NREL offshore turbine at 24 m/s wind speed and low turbulence.	20
2.4	Edgewise and Flapwise strain power in an offshore blade as a function of blade location. Data are obtained during operational cycles corresponding to the maximum peak amplitude.	21
2.5	Energy Harvester Design Map for $W_{strain} = 280 \mu\text{J}$	25
3.1	A Piezoelectric energy harvester (EH) is installed on a blade as a d_{31} configuration.	28
3.2	A piezoelectric generator is modeled as a lump-sum system. m , b , and k are the mass, structural damping, and stiffness of a generator.	29
3.3	Illustration of trends of the conversion efficiency over a range of damping coefficients; the efficiency depends on the input frequency and its maximum occurs at the material damped natural frequency, which shifts lower as damping increases.	31

3.4	A Sketch of the Experimental Set-up Specifications: The beam is constrained as a cantilever at its root, and the top is actuated by a linear motor.	34
3.5	Two types of MFCs (P1 and P2 types) are installed in the front and back of the beam.	34
3.6	Overall Experimental Setup; a linear motor actuates the tip deflection of the beam. The EH installed on the beam is wired to a resistor, where voltage and current in the circuit are measured.	35
3.7	Strain command input for a 5 MW wind turbine from the FAST simulation is shown in a blue solid curve. Strain measurements (dashed red line) of the beam follow well the command input.	36
3.8	Experiment Process for Wind Turbine Blade Flexing	36
3.9	Voltage(dashed) and Current(solid) Outputs of the MFC EH for a Sine Excitation of a 10 mm ($\sim 400 \mu\epsilon$) mean-to-peak amplitude at 1Hz	37
3.10	Voltage Output(dashed) and Strain Input(solid) of the EH for a Blade Strain Profile	38
3.11	Voltage(dashed) and Current(solid) Outputs of the EH for a Blade Strain Profile	38
4.1	Strain vs. Time at 15.9 m from hub (L) and Single sided amplitude spectrum in frequency of each flexing mode (R): Data shown for NREL offshore turbine at 24 m/s wind speed and low turbulence.	45
4.2	Edge/Flapwise strain power available in an offshore blade as a function of blade location. Data are obtained during operational cycles corresponding to the maximum peak amplitude. ($E_0 = 1$ GPa)	45
4.3	Experimental result of EH conversion efficiency over input frequency (200 $k\Omega$ load resistance and 200 $\mu\epsilon$ input peak amplitude)	46
4.4	Construction of Model-free Structural Health Monitoring for Wind Turbine Blades	48
4.5	Stiffness Reduction Model (L)20, Simple Damage Model for the Matrix Cracking (R)	50
4.6	Wind Data (L), Edgewise Strain Data from Leading Edge of Three Blades at the Root (R)	52

4.7	Pulse Timing of EHs (L), Ratio Factors of EHs (R)	53
4.8	Unhealthy Blade Simulation: Pulse Timing of EHs (L), Ratio Factors of EHs (R)	54
5.1	Schematic drawing of a vibration-based SHM system: (a) three identical sensor nodes mounted on blades, (b) node with energy harvester and telemetry, and (c) remote-sited data acquisition and health monitoring.	61
5.2	Construction of Model-free SHM for Wind Turbine Blades	62
5.3	An overview of the proposed SHM system: The hardware consists of the EH block (Section 2) and the algorithm consists of the remaining blocks (Section 3).	64
5.4	A sample case of harvested strain energy residuals is depicted. For each decision time interval, the three residuals are initialized to zero. The residuals $r^{(13)}$ and $r^{(23)}$ exceed the threshold at the decision time k_d , indicating that blade three is damaged.	68
5.5	Strain Amplitude of an Intact Thin-Walled Finite Element Beam and Degradation Area: The beam is 61.5 m long and three sizes of degradation are considered at 20.5 m location as shown in the insets.	75
5.6	(a) Division of residuals in August 2013 for three blades into ten windows superimposed, (b) Propagation of the standard deviation of the residuals for August 2013	78
5.7	Normalized real power output of the Eolos turbine compared to the nor- malized σ : The residual variance follows the trend of the turbine power output.	78
5.8	Receiver Operating Characteristic Curves for damage $g_D = 0.0005$. To meet the performance targets of 90% p_{TP} with $p_{FP} < 1\%$, the decision time increases significantly when the degradation parameter is small. . .	80
5.9	Receiver Operating Characteristic Curves for damage $g_D = 0.0035$	80
5.10	Decision time versus degradation parameter with $p_{FP} = 0.7\%$ for the baseline $\bar{B} = 0.0104 \mu\text{J}/\text{step}$ and $\sigma = 0.102 \mu\text{J}$	82
5.11	Decision time versus degradation parameter with $p_{FP} = 0.7\%$ for the enhanced EH by increasing surface area, $\bar{B} = 0.0416 \mu\text{J}/\text{step}$ and $\sigma =$ $0.204 \mu\text{J}$	82

A.1	Two Excitations of Strain Input to EHs	100
A.2	Two Excitations of Strain Input to EHs	101
A.3	Strain and Moment Distribution Charts for an Experimental Beam . . .	103
A.4	ANSYS simulation validates beam design to have uniform strain field. A straight beam (a) has greater strain gradient from its root to the tip than a tapered beam (b), which has smaller variation in the one-third area. .	104
B.1	Discrete Pulses over Time: Asynchronous pulses of three EHs are shown, and accumulated strain energy can be estimated by interpolation between two neighboring pulses.	107
B.2	Concept of Estimated Strain Energy Over Discrete Time, k	109
C.1	Standard deviation propagation of a residual over 36 hours in May 2013 for Eolos Turbine Blades.	112
C.2	Standard deviation propagation of a residual over 36 hours in June 2013 for Eolos Turbine Blades.	113
C.3	Standard deviation propagation of a residual over 36 hours in August 2013 for Eolos Turbine Blades.	114
C.4	Standard deviation propagation of a residual over 36 hours in September 2013 for Eolos Turbine Blades.	115
C.5	Standard deviation propagation of a residual over 36 hours in October 2013 for Eolos Turbine Blades.	116
C.6	Standard deviation propagation of a residual over 36 hours in November 2013 for Eolos Turbine Blades.	117

Chapter 1

Introduction

Global warming induced by greenhouse gas emissions will intensify the challenges of global instability, poverty, and conflict [4]. Among the efforts to reduce greenhouse gas emissions, generating electricity from wind power is a promising solution: wind power is the least cost option among renewable energies when adding new generation capacity to the grid [5]. The estimated levelized energy cost of wind in 2019 is as low as \$80.3/MWh, compared to solar PV (\$130/MWh) and solar thermal (\$243.1/MWh) [6]. The global cumulative installed wind capacity in the end of 2013 is 318 GW, approximately 3% of total energy consumption globally [7]. Global Wind Energy Outlook projects the total wind power installation up to 2,000 GW by 2030 [5]. This is the capacity which produces approximately 18% of total global electricity demand and assists to reduce over 3 billion tons of CO₂ emissions annually. As noted in the DOE-issued report, however, reduction in operating and maintenance costs is a major problem [8]. While failure can occur in any structural component, one of the most common and critical component failures is a wind turbine blade [9–11]. Blade failure leads to the catastrophic failure of a wind turbine.

Acquiring an early indication of structural or mechanical problems allows operators to plan maintenance, control the machine based on the conditions, or shut down the machine to avoid further damage in the case of an emergency [12]. Thus, a condition based maintenance program that utilizes data obtained in real time from sensors located on turbine components can improve the reliability and service-time of wind turbines in the end. This sensor network system is referred to as a Structural Health Monitoring

(SHM) system. SHM is the process of implementing a damage detection strategy for engineering structures [13]. SHM is crucial to avoid catastrophic failure of a wind turbine and reduce wind turbine life-cycle costs. Sensor data is acquired and evaluated continuously, allowing for preventative maintenance and shortened down time. Rytter [14] classified various methods based on four levels of damage identification: 1. Determination that damage is present in the structure, 2. Determination of the geometric location of the damage, 3. Quantification of the severity of the damage, and 4. Prediction of the remaining service life of the structure. The ultimate goal of any SHM system is the level 4; however, in this thesis, it will be focused to determine whether damage is present in rotor blade structures of a wind turbine. The intent is that such a monitoring system improves maintenance and indirectly affects the reliability of a wind turbine.

This chapter reviews why it is important to monitor wind turbine blades, and what current SHM technologies are available for wind turbine blades or similar applications. In the end of the chapter, the objective and the contributions of the thesis are given.

1.1 Why is a wind turbine blade important?

Monitoring wind turbine blades is very important but challenging. The impact of rotor blade reliability is significant. Most wind turbine blades are made of composite materials. Currently, in general, commercial blade length is more than 40 to 50 meters—a comparable size to a short bridge. Also, the blades are typically located in severe weather conditions and remote sites to take advantage of strong winds. Additionally, it is quite often that operational information such as wind speed and direction is limited due to technical and financial restrictions.

1.1.1 Impact of Blade Reliability

Failure of wind turbine blades is considered as one of the most undesirable events for wind turbines. The overall effect of blade failure to the reliability can be determined by considering the repair cost, the downtime, and the failure rate. The repair cost of blades is high, and a wind turbine has to be stopped for the repair service of blades for a long period of time. Also, the blade failure is one of the most common type of damage at a considerable failure rate. A study in Germany reported annual failure

rates of wind turbine components from their experience over 15 years with 1,500 wind turbines [11]. Based on Hahn et. al [11], the percentage of blade failure accounts for 7% of total number of failures. The downtime is about 4 days (approximately 10% overall downtime) among the failures of wind turbine components [11] (Table 1.1). As noted in the report [15], market data on actual project-level operational and maintenance costs are not readily available. But overall replacement costs can be inferred by components installation costs. The cost of rotor blades can account for 15~20% of the total cost and is the most expensive type of damage to repair [16]. Based on unscheduled maintenance costs of 1.5 MW wind turbine (70 m rotor and 84 m hub height) [17], rotor blades hold approximately 20% of the total cost (Table 1.1). An overall effect in Table 1.1 can be calculated by multiplying the three effects (failure rate, down time and cost) and scaling across the components (see Table 1.1). Considering the combined effect, the potential failure mode of rotor blade is most significant (27.56%) followed by supporting structure (18.71%), gearbox (15.52%), electrical system (9.44%), etc. But, it gives much sense that the blade and gearbox failures are more important than the tower which share is only meaningful when total collapse of a tower. Thus, types of failures like rotor blades or a gear box are greatly concerned for longer down time and high repair cost in the contrast to frequently failed components like electrical systems but with less costs.

Moreover, a broken blade—due to structural failure—can cause a great deal of unbalanced torque to the whole wind turbine system. This can result in the tower collapse [18]. Additionally, a serious safety concern to living environment can be drawn by a broken blade in that a modern rotor blade is designed to use a lift force. This means a wind turbine blade can fly like an airplane wing. There was an incident in the U.K. that a torn-off blade flew as far as 8 km and struck a residential house through the window [10].

1.1.2 Design with Composite Materials

Fiber Reinforced Polymer (FRP) composites offer excellent mechanical properties (higher strength /density ratio) and easier shaping than widely used metallic materials. Use of FRP materials, which was limited to aerospace applications, has been expanded to infrastructure and commercial sectors like sports gear. Wind turbine blades are not an exception, because rotor blades require light weight and high strength. Most of the

Table 1.1: Failure rates, down time, and maintenance cost of wind turbine main components (%) [9, 11]. The combined effect is the scaled product of these three factors.

Components	Failure Rates	Down Time	Cost	Combined Effect
Rotor Blades (Pitch)	7.00%	10.10%	20.60%	27.56%
Supporting Structure	4.00%	7.80%	31.70%	18.71%
Gearbox	4.00%	15.30%	13.40%	15.52%
Electrical System	23.00%	3.50%	6.20%	9.44%
Electronic Control	18.00%	4.00%	6.90%	9.40%
Generator	4.00%	17.30%	6.70%	8.77%
Rotor Hub	5.00%	8.30%	7.20%	5.65%
Drive Train	2.00%	14.30%	4.00%	2.16%
Yaw System	8.00%	5.80%	1.80%	1.58%
Sensors (Control)	10.00%	4.00%	0.80%	0.61%
Mechanical Brake	6.00%	6.00%	0.60%	0.41%
Hydraulic System	9.00%	3.50%	0.30%	0.18%
Total	100%	100%	100%	100%

blades in utility-sized generators are made of fibre-reinforced composites such as glass fibre/epoxy, glass fibre/polyester, wood/epoxy or carbon fibre/epoxy composites [19]. Light weight FRP blades provide high performance (low mass inertia) with low conservative margins of safety. By using FRP, a high strength blade can be fabricated without a weight penalty. However, the sensitivity of composite materials to impact loads, large deflections and susceptibility to moisture make the use of FRP challenging. Analytic calculation of the service life or the failure of FRP composites is difficult. If the structure is operating in remote sites under harsh conditions such as sudden wind gusts and lightning strikes for a long period of time, it becomes more difficult to make accurate fatigue life predictions of FRP materials, and so the maintenance of FRPs becomes particularly challenging.

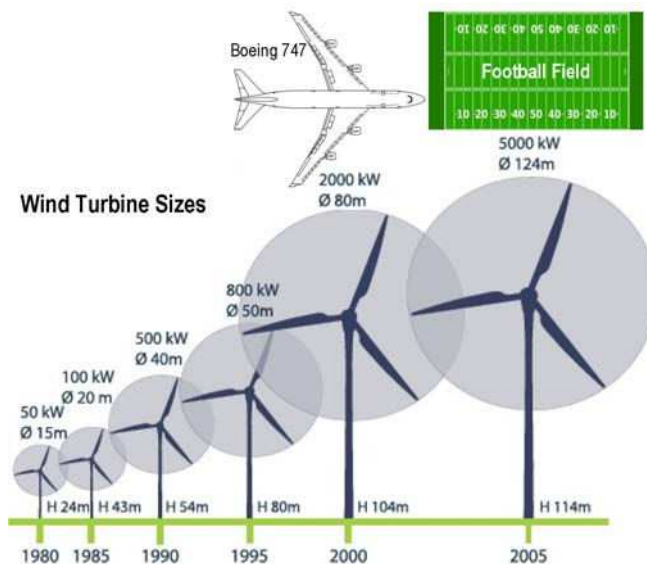


Figure 1.1: Increasing size of wind turbines over the last three decades is compared to a commercial jet airplane and an American football field at the same scale from [1].

1.1.3 Loading Conditions for Wind Turbine Blades

Wind turbine blades are under extreme loading conditions. High variability due to the stochastic nature of wind and long fatigue loading make the working conditions severe [20, 21]. Like bridges and airplane wings, rotor blades suffer from random excitation. And blades are under repeated fatigue loads—up to 10^8 or 10^9 —like helicopter blades. As shown in Figure 1.1, the size of wind turbine blades have been increased over the last three decades up to approximately 60 meters to design high-efficiency wind turbines, maximizing power capture [1].

Wind turbine blades are subject to bending, twisting and axial loads. Twisting loads are created by aerodynamic torque, blade pitching motion, and structural twist of blades. Axial loads—longitudinal extension—are made by the blade weight and are typically the minimal effect to blade health. Bending loads are in the edgewise and flapwise directions. Edgewise bending is a result of the gravity loads (i.e. blade weight) and is periodic, corresponding to the blade rotational speed. Flapwise bending is in the direction of the blade faces, perpendicular on the rotor plane. The flapwise

moments originate from the thrust force due to wind loads. Thus, edgewise strains are more periodic than flapwise strains, which vary randomly in both fluctuation range and mean [22].

1.1.4 Restrictions on Sensing Approaches

Wind turbine blades pose unique restrictions on sensing approaches. In an SHM system, sensors are typically wired to the central processing hardware. Many resources including transducers, D/A to A/D converters, multiplexers, signal conditioners, and processors for a wired SHM system are commercially available [23] (and more). However, wire-based SHM techniques are not easily applicable to rotor blades for various reasons. First, blades are rotating posing difficulties in wiring. Second, wiring always demands substantially added cost to the blade construction [24]. Since one line tends to be connected with several important sensor nodes to reduce installation costs [23], more failures at one location may disable the entire network. Even without these problems, the reliability of wired SHM for 20 years under harsh conditions is a concern: expensive maintenance for the wired sensor network must be regularly conducted.

Wireless sensing and processing systems have been introduced to overcome these drawbacks. In a wireless monitoring system, a sensor, signal conditioner and telemetry are necessary. Typically, these components are powered by a battery [25]. For example, a wireless sensing unit developed for civil structure health monitoring by Lynch et. al [26] consumes 250 mW to 900 mW, with the electric energy for each sensor / telemetry supplied by a 9V alkaline battery. With discrete power sources, many sensors can be employed and distributed over the entire structure. While current communication units are designed to minimize power consumption, battery lifetime is still a concern. Battery replacement is problematic, for wind turbine blades are installed on the top of a tall tower and turbines may be located in a remote area. A rechargeable battery is not only relatively heavy and fairly large compared to the dimension of a wireless node, but also is limited by its own service life. While a capacitor (no service life) may be a possible energy storage approach, it is generally much larger than a battery that stores the equivalent charge and the discharging rate is exponential for a short period of a service span by one time charge.

1.2 Review of Current SHM Technologies

An SHM system to detect damage requires a monitoring methodology (i. e. an algorithm), which is based on measurements and analysis of the dynamic response (of sensors) to environments. In this section, current SHM methods and sensor network systems for SHM are reviewed.

1.2.1 Existing SHM Methods

Because structural damage has an adverse effect on the functional safety, e.g. a safe long highway-bridge for crossing cars, SHM schemes are important and have been extensively studied. Ciang et al. [27] reported a comprehensive review on SHM of a wind turbine system, including a few SHM techniques which are currently available. Some techniques in the paper [27] such as thermal imaging, ultrasonic, or X-radioscopy method are not appropriate to an on-site autonomous monitoring system. Vibration-based SHM methods such as a modal analysis, a frequency response function analysis, and a strain energy method are more relevant for wind turbine blades. Carden and Fanning [28] reviewed vibration-based SHM methods. Montalvao et al. [29] summarized SHM methods especially emphasizing on composite materials. From these two papers, vibration-based SHM can be largely categorized as the frequency/modal (vibration mode), time domain (vibration transition) and direct signal analysis. Some of the important techniques employed in monitoring health of composite blades involve evaluation of natural frequency, mode shape/curvature, Operational Deflection Shapes (ODS), modal strain energy, impedance, Lamb wave, and statistical history (Auto-Regressive family models) [28, 29].

Many SHM systems for wind turbine blades utilize vibration-based techniques and showed the ability to detect damage in the structure. Vibration mode and transition evaluation is found in Ghoshal et al. [30], White et al. [31] and Light-Marquez et al. [32]. Four SHM techniques—transmittance functions, ODS, resonant comparison and wave propagation—were experimentally examined and compared by Ghoshal et al. [30]. They used a scanning laser Doppler vibrometer to increase the measuring sensitivity conveniently without contacting the blade, and there was a range of detecting capabilities among the four methods. White et al. [31] presented an SHM method for a lab-scale

carbon composite wind turbine blade, TX-100. In this paper, several accelerometers were deployed using transmissibility, virtual forces, and time-frequency analysis. Light-Marquez et al. [32] investigated three types of SHM: frequency response function, Lamb wave, time series (Auto-Regressive) analysis. Damage was emulated by a putty attachment to the blade surface and all three methods could successfully detect damage. Active impedance based SHM systems have also been developed for wind turbine blade SHM: Zayas et al. [33], Deines et al. [34], and Pitchford et al. [35]. They used either PZT (lead zirconate titanate) or MFC (Macro-Fiber Composite) piezoelectric materials for the actuator and sensor. The detecting ability of SHM in the above depends on 1) actuator power; 2) sensor location; and 3) sensor resolution. Direct measuring SHM is also found in Schulz et al. [36] and Rumsey et al. [12]. Schulz et al. [36] developed a structural neural system that is a 10×10 PZT sensor array over a 9-meter-long wind turbine blade. The sensors of the array are connected to conventional Acoustic Emission (AE) equipment. They could measure acoustic vibrations (strains), concluding detecting damage using continuous PZT sensors was feasible. Rumsey et al. [12] also studied a few direct measuring methods based on strain gages and AE sensors. They concluded that unique sound events were captured (listened) when damage occurred. Also strain energy reduction over fatigue cycles was observed as damage grows. As shown in the papers [12, 30–32], vibration based techniques are often combined with other approaches to improve detection capabilities. While researchers have demonstrated that vibration based techniques can detect damage, their success depends on the proximity of sensors to the damage site. To address this issue, one approach is to use many sensors such as [12], since damage initiation site is often unpredictable. Note that all these methods have been developed with a wired sensor network.

1.2.2 Wireless Sensor Network for SHM

The SHM methods reviewed in the previous section have been primarily developed as wired systems using inertial sensors (accelerometers) [31, 37], strain gages [12], AE sensors [12, 36, 38], and electric impedance-based sensors [33–35, 39]. But these sensors can be considered for wireless SHM. Table 1.2 [23, 39] summarizes the sensors on a basis of the measurements, sensing type, power consumption and installation cost. For a wireless system, low power consumption along with low device cost is desirable, so a

Table 1.2: Comparison of Sensors for Wireless SHM

Sensor	Measurement	Method	Type	Power	Cost
Accelerometer	Acceleration	Global	Passive	Low	Low
Strain gage	Strain	Global	Passive	Very low	Low
Acoustic Emission	Sound	Local	Passive	0-Very low	Low
Fiber Bragg Grating	Light (Strain)	Global	Active	Laser required	High
Piezo-electric patch	Lamb wave	Local	Active	Medium	Low
	Elec. impedance	Local	Active	Medium	Low

passive type is recommended. Among passive sensors, accelerometers and strain gages measure structural dynamic behavior changes, and AE sensors detect damage events such as the cracking sound.

There are several applications in which a wireless monitoring system was implemented with accelerometers. For the Golden Gate Bridge in San Francisco [40], a wireless monitoring system was developed to monitor the structural health. Two kinds of accelerometers were employed at 64 sensing nodes with 1 kHz sampling rate. Four lantern batteries (9 V) are used for each node to support power consumption of a few Watts. In the paper, satisfactory monitoring results were achieved. It is noted that a low implementation cost, \$600 per node compared to thousands of dollars for a wired network, has been achieved. Other examples of wireless SHM with accelerometers include a ceiling structure [41], habitat monitoring [42], intelligent bridge and infrastructure maintenance [43], and a stand-alone wireless sensing module for civil structures [44]. In each of these examples, the sensors were powered by batteries. A wireless SHM system with strain gages was reported for a helicopter rotor shaft by Arms et. al [45]. In the paper, 0.98 mW of power was required and the device could sample and transmit strain data. They concluded that the obtained online strain information could be used for optimizing maintenance scheduling and preventing possible failures. For wireless applications, the literature commonly indicates the importance of reliability of communication, overall size, low power consumption, and alternative power sources such as an energy harvester (EH) rather than a typical battery.

In the helicopter rotor application [45], a commercially available wireless telemetry

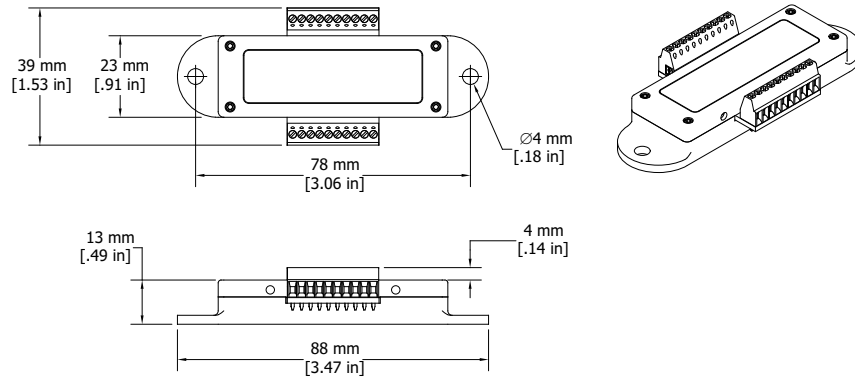


Figure 1.2: EH-Link layout from the Lord Microstrain, Inc. [2]

module was employed. Telemetry modules currently available have the capability of harvesting energy from a wide variety of sources and powering a range of sensors. An off-the-shelf sensor module such as the Micro Strain EH-Link [46] is available. It is smaller, uses less power, and can adapt a battery, solar cell, thermoelectric or piezoelectric material, compared to the sensor modules in [40, 41, 44]. It also combines telemetry, signal conditioning, onboard sensors (a triaxial accelerometer, relative humidity and temperature sensor), and signal conditioning for a Wheatstone bridge which is compatible with strain gages. The overall size of the unit is 78×39 mm as shown in Figure 1.2. Power consumption varies depending on hardware configurations as well as the number of sensors used in one module. In a continuous running mode from the table in [2], 18.53 mW power by 2.47 mA is required with 256 Hz sampling rate, 48 buffer packet and all onboard sensors used at the same time (the maximum configuration). The power consumption can be decreased down to 0.11 mW by 14 μ A with 1 Hz, 5 buffer packet and one Wheatstone bridge. In designing the EH, the energy in Joules generated per cycle of strain will be stored to achieve the telemetry module energy requirements. From the specifications in [2], for instance, 12 μ J is required for start-up of the device, 168 μ J is for a Wheatstone bridge measurement, and 92.4 μ J is for a packet of data transmission. Total usage for one point measurement and transmission is approximately 272.4 μ J/cycle. The capacitor size and charging time depends on the telemetry/sensor node power requirement given the available energy and the type of SHM methods.

1.3 Thesis Objectives

The objective of the thesis is to develop a reliable wireless SHM system for wind turbine blades. Several tasks are associated with achieving this goal: study on an energy harvester; calculate available strain power for a rotor blade; find a novel sensing approach; and develop a decision algorithm.

A wireless sensor network system uses Piezoelectric EHs for the power requirements of the sensor function, the data transfer, and the signal conditioning. Using an EH, strain energy is converted into usable electric energy, and an EH can be modeled as a electromechanical dynamic system, which output performance depends on input frequencies. Thus, methods to calculate the energy conversion and to find this conversion efficiency as a function of input frequencies should be studied.

Piezoelectric EH, the power source to a wireless sensor network, are to be installed on rotor blades. To enable wireless data transfer, strain energy of blades should be sufficient. Strain energy availability varies depending on at least two key factors: the size of rotor blades and wind conditions. Thus, available strain energy is evaluated for three typical wind turbines with three wind conditions.

Based on evaluated strain energy, a sampling frequency of sensor nodes can be calculated. The converted strain energy is stored in a capacitor. This stored electric charge powers an RF transmitter, and once the charged energy is sufficient, a measurement is sampled. In rotor blades, low frequency vibrational strain energy, which subsequently limits a sampling rate, is available. A low sampling rate gives a challenge to data analysis, and a new sensing approach is required. A new sensing approach can take advantage of the timing of data output from the RF transmitter, which is tied to the charging time, and intrinsic three rotor blades.

A decision-making algorithm is needed to declare the damage. When three responses of sensors located at the same position on the three blades are compared, an outlier among three can be determined as a damaged blade. The challenge is the presence of noise due to several factors including stochastic winds. Wind variation creates strain energy differences between two healthy blades, and a false alarm can be alerted. Thus, a key to success on a reliable damage decision is to apply probabilistic analysis to decrease false alarm rate and increase detection probability.

1.4 Thesis Contributions

The dissertation covers the development of a wireless structural health monitoring system for wind turbine blades. This dissertation includes the following major contributions.

- 1) Piezo-electric energy harvesters are used to enable sensor nodes wireless without batteries. Energy harvesters convert a fraction of mechanical strain energy into electrical energy. It is stored in a capacitor, and a pulse is generated once sufficient energy is captured.
- 2) The strain energy availability in blades is reported for typical sizes of utility-scale wind turbines using FAST simulation. This summary can help energy harvester designers to identify a type and size of an EH for their needs.
- 3) Energy harvester efficiency for wind turbine applications is studied. An experimental setup is designed to measure the efficiency for excitation at low broadband frequency.
- 4) A new monitoring scheme utilizing three blades to cross-compare blades in real-time is introduced. Neither a physical model of a blade nor external loading information is necessary.
- 5) A probabilistic algorithm has been developed for the monitoring system. The system can provide statistical accuracy of false alarming and damage detection probabilities. Also, the probabilistic approach provides a mathematical background and systematic procedure for design of a structural health monitoring system.

Chapter 2

Wind Turbine Blades as a Strain Energy Source for an EH

2.1 Summary

Structural health monitoring of wind turbine blade mechanical performance can inform maintenance decisions, lead to reduced down time and improve the reliability of wind turbines. Wireless, self-powered strain gages and accelerometers have been proposed to transmit blade data to a monitoring system located in the nacelle. Each sensor node is powered by a strain Energy Harvester (EH). The amplitude and frequency of strain at the blade surface (where the EH is mounted) must be sufficient to enable data transfer. In this study, the strain energy available for energy harvesting is evaluated for three typical wind turbines with different wind conditions. A FAST simulation code, available through the National Renewable Energy Lab (NREL), is used to determine bending moments in the wind turbine blade. Given the moment data as a function of position along the blade and time (i.e. blade rotational position), strain in the blade is calculated. The data provide guidance for optimal design of the energy harvester.

2.2 Introduction

The DOE has set a goal of “20% wind energy by 2030” [47]. Reduction in operating and maintenance costs for wind turbines has been identified as a major challenge to

achieving this goal. Wind turbine maintenance is a particular challenge because wind turbines are often located in remote regions (including offshore). Structural health monitoring (SHM) is a promising approach that can enable preventative maintenance, reduce down time and significantly reduce life-cycle costs [30]. While failure can occur in any structural component, one of the most common and critical components to fail is the wind turbine blade [9]. It is particularly challenging to continuously monitor blade health: (1) the blades are quite long and an extensive network of sensors is required; and (2) the blades are rotating, posing challenges to delivering power to and receiving data from the sensor network. To address these issues, a novel sensing and SHM system has been proposed (Figure 2.1). The system is comprised of a network of sensor nodes (Figure 2.1(a)). Each node is powered by an energy harvester (EH) and includes a sensor and telemetry unit (Figure 2.1(b)). The strain gauge and/or accelerometer data will be wirelessly transmitted to a centralized monitoring system in the turbine nacelle (Figure 2.1(c)). Recent technological developments in energy harvesting materials and fabrication processes along with commercially available low power telemetry modules make these technology advancements a possibility for the first time. In the present study, the availability of strain energy for various commercially available wind turbines will be evaluated.

2.3 Background

2.3.1 Sensors and Telemetry for SHM

Damage to the composite blade often begins as a matrix crack that can lead to debonding and delamination as the blade undergoes cyclic loading. A variety of sensing approaches have been considered for structural health monitoring of composite structures such as helicopter or wind turbine blades including: acoustic sensors, accelerometers, strain gauges, piezoceramic transducers and fiber optic sensors [12, 31, 33, 34, 38]. These sensors typically provide strain, acceleration and acoustic/vibration data in real time. Sensor data is processed using algorithms designed to predict the location and extent of damage based on sensor data. Ciang et al. [27] completed an extensive review of sensors for damage detection and their suitability as an SHM system for wind turbine blades.

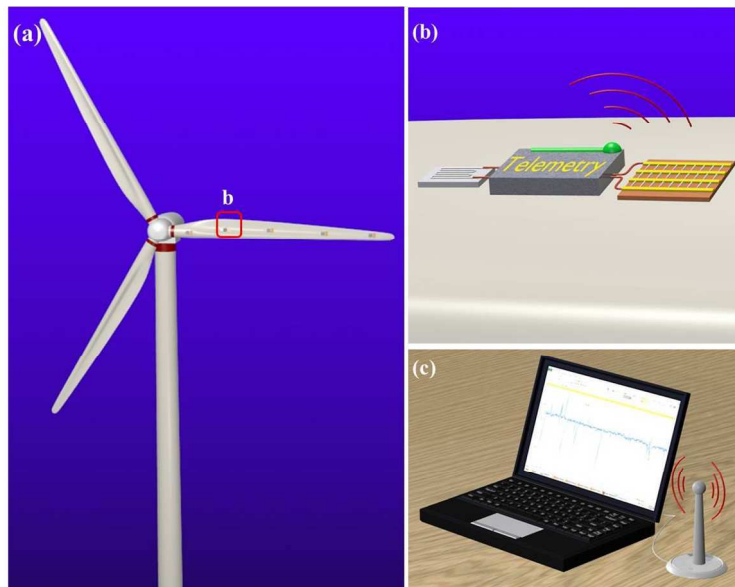


Figure 2.1: Schematic showing (a) sensor nodes mounted on blade, (b) node with energy harvester and telemetry, and (c) data acquisition and health monitoring.

Sensors that provide acoustic emission, thermal imaging, and ultrasound data can provide overall health but are difficult to interpret because the blade geometry is complex. These authors identified “hot spots” on the blade where failure is likely to occur. These hot spots include the blade root, 30% span from the root, and 70% span from the root. Even so, damage detection requires multiple sensors “in the vicinity” of the anticipated damage location. Discrete sensors such as strain gauges and accelerometers are acceptable as long as there are clusters of these sensors located near anticipated damage sites to ensure proximity to (and detection of) damage. With many sensors, the challenge becomes powering the sensors and relaying the data to a central data acquisition system for further processing.

2.3.2 Feasibility of Energy Harvesting

In the present study, the feasibility of an EH for wind turbine blade SHM has been investigated. One aspect of this study has been to verify that the strain energy available during typical operating conditions can satisfy the power requirements for sensing and

telemetry. A data acquisition and power management strategy is considered such that “harvested” energy is stored in a capacitor until a threshold energy level is achieved. Once the stored energy is sufficient for data acquisition and telemetry, strain data for several complete revolutions of the wind turbine are wirelessly transferred to a data acquisition substation as a burst. At which point, the energy harvester restores the capacitor and the data cycle begins again. Feasibility, then, entails estimating the power requirements and the power available to be harvested.

The strain energy harvested W_{strain} will depend on the energy harvester configuration, the frequency f and sinusoidal amplitude of the strain ϵ :

$$W_{strain} = \eta V E \cdot \epsilon^2 f \cdot \Delta t \quad (2.1)$$

where V is the volume of an EH, E is the modulus of the EH, and η is the efficiency of energy conversion. The charging time t is the time required to charge the capacitor and will also define the time between bursts of data transmission/acquisition. The magnitude of strain and frequency will depend on the wind turbine blade geometry and operating conditions. For example, it has been reported that flapwise and edgewise bending of the blade can provide strain ranging from $1200\mu\epsilon$ (1.65 MW turbine) to $3600\mu\epsilon$ at 0.25 Hz [17, 48, 49].

As noted, the energy available for harvesting depends on the strain and the frequency of vibration; and harvesting capability depends on the type and the design of an EH (Eq. 2.1). Thus is useful to define the power available P_{avail} and the EH design factor K_{EH} as

$$P_{avail} = E_0 \epsilon^2 f \quad (2.2)$$

$$K_{EH} = \eta V \frac{E}{E_0} \quad (2.3)$$

where E_0 is the nominal modulus of an EH material. By using this measure of power, simulation strain data can be compared for various turbines and under various operating conditions. For the purpose of comparison, a modulus of $E_0 = 1$ GPa is taken in all plots and data reported herein. Values can easily be scaled to evaluate other harvester materials. So, the harvested energy can be decomposed into an internal factor (K_{EH}) and external source (P_{avail} and t). Now, one can determine the type and size of an EH

from K_{EH} with selected charging time. And the original Eq. (2.1) is simplified into

$$W_{strain} = P_{avail} \cdot K_{EH} \cdot \Delta t. \quad (2.4)$$

While these studies provide a good starting point for estimating the strain energy available, a map of strain over the blade surface will be required to accurately assess the energy harvester design. The objective of this study is to characterize the strain energy available for a range of wind turbines under steady state and turbulent conditions. Three turbines have been selected that represent typical turbine power capacities and geometries: a CART3 (600 kW), a WindPact (1.5 MW) and a 5MW offshore wind turbine. Wind loading conditions are varied from 6 to 24 m/s at high and low turbulence.

2.4 Methods

There are a number of options available for creating a detailed finite element model of wind turbine blades. For example, NuMAD [50] is a pre and post processor (for use with ANSYS) with a graphical user interface that enables users to quickly create a three dimensional model of a wind turbine blade. One drawback to these models is that extensive knowledge of the blade geometry and composite material layup is required. This detailed information is considered proprietary by commercial wind turbine manufacturers. Instead, nonlinear simulations presented in this paper are performed using the FAST (Fatigue, Aerodynamics, Structures, and Turbulence) aeroelastic design code for horizontal axis wind turbines developed by the National Renewable Energy Laboratory (NREL) [3]. In FAST, the wind turbine is modeled as an interconnected system of rigid bodies (i.e., the nacelle and hub) and flexible bodies (i.e., the blades, tower and drive shaft) subjected to dynamic wind loads. FAST uses the assumed modes method for the flexible structural dynamics of the system and blade element momentum theory is used to calculate the aerodynamic loads using AeroDYN [51]. FAST can model wind turbines with a total of 22-24 degrees of freedom. This full order model includes first and second tower fore-aft and side-to-side bending modes, first and second flapwise bending modes of blades, first edgewise bending modes of blades, drive train torsion, generator position and nacelle yaw angle. Input data to the FAST code includes the turbine geometry and component material properties along with wind loading and aerodynamic data. Standard output data include blade displacement, such as flap-wise and

Table 2.1: Three Typical Wind Turbines Properties

Index	CART3	WindPACT	NREL Offshore
Rated Power	600 kW	1.5 MW	5.0 MW
Rated Rotor Speed	37.1 rpm	20.5 rpm	12.1 rpm
Cutin/Rated/Cutout Speed	6/13.5/20 m/s	3/11.5/27.6 m/s	3/11.4/25 m/s
Hub Height	34.9 m	84 m	87.6 m
Blade Length (Radius)	20 m	35 m	63 m
Blade Weight	1,807 kg	3,913 kg	17,740 kg
Blade Airfoil Type	s816, 817, 818	s818, 825, 826	DU21, 25, 30, 35, 40
References	Ref. [52]	Ref. [53]	Ref. [54]

edge-wise displacement, forces and bending moments as a function of rotation.

A number of predefined, FAST turbine models have been constructed and are available through the NREL FAST website. These models can be used to characterize the available strain energy for turbines of various sizes. Specifically, this paper will focus on three different turbine models: a) 600 kW CART3, b) 1.5 MW WindPact, and c) 5 MW offshore wind turbine. The specifications of each turbine are shown in Table 1. In each simulation, the standard built-in control law is used to generate the generator torque and blade pitch commands.

Blade strain is not calculated as part of the standard outputs from FAST. However, the FAST outputs include moments and deflections at various locations (nodes) along the span of the blades. These can be used to calculate strains in several ways: 1) local span (nodal) moments, 2) local span translational deflections, 3) blade tip deflection with a mode-shape function, and 4) blade root moments with a mode-shape. Strains calculated using mode-shapes are not accurate because the mode-shapes are only approximately correct and may not correspond to the actual blade mode in operation. On the other hand, nodal moment outputs can be used to compute accurate local strains at various nodal locations. Hooke's law provides the following relationship between strain and moment M :

$$\epsilon_E(z_b) = \frac{\sigma}{E} = \frac{M_E(z_b)y_b}{EI} \quad (2.5)$$

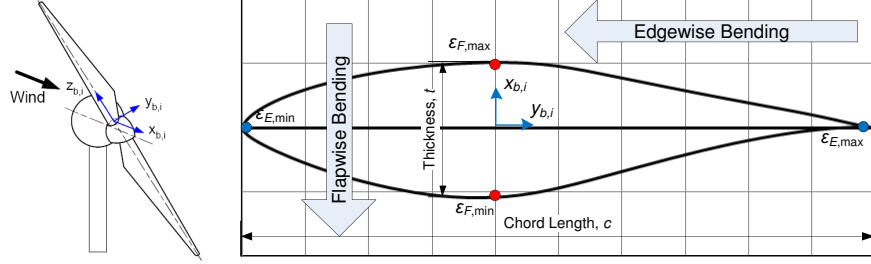


Figure 2.2: Blade Coordinate System (left) [3] and Cross-sectional Shape of Blade (right): Max. Strain Locations

$$\epsilon_F(z_b) = \frac{\sigma}{E} = \frac{M_F(z_b)x_b}{EI} \quad (2.6)$$

where ϵ denotes the strain, M is the bending moment, EI is stiffness, z_b is the distance from the blade support at the nacelle to the node, and x_b/y_b are the chord length and thickness of the airfoil. Eqs. (2.5 and 2.6) assumes pure bending mode is the dominant factor. The subscripts e and f denote the edge and flapwise directions on the blade. Figure 2 (left) shows the coordinate system of blades. Each bending direction is depicted in Figure 2.2 (right). Bending strain (or stress) is proportional to the distance from the neutral axis crossing the mass center. Therefore, x_b is the direction of the distance for the edgewise strain and y_b is for the flapwise strain.

These strains are greatest at the maximum distance as shown in Figure 2.2 (right). For the maximum edgewise strain, the chord length $y_b = \frac{c}{2}$ of the airfoil is used and the thickness $x_b = \frac{t}{2}$ yields the maximum flapwise strain. The airfoil geometry of a wind turbine blade is generally quite complicated and finding the neutral axis is nontrivial. A reasonable approximation is to use half the local thickness and chords length to estimate the maximum edge and flapwise strain. The FAST simulation allows up to nine nodal moment outputs. These can be used to compute strain at the nine discrete locations along the span of the blade. Specifically, at the i^{th} local nodes, the edgewise and flapwise

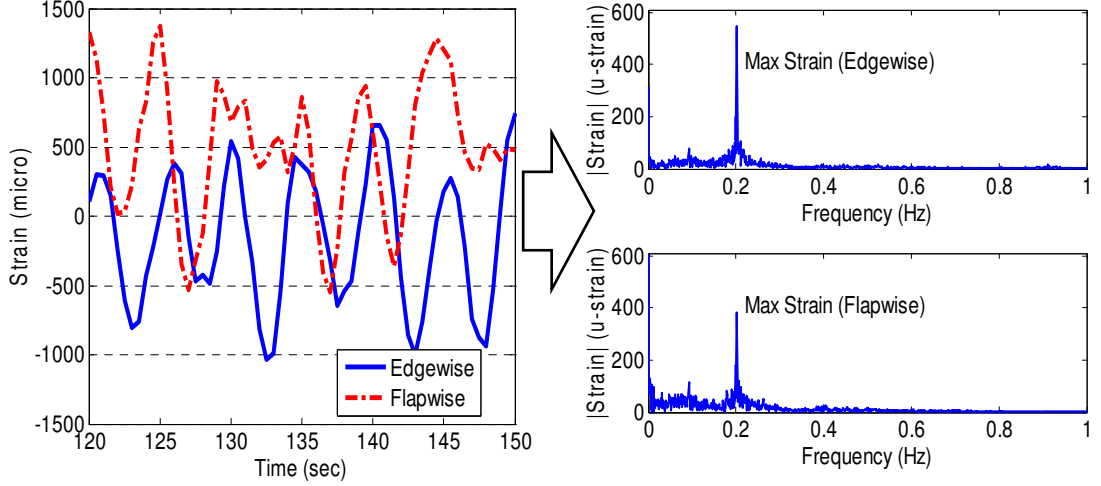


Figure 2.3: Strain vs. Time at 15.9 m from hub (Left) and Single sided amplitude spectrum in frequency of each flexing mode (Right): Data shown for NREL offshore turbine at 24 m/s wind speed and low turbulence.

strain can be expressed as in Eq. (2.7)

$$\epsilon_{E,i} = \frac{M_{E,i}c_i}{2(EI)_{E,i}}, \text{ and } \epsilon_{F,i} = \frac{M_{F,i}t_i}{2(EI)_{F,i}} \quad (2.7)$$

where c_i and t_i are the chord length and thickness of the airfoil at the i^{th} node.

2.5 Results and Discussion

Simulations were performed for turbines of three sizes and at different wind speed and turbulence conditions. Simulation results for the 5 MW NREL offshore wind turbine operating under wind conditions of 24 m/s at low turbulence are shown in Figure 2.3 and Figure 2.4. Figure 2.3 shows strain data in both edgewise and flapwise bending at an instant in time and Fast Fourier Transform analysis of each bending mode. Figure 2.4 shows the edgewise and flapwise strain power along the span of the blade during the operation under the selected wind conditions. As shown in Figure 2.3, the amplitude of the edgewise strain is ~ 550 micro-strain and the amplitude of the flapwise strain is ~ 390 micro-strain. The strain varies with time at a cyclic rate of ~ 0.2 Hz, corresponding

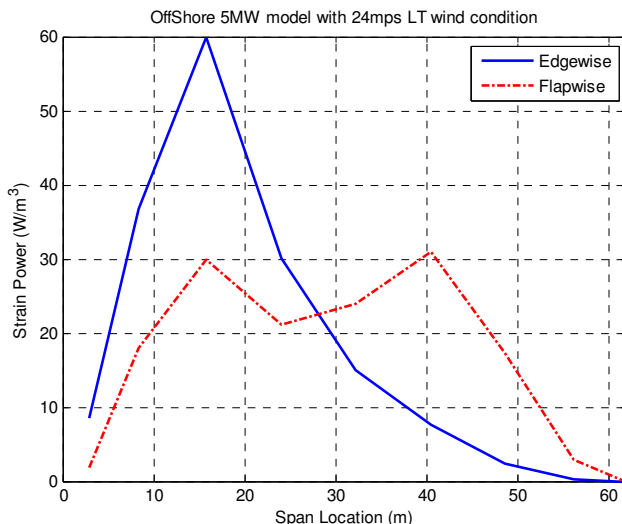


Figure 2.4: Edgewise and Flapwise strain power in an offshore blade as a function of blade location. Data are obtained during operational cycles corresponding to the maximum peak amplitude.

to the rotational frequency of the turbine at these wind conditions. For the flapwise bending mode, large non-zero mean strain is observed. But this bias term is disregarded, as the zero-frequency mode does not contribute to generate energy. In Figure 2.4, the maximum edgewise strain power, ~ 60 W/m³, occurs at a distance 15.9 m from the blade support (at the nacelle). On the contrary, the maximum flapwise strain power, ~ 31 W/m³, occurs at 40.5 m. A similar flapwise strain power of 30 W/m³ occurs at 15.9 m. Table 2.2 provides the summary of the simulation results for the 5 MW model.

Similar simulations were performed for the CART3 and WindPACT turbine models to assess the available energy for harvesting. Tables 2.2, 2.3 and 2.4 summarize the results of these simulations. The maximum strain, strain frequency and spanwise location of the maximum strain are shown for both edgewise and flapwise bending. Several trends are apparent in these results. First, the strain progressively increases with increasing turbine size. This is expected as the 5MW turbine has larger, more flexible blade leading to increasing strain. Second, the strain is greatest at the higher wind speed/lower turbulence intensity conditions. Third, the frequency of maximum strain

Table 2.2: Max. Strain of the NREL Offshore (5 MW) for the various wind conditions ($E_0 = 1$ GPa)

Wind	Edge [$\mu\epsilon$]	Flap [$\mu\epsilon$]	Freq [Hz]	P_{avail} [W/m^3]	$z_{b,max}$ [m, %]
6 m/s HT	312	-	0.13	12.65	15.9m (25%)
6 m/s LT	355	-	0.13	16.38	15.9m (25%)
13 m/s HT	432	-	0.2	37.32	15.9m (25%)
13 m/s LT	469	-	0.2	43.99	15.9m (25%)
24 m/s HT	515	-	0.2	53.05	15.9m (25%)
24 m/s LT	545	-	0.2	59.41	15.9m (25%)
6 m/s HT	-	55	0.13	0.39	15.9m (25%)
6 m/s LT	-	59	0.13	0.45	15.9m (25%)
13 m/s HT	-	178	0.2	6.34	40.5m (64%)
13 m/s LT	-	163	0.2	5.31	15.9m (25%)
24 m/s HT	-	352	0.2	24.78	40.5m (64%)
24 m/s LT	-	393	0.2	30.89	40.5m (64%)

tends to match with the rotor speed. While the edgewise strain is higher for all cases, the difference between edge and flapwise strain decreases at higher wind speeds. This trend can be a result of blade pitch control that is imposed at high wind speeds.

These results can be used to determine EH design requirements given the energy available and power transmission requirements. In Figure 2.5, the energy harvester design factor K_{EH} is shown as a function of the charging time Δt . Curves for three power levels P_{avail} , 13, 22 and 50 W/m^3 , are shown in the figure. These power levels are typical for the wind turbines investigated in the present work (see Table 2). In this case, a data transmission energy requirement of 280 μJ was selected, corresponding to the power required to transmit a single measurement via EH-link from Microstrain [46] (a commercially available wireless transmission module). The curves are obtained by setting the transmission energy equal to the strain energy harvested W_{strain} (Eq. 2.4). As an example, consider a ZnO nanowire EH [55] with an efficiency of 6.8%, volume of 0.38 mm^3 , and a modulus of 30 GPa, such that the design factor is 0.78 mm^3 . The corresponding charging time is approximately 2 hours for a harvester located on 5 MW

Table 2.3: Max. Strain of the CART3 (600 kW) for the various wind conditions ($E_0 = 1$ GPa)

Wind	Edge [$\mu\epsilon$]	Flap [$\mu\epsilon$]	Freq [Hz]	P_{avail} [W/m^3]	$z_{b,max}$ [m, %]
6 m/s HT	90	-	0.27	2.19	7.5m (38%)
6 m/s LT	109	-	0.29	3.45	7.5m (38%)
13 m/s HT	99	-	0.62	6.08	7.5m (38%)
13 m/s LT	85	-	0.62	4.48	7.5m (38%)
24 m/s HT	238	-	0.63	35.69	7.5m (38%)
24 m/s LT	249	-	0.62	38.44	7.5m (38%)
6 m/s HT	-	14	0.27	0.05	7.5m (38%)
6 m/s LT	-	17	0.29	0.08	7.5m (38%)
13 m/s HT	-	38	0.62	0.90	7.5m (38%)
13 m/s LT	-	32	0.62	0.63	7.5m (38%)
24 m/s HT	-	218	0.63	29.94	7.5m (38%)
24 m/s LT	-	220	0.62	30.01	7.5m (38%)

offshore wind turbine operating at 24 m/s (providing approximately $50 W/m^3$ power). For wind turbine conditions or locations in which less power is available, the charging time requirements are approximately 4.5 hours for $P_{avail} = 22 W/m^3$ and 7.5 hours for $P_{avail} = 13 W/m^3$.

2.6 Conclusion

The present study provides an estimate of the strain energy that can be expected for typical wind turbine geometries over a range of wind loading conditions. Based on the FAST simulation results, the maximum strain occurs at a distance from the hub that is approximately 20 to 33% of the blade length. For the three turbine models, the maximum strain amplitude is 550 micro-strain at 0.2 Hz for the 5MW offshore turbine. On going work as part of the EOLOS [56] facility at the University of Minnesota will include strain data from a fully instrumented 2.5 MW wind turbine. The estimates of strain energy from the current study along with the data from the full scale instrumented

Table 2.4: Max. Strain of the WindPACT (1.5 MW) for the various wind conditions ($E_0 = 1$ GPa)

Wind	Edge [$\mu\epsilon$]	Flap [$\mu\epsilon$]	Freq [Hz]	P_{avail} [W/m^3]	$z_{b,max}$ [m, %]
6 m/s HT	105	-	0.19	2.09	7.3m (21%)
6 m/s LT	174	-	0.19	5.75	7.3m (21%)
13 m/s HT	181	-	0.34	11.14	7.3m (21%)
13 m/s LT	169	-	0.34	9.71	7.3m (21%)
24 m/s HT	295	-	0.34	29.59	7.3m (21%)
24 m/s LT	304	-	0.34	31.42	7.3m (21%)
6 m/s HT	-	20	0.21	0.08	11.7m (33%)
6 m/s LT	-	20	0.19	0.08	11.7m (33%)
13 m/s HT	-	56	0.34	1.07	16.2m (46%)
13 m/s LT	-	37	0.34	0.47	11.7m (33%)
24 m/s HT	-	156	0.34	8.27	16.2m (46%)
24 m/s LT	-	168	0.34	9.60	16.2m (46%)

wind turbine will inform energy harvester design and development of data transmission algorithms.

Nomenclature

E	Young's Modulus of an EH, GPa ($E_0 = 1$ GPa)
$EI_{E(F),i}$	Stiffness in edge(flap)-wise bending at i th element [Nm^2]
K_{EH}	Design factor [m^3]
$M_{E(F),i}$	Edge(Flap)-wise moment at i th node [Nm]
P_{avail}	Strain power available [W/m^3]
V	Volume of an EH [m^3]
W_{strain}	Harvested strain energy [μJ]
c_i	Chord length of i th airfoil [m]
f	Strain frequency [Hz]
t_i	Thickness of i th airfoil [m]

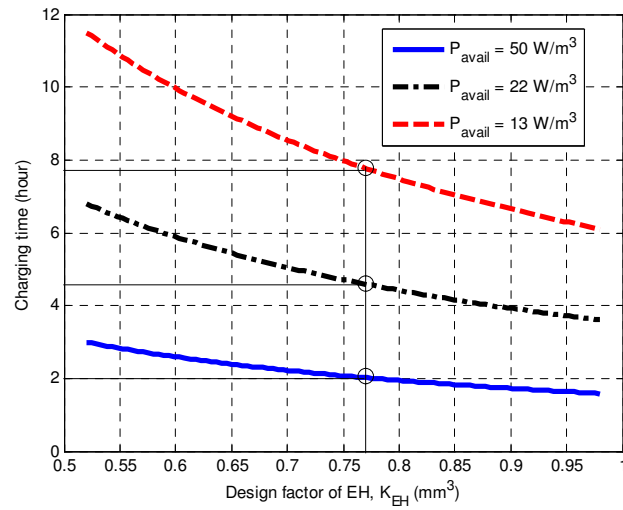


Figure 2.5: Energy Harvester Design Map for $W_{\text{strain}} = 280 \mu\text{J}$

t	Charging time [sec]
ϵ	Mechanical strain [$\mu - \epsilon$]
η	Energy conversion efficiency[-]

Chapter 3

Efficiency of Energy Conversion for Low Broadband Excitation

3.1 Introduction

Wireless sensing network systems are advantageous in many respects including easy installation, flexible deployment, and reduced costs. In addition, transmitting the data wirelessly avoids the vulnerability to unfavorable weather conditions such as lightning which can strike conductive wires and structures. Structural Health Monitoring (SHM) is one of the intelligent sensor-network systems which benefit from wireless technologies. Wireless monitoring systems were developed to monitor the health of structures including bridges [40, 57–59], buildings [41, 42, 60], helicopter rotors [45, 61], and wind turbines [23, 62–65]. Most of the applications are powered by batteries. However, the batteries will require periodical replacement, which is tedious and even dangerous for some applications like wind turbine blades. Modern full-sized wind turbines are typically taller than a 30-story building, and a blade length is about 50 meters long, which is comparable to a short bridge. Thus, wireless SHM takes advantage of self-powered autonomous sensors powered by energy harvesters (EHs).

An energy harvester converts unused ambient energy into usable electricity. Most common harvesting sources are environmental vibrations, light, and temperature difference. For example, Carlson et al. [66] examined piezoelectric, thermoelectric and photovoltaic energy harvesting techniques for onboard sensors on wind turbine blades.

They argued that wireless sensing is appropriate for the SHM of wind turbine blades due to the possibility of lightning strikes on wires. In the paper [66], authors concluded that the photovoltaic system was most promising to scavenge the largest energy. However, for structural monitoring, it is not always feasible to use solar powering [67]. Onboard sensors could be installed (or embedded) inside of blade panels (i.e. in the void space). Whereas, energy harvesting from the vibration source is most appropriate in structures which are monitored only when monitoring is necessary (when they vibrate). Structural failure is highly probable at moments of vibrations. In this regard, the piezoelectric mechanism for SHM is studied in [23, 45, 66, 68–72].

A wind turbine blade—made of composite materials typically—deforms during its operation. Wind turbine blades are under the wind force and/or gravity. An irregular wind force vibrates blades. When blades are rotating during turbine operation for a horizontal-axis wind turbine system, gravity exerts alternating bending moments. Both gravity and wind force make a blade deformed periodically and induce structural strain. This strain energy can be harvested by a piezoelectric phenomenon. Figure 3.1 illustrates a schematic drawing for the energy harvesting system. Thus, energy harvesting which converts mechanical energy from blade strain energy to usable electrical energy is promising for wireless SHM of wind turbine blades.

Harvested energy can be estimated by the conversion efficiency of an EH and available strain energy. EH conversion efficiency was studied in [73–77]. They found the conversion efficiency depends on the input frequency, but mostly pure harmonic signals at fairly high frequencies were considered. However, application specific conversion efficiency is required to construct an SHM system where the input force to an EH is at a low broadband frequency. When an EH is mounted on the surface of a wind turbine blade, the excitation frequency (associated with blade rotation) is less than the blade natural frequency (typically < 1 Hz). Thus, strain amplitude is relatively low. Moreover, the input from blade loading is not purely harmonic due to several factors including the wind variation. In this chapter, evaluation of an overall conversion efficiency—from mechanical to harvested electric energy—for low random frequency excitation is presented.

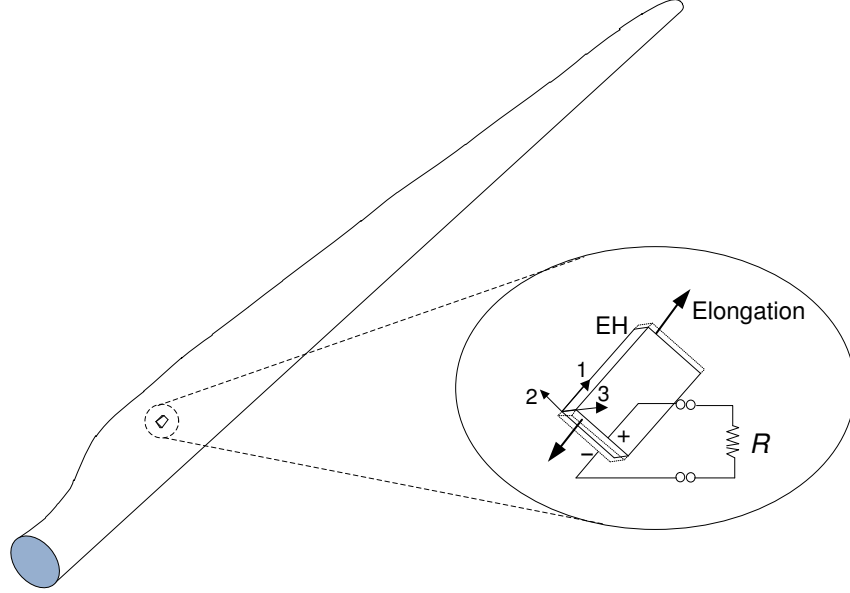


Figure 3.1: A Piezoelectric energy harvester (EH) is installed on a blade as a d_{31} configuration.

3.2 Model for EH efficiency

The energy conversion efficiency η_{me} is commonly defined as the time-averaged energy ratio between the input W_{in} and output W_e by

$$\eta_{me} = \frac{W_e}{W_{in}}, \quad (3.1)$$

where

$$W_e = \int R \cdot \dot{q} \cdot \dot{q} dt, \quad (3.2)$$

and

$$W_{in} = \int f_{ex} \cdot \dot{x} dt. \quad (3.3)$$

R , q , x , and f_{ex} are a resistive load, the electric charge on the electrodes, displacement of the generator, and an external harmonic function respectively. The generator where an EH is mounted can be modeled as a lump-sum system as shown in Figure 3.2. The

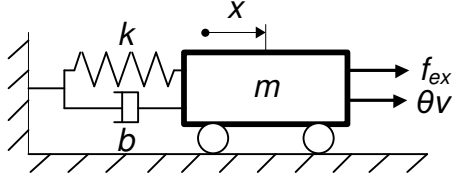


Figure 3.2: A piezoelectric generator is modeled as a lump-sum system. m , b , and k are the mass, structural damping, and stiffness of a generator.

induced electric voltage v and the electric charge q depend on the generator and piezo-material properties. The governing equations of the piezoelectric EH are described by coupled mechanical electrical simultaneous equations [78]. The mechanical behavior of the piezoelectric generator is expressed by

$$m\ddot{x} + b\dot{x} + kx - \theta v = f_{ex} \quad (3.4)$$

where m , b , k is mechanical mass, damping, and stiffness of a generator respectively. θ is the electromechanical coupling coefficient of a piezoelectric material. Two unknown variables x and v are solved by relating a circuit equation with zero initial conditions with a known input force f_{ex} , as

$$\theta x - C_p R \dot{q} = q \quad (3.5)$$

where C_p is the piezoelectric material capacitance.

Given the constitutive equations of Eqs. (3.4 and 3.5), the transfer functions between the mechanical force input $F_{ex}(s)$, and outputs of the electric charge $Q(s)$ and mechanical deformation $X(s)$, can be expressed as [79]:

$$H(s) = \frac{Q(s)}{F_{ex}(s)} = \frac{\theta}{(ms^2 + bs + k)(RC_p s + 1) + \theta^2 R s}, \quad (3.6)$$

and

$$G(s) = \frac{X(s)}{F_{ex}(s)} = \frac{RC_p s + 1}{(ms^2 + bs + k)(RC_p s + 1) + \theta^2 R s}. \quad (3.7)$$

Assume this one degree of freedom generator is under a single modal vibration. From Eqs. (3.1,3.6,3.7), the efficiency can be expressed as

$$\eta_{me} = \frac{\theta^2 R \omega}{|RC_p \cdot j\omega + 1| \cdot |D(j\omega)|}, \quad (3.8)$$

where $|D(j\omega)|$ is the magnitude of the denominator of $G(s)$ at the frequency of ω as

$$D(j\omega) = |(-m\omega^2 + jb\omega + k)(jRC_p\omega + 1) + j\theta^2 R\omega|. \quad (3.9)$$

As shown in Eq. 3.8, the efficiency depends on the input frequency ω . Figure 3.3 shows an illustration of the trends of the conversion efficiency for various damping coefficients. Its maximum occurs at the damped natural frequency of a generator when other variables are fixed. As damping increases, the frequency for the maximum efficiency becomes low.

3.3 Estimating Input Energy

Harvested energy can be conveniently calculated by using the input energy W_{in} once the conversion efficiency is known. The output electric (harvested) energy W_e is obtained as Eq. 3.1 by W_{in} multiplied by the efficiency. Thus, it is important to estimate available strain energy accurately. This available strain energy is considered as the input to an EH, and the input mechanical energy density w from the strain of the substrate is estimated by

$$w = \int_{\epsilon_1}^{\epsilon_2} \sigma d\epsilon = \int_{t_1}^{t_2} E\epsilon \dot{\epsilon} dt \quad (3.10)$$

where ϵ , σ , and E are strain, stress, and Young's modulus of an EH respectively. This relation provides the strain energy when an EH is stretched or compressed from ϵ_1 to ϵ_2 by external forces exerted on its body. At times when the input energy is considered, an EH is forced in the opposite direction of EH passive deformation. When an EH contracts from its expansion, there is no need for an input force for this motion, and vice versa (or the mechanical energy released back from an EH to the environment is not considered as the input energy.) Thus, the total input energy occurs only when the

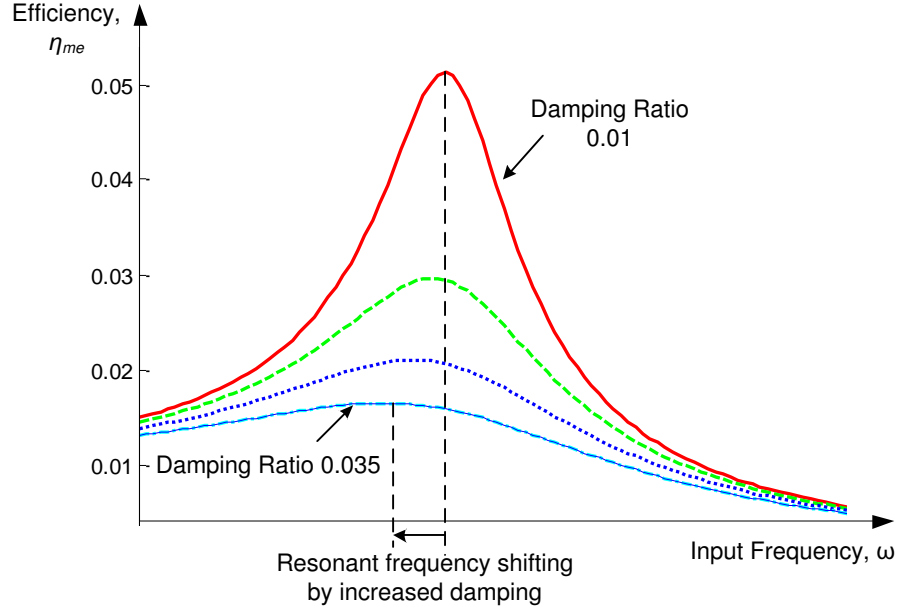


Figure 3.3: Illustration of trends of the conversion efficiency over a range of damping coefficients; the efficiency depends on the input frequency and its maximum occurs at the material damped natural frequency, which shifts lower as damping increases.

strain and strain rate are in the same sign. In this way, the conversion efficiency can be derived from the input mechanical vibration exerted on. The total input energy W_{in} to an EH is given by

$$W_{in} = \begin{cases} V \int_{\epsilon_1}^{\epsilon_2} E \epsilon \dot{\epsilon} dt & \text{if } \epsilon \dot{\epsilon} > 0 \\ 0 & \text{else} \end{cases} \quad (3.11)$$

where V is the volume an EH.

3.3.1 Harmonic Excitation

Consider an EH that is under a single dominant harmonic excitation with a frequency f and a mean-to-peak strain amplitude ϵ_a (unitless): $\epsilon(t) = \epsilon_a \sin(2\pi ft)$. Input strain

energy of one cycle $W_{in}^{(1)}$ can be calculated based on Eq. 3.11.

$$W_{in}^{(1)} = VE\epsilon_a^2 2\pi f \left(\int_0^{\frac{1}{4f}} \sin 2\pi ft \cdot \cos 2\pi ft dt + \int_{\frac{1}{2f}}^{\frac{3}{4f}} \sin 2\pi ft \cdot \cos 2\pi ft dt \right) = 2 \cdot \frac{1}{2} VE\epsilon_a^2. \quad (3.12)$$

Given the excitation frequency f and the total time of excitation δt , then the number of excitation cycles n is

$$n = f \cdot \delta t. \quad (3.13)$$

Combining Eqs. (3.12 and 3.13), the strain energy input for n cycles $W_{in}^{(n)}$ is

$$W_{in}^{(n)} = n \cdot 2 \cdot \frac{1}{2} VE\epsilon_a^2 = f\delta t \cdot VE\epsilon_a^2. \quad (3.14)$$

And multiply the EH efficiency η_{me} to Eq. (3.14) to estimate the amount of harvested energy W_{EH} , then we get

$$W_{EH} = \eta_{me} \cdot VE \cdot \epsilon_a^2 f \cdot \delta t. \quad (3.15)$$

3.3.2 Random Excitation

When an input strain is arbitrary, no explicit form of a function for the strain is available. In this case, the input strain in Eq. (3.11) can be discretized in time. As in the previous section, the effective strain energy is considered as the energy from the extraneous source, which makes the structure stretched or contracted. In other words, from Eq. (3.11)

$$W_{in} \approx \begin{cases} VE \sum_{k_1}^{k_2} \epsilon_k \cdot \frac{\epsilon_k - \epsilon_{k-1}}{\Delta t} \Delta t & \text{if } \epsilon_k \cdot (\epsilon_k - \epsilon_{k-1}) > 0, \\ 0 & \text{else.} \end{cases} \quad (3.16)$$

See Appendix A for more examples to calculate input energy.

3.4 Experiments for the Conversion Efficiency

The conversion efficiency is a fundamental parameter to estimate harvested energy using the input energy in Eq. 3.1. It is particularly advantageous to obtain this efficiency experimentally when the EH physical properties such as the structural damping or piezoelectric coupling coefficients (see Eqs. 3.4 and 3.5) are not certain. This section overviews the experiment design and its setup.

3.4.1 Experiment Design and Set-up

A commercial EH, MFC M2814P2 (31-mode) from Smart Material [80], is employed for this study. The volume and its Young's modulus of the EH are 117.60 mm^3 and 30.34 GPa found in the data sheet. Figure 3.4 depicts a sketch of the experimental set-up of a beam. The EH is attached to a host structure, a vertical cantilever beam made of aluminium. To have a uniform strain area for the EH, a tapered beam was designed, having wider width to the root. A few advantages of using a cantilever beam are flexibility of setting-up (using only one side constraint) and low external forces required to have equivalent strain level to the four-points bending (better controllability). And so, for a cantilever set-up, a low-strength material can be used. The beam dimension is $50 \times 203 \times 2 \text{ (mm)}$. Decreasing width compensates decreasing moments of inertia, thus a constant strain field in the triangle area can be secured. Details about the strain calculation for the design and strain conversion to the tip displacement with its validation can be found in the appendix A.

The beam is excited at the tip by a linear motor with a known input amplitude and frequency. The beam is constrained at its root. An EH is connected to a variable-resistor, and the EH performance is recorded in voltage and current over the circuit connected to the EH. In this study, $200 \text{ k}\Omega$ load resistance was chosen for the best performance of the selected EH (which matches the EH impedance). In order to track beam deformations in real time, two strain gages are installed on the top and bottom of the EH area installed on the beam. Figure 3.5 shows a picture of the beam. For a comparison, a P1 type (33-mode) of the MFC is installed in the front and a P2 type (31-mode) is in the back of the beam. Figure 3.6 shows the overall set-up of the experiment. Voltage and current are measured in an electromagnetic shield cage.

Two types of loadings were imposed in this experimental study. First, the EH was driven by various single harmonic wave inputs. The input amplitude was fixed to 10 mm tip displacements ($\sim 400 \mu\epsilon$ mean-to-peak amplitude), but frequencies were varying as $0.2, 0.5, 1, 5, \text{ and } 10 \text{ Hz}$. Second, an input strain profile expected for a full-size wind turbine was considered. This strain input typically has a low frequency (less than 1 Hz) and random fluctuations. For this objective, strain data of 5 MW offshore wind turbine from the FAST [3] simulation were taken for an input. Figure 3.7 shows a time trace plot for an strain input versus strain measurements of the beam. As shown in the figure,

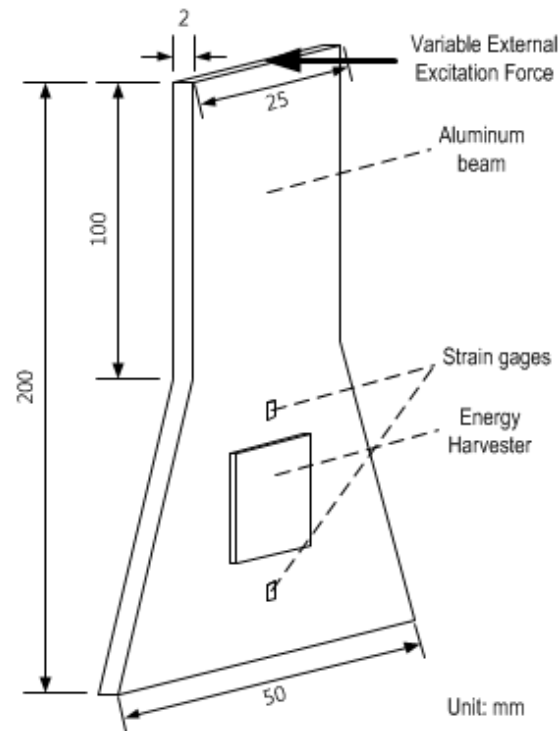


Figure 3.4: A Sketch of the Experimental Set-up Specifications: The beam is constrained as a cantilever at its root, and the top is actuated by a linear motor.

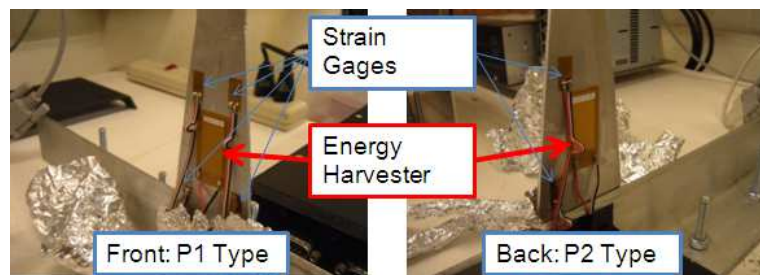


Figure 3.5: Two types of MFCs (P1 and P2 types) are installed in the front and back of the beam.

the beam is well tracking the command input of simulation results of blade strain.

The experiment process for the FAST test is shown in Figure 3.8. A user can specify the simulation environment including a wind turbine type, wind speed, turbulence intensity. The information for strains of three blades for a number of discrete locations

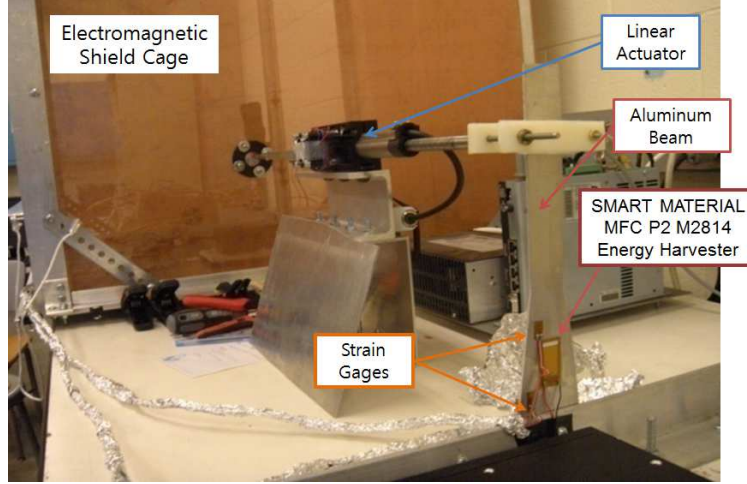


Figure 3.6: Overall Experimental Setup; a linear motor actuates the tip deflection of the beam. The EH installed on the beam is wired to a resistor, where voltage and current in the circuit are measured.

in the longitudinal direction is available. The FAST provides discrete bending moments data in a time series in edge/flapwise directions. The moments are calculated to strains, and strains are converted to tip displacements. The beam is excited by a linear actuator dictated based on calculated displacements. For this experiment, a local strain profile of a site in a distance of approximately 60% of the blade length from the hub was used. Its dominant modal frequency and amplitude—calculated by Fast Fourier Transform—were 0.2 Hz and 195 μ -strain respectively (,which is corresponding to 5.35 mm tip displacement). The result of this random excitation is compared to the efficiency from a 5 mm pure harmonic input at 0.2 Hz.

3.5 Experimental Results

The mechanical-to-electrical conversion efficiency is studied experimentally. The harvested energy W_e is calculated by measured voltage v and current i in the circuit of the load side as

$$W_e = \sum_{k=1}^{n_d} v(k)i(k) \frac{\Delta t}{n_d} \quad (3.17)$$

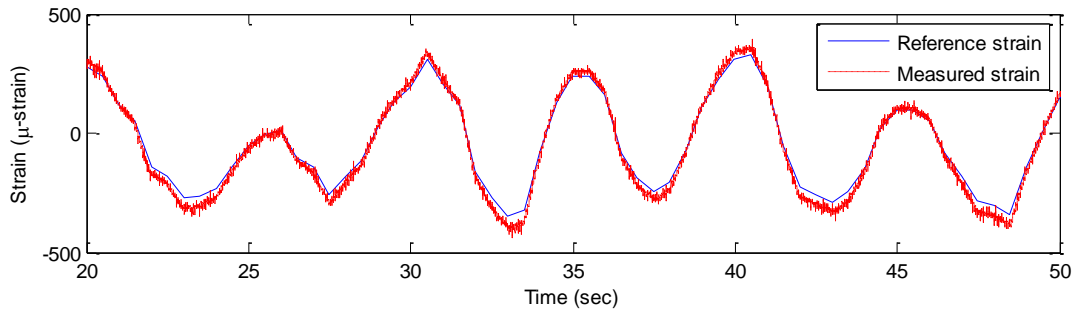


Figure 3.7: Strain command input for a 5 MW wind turbine from the FAST simulation is shown in a blue solid curve. Strain measurements (dashed red line) of the beam follow well the command input.

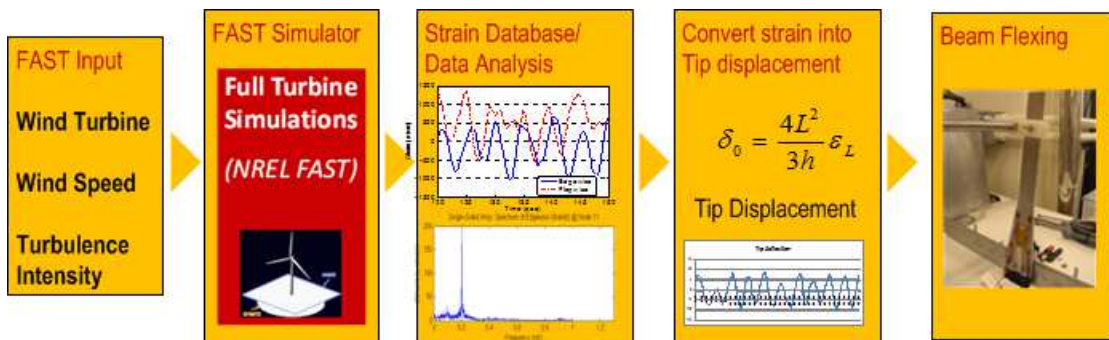


Figure 3.8: Experiment Process for Wind Turbine Blade Flexing

where Δt and n_d are the experiment total time and the total number of measurements respectively.

3.5.1 Harmonic Excitation

The experimental conversion-efficiency is the ratio of the input mechanical energy and the output electric energy as Eq. 3.1. The input energy for this harmonic case is calculated from Eq. 3.14. Input and output powers are calculated from strain gage and voltage/current measurements respectively. For a pure harmonic strain input, closed-circuit voltage/current measurements are shown in Figure 3.9. As shown in the figure, voltage and current are of pure harmonic cycles at the same frequency as the input.

The procedure is repeated for a range of input frequencies, and Table 3.1 summarizes the EH performance for given conditions. As expected from the analytic study of the efficiency in section 3.2, the efficiency increases with frequency up to 2.5 % at 5 Hz, and at 10 Hz, the highest frequency tested, the efficiency is 2.34%. For an aluminium beam with natural frequency of approximate 20 Hz, the frequency for the maximum conversion efficiency of the EH (see Eq. 3.8) is approximately estimated between 3 and 6 Hz (EH depending on the damping ratio). The manufacturer reports 2.5-4% total (maximum) energy conversion efficiency, which is also consistent with the experimental findings reported herein.

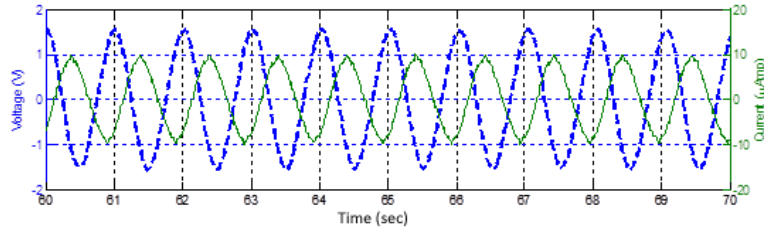


Figure 3.9: Voltage(dashed) and Current(solid) Outputs of the MFC EH for a Sine Excitation of a 10 mm ($\sim 400 \mu\epsilon$) mean-to-peak amplitude at 1Hz

3.5.2 Random Excitation

The EH was also tested for a 5 MW wind turbine blade strain input (Figure 3.8). For this random excitation, the efficiency was calculated from the input energy equation in Eq. 3.16. Figure 3.10 shows the FAST command strain input (solid) oscillates with an

Table 3.1: Energy Harvester Efficiency for Various Input Frequencies

Freq [Hz]	W_{in} [mJ]	W_e [μ J]	Efficiency [%]	Input Disp. [mm]
0.2	0.29	1.2	0.42 %	5
0.5	2.85	33.6	1.18 %	10
1	5.71	101.6	1.78 %	10
5	28.54	732.6	2.57 %	10
10	57.09	1338.2	2.34 %	10

amplitude of approximately $\sim 200 \mu$ -strain and the measured voltage output (dashed) follows the strain input. The figure confirms that the strain profile makes a similar pattern to the voltage output, with some irregular fluctuations occurring during the cycles. In Figure 3.11, time traces of voltage and current outputs by the FAST input are shown and a similar working practice of the EH is observed. For the FAST setup, the efficiency was $\sim 0.96\%$ which is more than double the efficiency of a pure 0.2 Hz sinusoid input. This is partly due to other minor modal components (i.e. random fluctuations). In general, a shaky environment generates more energy and greater electricity generation can be expected.

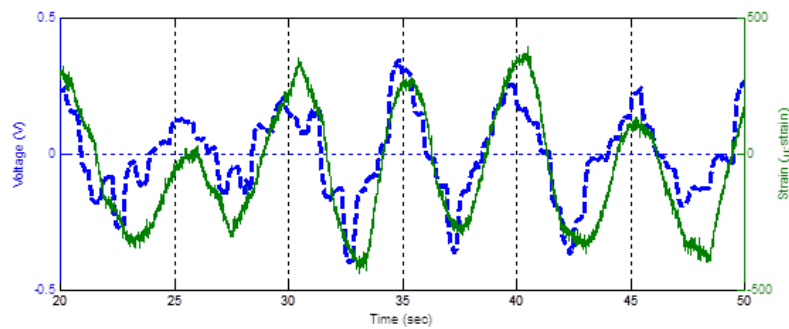


Figure 3.10: Voltage Output(dashed) and Strain Input(solid) of the EH for a Blade Strain Profile

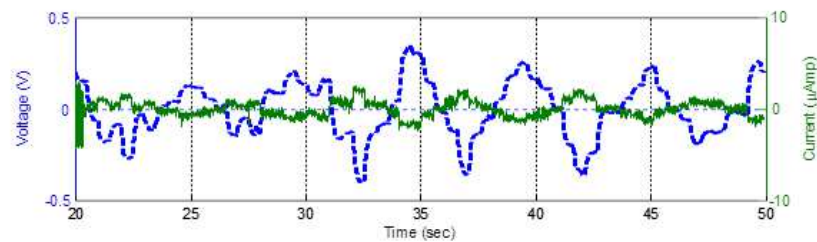


Figure 3.11: Voltage(dashed) and Current(solid) Outputs of the EH for a Blade Strain Profile

3.6 Conclusions

In this study, a methodology to obtain an experimental conversion efficiency of a piezoelectric energy harvester (EH) operating at low frequency broad band excitation and experimental results were presented. A tapered cantilever beam with a triangular area was designed to have a uniform strain field for testing an EH. The beam was excited by a linear motor at various input frequencies of a single harmonic signal. The tip displacement was prescribed to create a desired strain value at the EH located at the root of the beam. From the experiments, the efficiency ranged from 0.4 to 2.6% for frequencies of 0.2-10 Hz. A low frequency pure sine wave input (0.2 Hz) was compared to a realistic rotor blade strain input obtained through FAST simulation for a 5 MW wind turbine broad band excitation at dominant frequency of 0.2 Hz. The conversion efficiency ($\sim 0.96\%$) with the FAST strain input was almost double that of the efficiency ($\sim 0.42\%$) at a 0.2 Hz pure sine input. For the EH selected in this study, a conservative 0.5% efficiency can be used for a full-size wind turbine such as a 5 MW offshore model.

Chapter 4

Wireless SHM of Blades Using an EH as a Sensor

4.1 Summary

Structural Health Monitoring (SHM) of wind turbine blades is critical to improve the reliability of wind turbines. A health monitoring algorithm was developed that utilizes energy harvesters as sensors. An accumulated energy sensor is described in which an energy harvester mounted on the surface of the wind turbine blade converts low frequency vibrational strain energy from the blade to electrical charge, that is subsequently stored to power an RF transmitter. The premise of this sensing approach is that the timing of data output from the RF transmitter, which is tied to the charging time, is indicative of the structural health. The time between data transmission pulses will be reduced if the blade stiffness decreases. The SHM algorithm compares data transmission time for the three blades to identify the onset of blade damage. To demonstrate the effectiveness of the algorithm, an expected energy harvester signal transmission rate is established from blade strain data from a 2.5 MW wind turbine. The transmission rates for the three blades are compared to establish a threshold for “healthy” blades. Simulated damage corresponding to approximately 20% increase in harvested energy can be detected by the SHM algorithm.

4.2 Introduction

The DOE has set a goal of “20% wind energy by 2030” [47]. Reduction in operating and maintenance costs for wind turbines has been identified as a major challenge to achieving this goal. Wind turbine maintenance is a particular challenge because wind turbines are often located in remote regions (including offshore). Structural Health Monitoring (SHM) is a promising approach that can enable preventative maintenance, reduce down time and significantly reduce life-cycle costs [30]. While failure can occur in any structural component, one of the most common and critical components to fail is the wind turbine blade [9]. It is particularly challenging to continuously monitor blade health: (1) the blades are quite long and an extensive network of sensors is required; and (2) the blades are rotating, posing challenges to delivering power to and receiving data from the sensor network.

A novel sensing and SHM system is proposed. The system is comprised of a network of discrete sensor nodes. Each wireless node includes an energy harvester to convert vibrational strain energy from the blade to electrical charge and an RF transmitter circuit. The electrical charge from the energy harvester is stored to power an RF transmitter. The RF transmitter wirelessly communicates a single pulse to a centralized monitoring system in the turbine nacelle when sufficient electrical charge has been stored. The premise of this sensing approach is that the timing of data output from the RF transmitter, which is tied to the charging time, is indicative of the structural health. In a damaged blade, changes in the stiffness (associated with damage) will lead to a change in blade strain, resulting in a change in the timing of the RF pulses.

To demonstrate the effectiveness of the proposed sensor-algorithm, a study is presented that utilizes blade strain data from the Eolos 2.5 MW wind turbine installed at the University of Minnesota. Fiber optic strain sensors were installed at several locations on each of the three blades of the Eolos turbine. At this stage of the research, energy harvesters have not yet been installed on the turbine blades. Hence, the low frequency strain data are converted to simulated energy harvester pulse transmission data. These simulated energy harvester data are the basis for evaluation of the health monitoring algorithm.

4.3 Background

4.3.1 Health Monitoring of Wind Turbine Blades

Structural health monitoring⁵ is the process of implementing a damage detection strategy for an engineering structure. SHM algorithms have been well-studied because structural damage can have significant safety impacts. The literature on SHM includes many applications to wind turbine blades [12, 27–32, 34–36]. Methods include acoustic emission, thermal imaging, ultrasonic methods, modal approaches, fiber optic methods, laser Doppler, electrical resistance, and X-rays [27]. Vibration-based SHM methods [28, 29] seem most appropriate for the proposed architecture. Vibration-based SHM can be largely categorized into frequency/modal domain and time domain analysis. Some of the previous work in this area is briefly reviewed. Zayas et. al [33] developed an impedance-based SHM system by PZT sensors and actuators. The SHM system can detect damage inside a blade but a sensor must be placed close to the damage. Pitchford et al. [35] also studied impedance-based SHM using MFC piezoelectric materials. While modal testing, MFC patches are used for monitoring material behavior with an active impedance method. Ghoshal et al. [30] presented four blade health monitoring techniques: transmittance functions, ODS, resonant comparison, and wave propagation. The feasibility to detect damage was indicated by using piezoceramic patches for excitation and a scanning laser Doppler vibrometer or piezoceramic patches to measure vibration. Schulz [36] suggested a smart sensor system to actively detect a fault in a composite blade. White et al. [31] presented a SHM method for a lab-scale carbon composite wind turbine blade, TX-100. In this paper, several accelerometers were deployed and they used virtual forces, transmissibility, and time-frequency analysis. In Ref. [12], their methods were shown as not effective on damage detection located farther than 2 meters from a sensor. Rumsey et al. [12] studied a few direct measuring methods based on strain gages and acoustic emission sensors. They concluded unique sound events were captured when damage occurred and strain energy reduction over fatigue cycles was observed as damage increased.

In summary, there is a large body of work on SHM for wind turbine blades. Most of these techniques employ a small number of sensors to detect structural damage. The use of energy harvesting sensors with wireless communication eliminates the need for

costly wiring which requires maintenance. As a result, it is feasible to implement an array of many sensors on each of the three turbine blades.

4.3.2 Energy Harvester as a Sensor

It is important to estimate the strain energy available for powering SHM sensors. The strain energy density w_{strain} (J/m^3) at a given strain ϵ_1 (unitless) is given by the fundamental equation:

$$w_{\text{strain}} = \int_0^{\epsilon_1} \sigma d\epsilon \quad (4.1)$$

where σ is the stress (Pa). If the Young's modulus E (GPa) is constant then the strain energy density (J/m^3) can be expressed entirely in terms of strain as

$$w_{\text{strain}} = \int_0^{\epsilon_1} E\epsilon d\epsilon \quad (4.2)$$

This relation provides the strain energy density at a given strain ϵ_1 . An EH, when subjected to time-varying strains, converts a fraction of the mechanical strain energy input into usable electrical energy. The EH efficiency η (unitless) is defined as the energy conversion ratio from mechanical input to electrical energy output. This efficiency is typically on the order of 10^{-2} . Assuming η is known, the harvested energy is estimated by the input energy multiplied by η . External forces are converted to electric energy when the EH is stretched or compressed. The input energy is calculated from strain by considering only conditions when the strain $\epsilon(t)$ and the strain rate $\dot{\epsilon}(t)$ are the same sign. Thus the total input energy density w_{in} to the harvester is given by

$$w_{\text{in}} = \int_0^{t_1} w_{\text{instant}}(\epsilon(t), \dot{\epsilon}(t)) dt \quad (4.3)$$

where the instantaneous energy density w_{instant} is

$$w_{\text{instant}}(\epsilon, \dot{\epsilon}) = \begin{cases} E\epsilon\dot{\epsilon} & \text{if } \epsilon\dot{\epsilon} > 0 \\ 0 & \text{else.} \end{cases} \quad (4.4)$$

Explicit formulas for the harvested energy can be derived if the strain is sinusoidal with frequency f (Hz) and peak amplitude (mean to peak) of the strain ϵ_a (unitless) (see Appendix). For example, if $\epsilon(t) = \epsilon_a \sin(2\pi f t)$, then the harvested energy density is

$$w_{\text{EH}} = \eta E \cdot \epsilon_a^2 f \cdot \delta t. \quad (4.5)$$

The harvested energy density w_{EH} can be converted to a total harvested energy W_{EH} (J) by multiplying by the volume V (m^3) of the EH

$$W_{EH} = \eta V E \cdot \epsilon_a^2 f \cdot \delta t . \quad (4.6)$$

The charging time δt (sec) is the time required to charge the capacitor (part of the RF circuit) and will also define the time between bursts of data transmission/acquisition. The magnitude of strain and frequency will depend on the wind turbine blade geometry and operating conditions.

As noted, the energy available for harvesting depends on the strain and the frequency of vibration; and harvesting capability depends on the type and the design of an EH (Eq. 4.6). Thus it is useful to define the power available P_{avail} (W/m^3) and the EH design factor K_{EH} (m^3) as

$$P_{avail} = E_0 \epsilon_a^2 f , \quad (4.7)$$

$$K_{EH} = \eta V \frac{E}{E_0} \quad (4.8)$$

where E_0 is the nominal modulus of an EH material (GPa). These definitions separate the design properties of a given EH (given in volumetric units) from the conditions in which the EH operates as specified by the power density P_{avail} . By using this measure of available power, simulation strain data can be compared for various turbines and under various operating conditions. For the purpose of comparison, a modulus of $E_0 = 1$ GPa is taken in all plots and data reported herein. Values can easily be scaled to evaluate other harvester materials. In summary, the harvested energy can be decomposed into an internal factor (K_{EH}) and external source (P_{avail}) and charging time δt . Eq. (4.6) is simplified as

$$W_{EH} = K_{EH} \cdot P_{avail} \cdot \delta t \quad (4.9)$$

When using the energy harvester as a sensor, the energy available from harvested W_{EH} must be sufficient to charge the capacitor in the RF circuit W_{RF} . The energy required to send a single tone burst W_{RF} is set by the RF circuit/capacitor configuration, and is a fixed amount on the order of micro Joules. In this configuration, the charging time δt is also the time between transmission pulses. Thus, because the energy required to send a single pulse is fixed, the charging time (and time between pulses) δt is reduced when the power available P_{avail} increases.

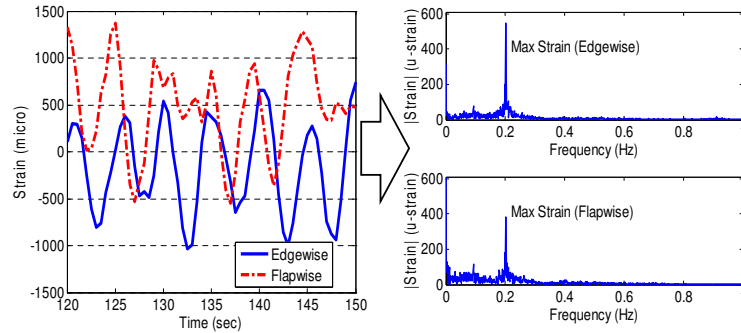


Figure 4.1: Strain vs. Time at 15.9 m from hub (L) and Single sided amplitude spectrum in frequency of each flexing mode (R): Data shown for NREL offshore turbine at 24 m/s wind speed and low turbulence.

4.3.3 Available Strain Energy

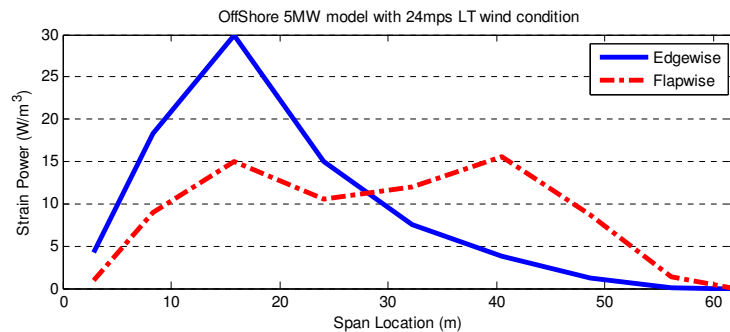


Figure 4.2: Edge/Flapwise strain power available in an offshore blade as a function of blade location. Data are obtained during operational cycles corresponding to the maximum peak amplitude. ($E_0 = 1$ GPa)

In our earlier work [81], the strain energy available was estimated for three wind turbines (a CART3 600 kW, a WindPact 1.5 MW and a 5MW offshore wind turbine) and various wind conditions (6 to 24 m/s at high and low turbulence). For the range of wind turbine sizes and wind conditions considered, the P_{avail} ranges from 1 to 30 W/m³. FAST [3] simulation results for the 5MW NREL offshore wind turbine operating under wind conditions of 24 m/s at low turbulence are shown in Figure 4.1. Figure 4.1 shows

strain data in both edgewise and flapwise bending over a 30sec time window at a location 15.9m from the rotor hub (left). Fast Fourier Transforms computed for each bending mode over a longer time window are also shown (right). As shown in Figure 4.1, the peak amplitude of the edgewise strain is ~ 550 micro-strain and the amplitude of the flapwise strain is ~ 390 micro-strain. These edgewise and flapwise strains are used as RMS amplitudes of ~ 390 and ~ 280 micro-strain respectively in determining the power available for the energy harvester. The strain varies with time at a periodic rate of ~ 0.2 Hz, corresponding to the rotational frequency of the turbine at these wind conditions. Figure 4.2 shows the corresponding maximum edgewise and flapwise P_{avail} (calculated from Eq. (4.7)) along the span of the blade. The maximum edgewise P_{avail} , ~ 30 W/m³, occurs at a distance 15.9 m from the blade support (at the nacelle). The flapwise P_{avail} has two peaks, 15 W/m³ at 15.9 m. and 16 W/m³ at 40.5 m. This profile of P_{avail} along the blade length is typical for the wind turbine sizes and wind conditions considered.

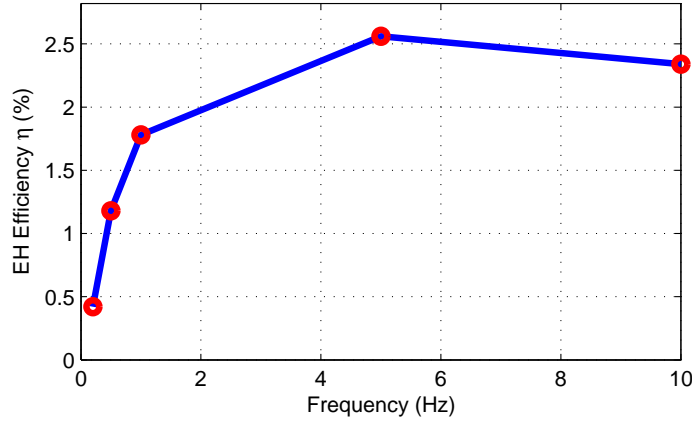


Figure 4.3: Experimental result of EH conversion efficiency over input frequency (200 $k\Omega$ load resistance and 200 $\mu\epsilon$ input peak amplitude)

In this study, a data transmission energy requirement W_{RF} of 92.4 J was selected, corresponding to the power requirement to transmit a signal to a data acquisition board (DAQ) in the nacelle via a commercially available wireless transmission module (EH-link from Microstrain17). The EH design factor K_{EH} is experimentally evaluated for an off the shelf energy harvester, the Smart Material [80] M2814P2 type MFC with a surface area of 28 mm \times 14 mm by 0.3 mm thick. The material modulus E is 30.34

GPa. It is well known that the piezoelectric EH performance depends on the load resistance, input amplitude and frequency. Thus, the energy harvester efficiency was determined under conditions that are expected for wind turbine applications. Figure 4.3 shows energy harvester efficiency for tests performed at $200 \mu\epsilon$ of input peak amplitude over frequencies ranging from 0.2 to 10 Hz. At 0.2 Hz, the energy harvester efficiency is approximately 0.4%. Under these conditions, K_{EH} is 14.27 mm^3 . Given the power requirement for a single pulse ($W_{RF} = W_{EH} = 92.4 \mu\text{J}$), the charging time when $P_{avail} = 30 \text{ W/m}^3$ is 3.6 minutes.

4.4 Approach

In this section, a health monitoring algorithm for detecting blade damage is described. An overview of the approach is illustrated in Figure 4.4. EHs are installed at the same locations on the three blades. From blade vibrations (first row in Figure 4.4), EHs accumulate strain energy (second row). When the accumulated strain energy is sufficient for transmitting a single data pulse, the transmitted signal is received by the DAQ system and the time is recorded (third row). The time intervals for each of the three EH pulse transmissions are compared to each other. The SHM algorithm determines whether a wind turbine blade is damaged based on the difference in the pulse timing interval among the three EHs. EHs can be installed at many locations on each blade and this monitoring algorithm can be repeated for each set of three measurements obtained from the same blade location. This enables detection of the damage location.

4.4.1 Damage Model

Matrix cracking is common in composite materials and initiated by multiple factors including fatigue loading. As shown in Figure 4.4.1 (left), the stiffness decreases as the crack density increases. Thus, matrix cracking is modeled as a loss in stiffness.[82] A local loss in stiffness will increase the strain (and subsequently P_{avail}) at that location. As the blade is cyclically loaded, damage will accumulate. A simple damage model of matrix cracking is shown in Figure 4.4.1 (right) as a function of the number of loading cycles. This model introduces the concept of a damage factor g_D that tracks the stages of matrix crack growth as the part is cyclically loaded. The damage factor is initially

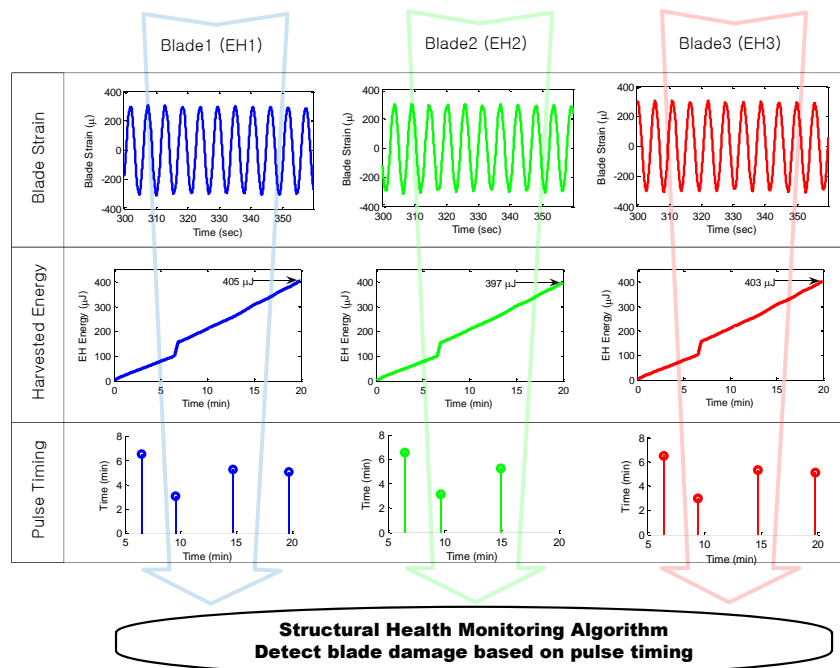


Figure 4.4: Construction of Model-free Structural Health Monitoring for Wind Turbine Blades

$g_D=1$, corresponding to no damage, and increases to $g_D=1.2$ corresponding to a 20% increase in strain (or 20% loss in stiffness). Because the strain energy harvested will increase with damage, Eq. (4.3) is modified to account for the damage that accumulates with each cyclic load.

$$w_{in} = \int_0^{t_1} g_D(t) \cdot w_{\text{instant}}(\epsilon(t), \dot{\epsilon}(t)) dt \quad (4.10)$$

This integral relation is more general than Eq. (4.6) in that it includes the factor g_D (unitless) to model damage. Eq. (4.10) can be discretized with a step size of Δt (sec) to accommodate an arbitrary strain profile:

$$w_{in} \approx \sum_{k=1}^n g_{D,k} \cdot w_{\text{instant},k} \cdot \Delta t \quad (4.11)$$

where

$$w_{\text{instant},k} = \begin{cases} E\epsilon(t_k) \cdot \frac{\epsilon(t_k) - \epsilon(t_{k-1})}{\Delta t} & \text{if } \epsilon(t_k) \cdot (\epsilon(t_k) - \epsilon(t_{k-1})) > 0 \\ 0 & \text{else .} \end{cases} \quad (4.12)$$

The total harvested strain energy given the volume of the EH V and the efficiency η is

$$W_{\text{EH}} \approx \eta V \sum_{k=1}^n g_{D,k} \cdot w_{\text{instant},k} \cdot \Delta t \quad (4.13)$$

Eq. (4.13) applies for more general strain conditions and not simply for single harmonic vibrations as considered in Eq. (4.6). The discrete-summation is used to approximate the continuous integral in the simulations and this allows for the damage factor to change with each cycle.

4.4.2 Triple Redundancy Fault Detection

As described in the background section, there is limited vibrational power that can be harvested. In particular, for the range of wind conditions and turbine sizes studied by Lim et. al [81], the maximum available power P_{avail} is no more than 30 W/m³ even under the most favorable operating conditions. Given current energy harvester efficiencies, it would take approximately 4 minutes to store sufficient energy to simply wirelessly transmit a single pulse. Additional energy would be required to take a strain

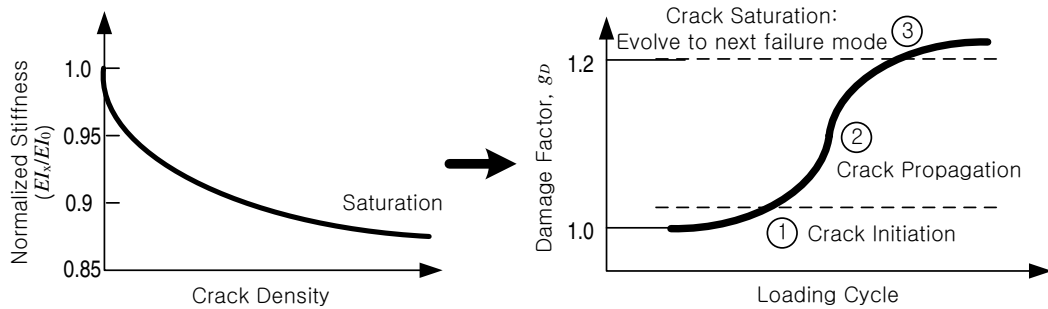


Figure 4.5: Stiffness Reduction Model (L)20, Simple Damage Model for the Matrix Cracking (R)

or accelerometer measurement. As a consequence, it is not possible to use high sample rate SHM algorithms with sensors powered by a vibrational energy harvester.

The essential idea of the proposed health monitoring algorithm is to compare identical measurements from the three individual blades. Specifically, the transmission time intervals from the sensing nodes at identical locations on the three turbine blades is compared. This transmission time interval between pulses is a direct measurement of the rate of harvested power. An individual timing measurement is then deemed “unhealthy” if it differs from the remaining blades by more than a specified threshold. The hypothesis is that a damaged blade will yield a sufficiently different measurement than a healthy blade. This triple redundant design is model-free and is commonly used in the aerospace industry [83–85] to achieve high levels of reliability. The triple redundancy enables detection of a single blade failure because the failed blade yields outlier measurements in comparison to the two healthy blades. This approach relies on three key assumptions. First, it is assumed that the three blades are initially healthy. Second, it is assumed that two or more blades do not fail in the same way at the same location. Third, the three blades are assumed to have similar wind loading conditions when averaged over time. In the case of matrix cracking, higher available power P_{avail} leads to a shorter transmission time interval. In this way, the damage can be detected with low sampling frequency because the speed of damage progression is much slower than the sampling period.

Eq. (4.11) is the general relation that can be used to model the time between pulse transmissions for any strain history and damage profile. The important point is that the time to charge the harvester for a pulse transmission depends on several factors including the harvester properties, installation configuration and loading conditions. For example, variations in the wind speed will change the vibrational energy P_{avail} and hence the timing of the pulses from energy harvesting sensors. However, it is assumed that all three blades operate in the same wind conditions. Hence, changes in wind conditions should lead to similar changes in the pulse time of the energy harvesting sensors located on all blades. Thus is useful to define a non-dimensional ratio to compare the pulse timings from each energy harvester. Let $\Delta t_i(t)$ denote the time difference between two most recent pulses received at time t from blade i . The time differences computed from harvesters on blades 1, 2, and 3 can be compared at time t using the following three ratios:

$$R_{1-2}(t) = \frac{\Delta t_1(t)}{\Delta t_2(t)}, \quad R_{1-3}(t) = \frac{\Delta t_1(t)}{\Delta t_3(t)}, \quad R_{2-3}(t) = \frac{\Delta t_2(t)}{\Delta t_3(t)}. \quad (4.14)$$

The use of non-dimensional ratios minimizes the effect of exogenous influences, e.g. wind conditions, thus enabling blade damage to be more easily detected in the processed data. The pulse ratios may not be unity even if all blades are healthy, i.e. blade timings can be different due to differences in sensor installation, individual harvester efficiency, etc. However, matrix cracking on a single blade will lead to higher available power P_{avail} and hence a shorter transmission time interval. Damage can be detected over time by noting that the transmission time ratios for a single blade will diverge from the initial values. For example, damage in blade 3 will cause more frequent transmissions and thus shorter transmission time intervals. As a result the ratios computed using blade 3, i.e. R_{2-3} and R_{3-1} , will diverge from their initial values. Deviations sufficient to indicate blade damage can be detected by a simple threshold. The precise implementation is as follows. First, an initial dataset is recorded under the assumption that each blade is healthy. The transmission time ratios $R_{i-j}(t)$ ($i=1,2,3$ and $j \neq i$) obtained from this initial dataset are averaged in time to obtain the constant ratio \bar{R}_{i-j} that corresponds to healthy operation. Damage is detected on blade i ($=1,2,3$) if $|R_{i-j}(t) - \bar{R}_{i-j}| > T$ for $i \neq j$ where T is the detection threshold. This proposed detection method is evaluated in the next section using experimental strain data from a utility-scale turbine combined

with the model to simulate the harvester in both healthy and unhealthy conditions.

4.5 Results and Discussion

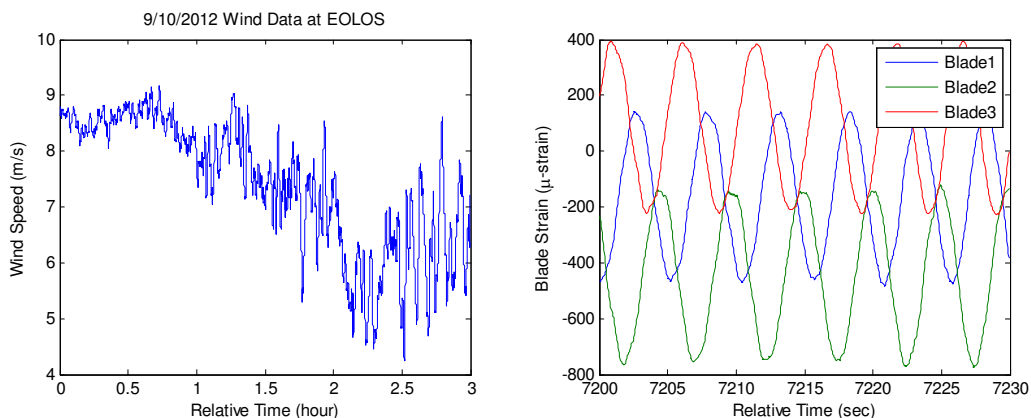


Figure 4.6: Wind Data (L), Edgewise Strain Data from Leading Edge of Three Blades at the Root (R)

4.5.1 Eolos Wind Turbine

The Eolos [56] Wind Energy Research consortium was established in 2010 by the University of Minnesota and includes the Wind Research Field Station located at the University of Minnesota’s UMore Park facility. In the summer of 2011, a state-of-the-art 2.5MW C96 Clipper Liberty Wind Turbine [86] was installed at UMore Park. The turbine has a rotor diameter of 96 meters and tower hub height of 80 meters. The turbine includes fiber optic strain gages and accelerometers installed at various points on the three blades and tower base for research purposes. In addition, a 130 m tall meteorological tower, located upwind of the turbine, is instrumented with an array of advanced wind measurement technologies including sonic anemometers, temperatures sensors and cameras. All data collected at the site, including the turbine, blade, foundation, and met tower are transmitted back to the university campus through high-speed internet for real-time viewing and sharing. Blade strain and wind data (obtained from

an upstream met tower) from the Eolos turbine are used in this paper to evaluate the proposed health monitoring algorithm. For each blade, strain at up to 10 locations is continuously recorded at a frequency of 20 Hz. Wind data and turbine operating conditions, sampled at 1 Hz, are recorded and time stamped to correspond to the strain data. An example of data obtained from the Liberty turbine at the Eolos Field Station is shown in Figure 4.5. It shows data recorded for three hours on September 10th, 2012 (left) and magnified strain data for 30 seconds of the same day (right). Strain data are from three strain gages at the same locations (root leading edge) of three blades. As shown, strain values of each measurement are asynchronously periodic and they have dissimilar non-zero means.

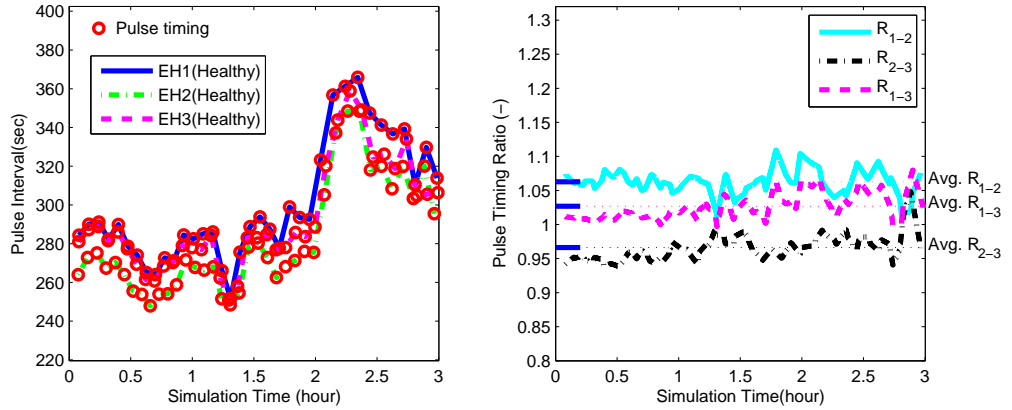


Figure 4.7: Pulse Timing of EHs (L), Ratio Factors of EHs (R)

4.5.2 Data Process using a Ratio Factor (Healthy Blades)

We expect the Eolos turbine blades to be “healthy” since the turbine has only recently been installed. Hence the data in Figure 4.5 represent healthy blades. The EH is modeled after the properties of the M2814P2 MFC which has a design factor of K_{EH} is 14.27 mm³. The signal pulse timing, shown in Figure 4.5.1 (left), was generated using the logged data shown in Figure 4.5 and a model of this EH. It is noted that the pulse timing interval increases after $t \approx 2$ hour due to the decrease in wind speed after $t \approx 1$ hour. The trends of three EHs pulse timings are similar despite this variation in the

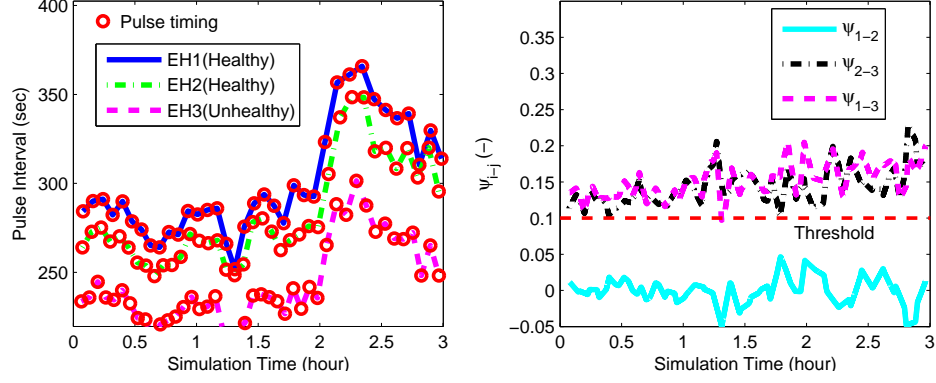


Figure 4.8: Unhealthy Blade Simulation: Pulse Timing of EHs (L), Ratio Factors of EHs (R)

working condition. Figure 4.5.1 (right) shows the three ratios defined in Eq. (4.14). This figure shows that the ratios remain relatively constant in spite of the variations and DC offsets in the strain measurements. In effect the long charging time (600 seconds here) averages out the short term variations and the signal DC offsets do not cause variations in the time interval ratios. As discussed above, the pulse timings may not be equal for each EH and hence the timing ratios are not equal to unity. The transmission time ratios shown in the right subplot of Figure 4.5.1 were averaged to obtain the nominal ratios \bar{R}_{i-j} that corresponds to healthy operation.

4.5.3 SHM Simulation for a Unhealthy Blade

After certain cycles of fatigue loading, cracks are saturated and g_D becomes some higher number than 1.0. This subsection considers the damage model in Figure 4.4.1 (right). A stage 3 cracking (saturation) damage is simulated in blade 3. This is simulated by changing the blade 3 damage factor in Eq. (4.11) from its nominal value ($g_D = 1.0$) to a value corresponding to a 20% increase in harvested energy ($g_D = 1.2$). The damage would typically occur over a long time scale and hence the damage factor is assumed to be constant on the time-scale of the simulation results shown here. The strain data shown in Figure 4.5 is again used to simulate the harvester pulse timings for the healthy

blades ($i = 1, 2$) and unhealthy blade ($i = 3$). The left subplot of Figure 4.5.1 shows the simulated pulse timings. The pulse timings for blade 3 have deviated from the healthy values shown in Figure 4.5.1. However, the damage signal is not easily discernable due to the variations in pulse intervals. The three ratio factors R_{i-j} are computed and then subtracted from the averaged initial values to obtain the deviations from healthy signals: $\psi_{i-j}(t) := R_{i-j}(t) - \bar{R}_{i-j}$. These deviations are shown in the right subplot of Figure 4.5.1. It is clear from this figure that the ratios computed with blade 3 deviate significantly and consistently from the healthy values. A threshold, chosen as $T = 1.1$, can be used to distinguish between small (healthy) values and larger (unhealthy) values. Further investigation is needed to understand the appropriate threshold level to balance the detection and false alarm rate of the proposed algorithm.

4.6 Conclusion

This paper described a structural health monitoring (SHM) algorithm to detect damage in wind turbine blades. The system relies on an accumulated energy sensor that harvests low frequency vibrational energy from the blade and wirelessly transmits a pulse once sufficient energy has been stored. The premise of this sensing approach is that the timing of signal transmissions is indicative of the structural health. The SHM algorithm identifies damage by comparing the transmission timing of sensors installed at the same location on the three blades. The effectiveness of the SHM algorithm was evaluated using experimental strain data from a 2.5MW turbine combined with a model of the energy harvester. These results indicate that simulated damage corresponding to approximately 20% increase in harvested energy can be detected by the proposed SHM algorithm. Future work will investigate the details of the algorithm including the threshold selection. In addition, more accurate damage models will be used to understand how the distance between the damage and sensor locations impacts the detection performance.

Nomenclature

E Young's Modulus of an EH, GPa ($E_0 = 1$ GPa)

K_{EH}	EH design factor, m^3
P_{avail}	Available strain power density, W/m^3
R_{i-j}	Pulse timing ratio between blades i and j
T	Damage detection threshold
V	Volume of an EH, m^3
W_{EH}	Harvested strain energy, J
f	Strain frequency, Hz
g_D	Damage factor
n	cycles of excitations
Δt	Discretization step time, sec
δt	Charging time, sec
w_{in}	Input strain energy density, J/m^3
ϵ	Mechanical strain, $\mu - \epsilon$
ϵ_a	Mechanical strain amplitude (mean-peak), $\mu - \epsilon$
η	Energy conversion efficiency
ψ_{i-j}	Pulse timing ration deviation by damage of R_{i-j}

Chapter 5

Algorithm for the Wireless SHM of Blades Using EHs

5.1 Summary

Wind turbine blade failure can be catastrophic and lead to unexpected power interruptions. In this paper, a Structural Health Monitoring (SHM) algorithm is presented for wireless monitoring of wind turbine blades. The SHM algorithm utilizes strain energy data that are acquired by piezo-electric energy-harvesters. The SHM algorithm compares the accumulated strain energy of sensors located at the same position on the three blades. This exploits the inherent triple redundancy of the blades and avoids the need for a structural model of the blade. The performance of the algorithm is evaluated using probabilistic metrics such as detection probability (True Positive) and false alarm rate (False Positive). The decision time is chosen to be sufficiently long that a particular damage level can be detected even in the presence of system sensor noise and wind variations. Finally, the proposed algorithm is evaluated with a case study of a utility-scale turbine. The noise level is based on measurements acquired from strain sensors mounted on the blades of a Clipper Liberty C96 turbine. Strain energy changes associated with damage from matrix cracking and delamination are estimated by a finite element model. The case study demonstrates that the proposed algorithm can detect damage with a high probability based on an inspection time period of approximately 50-200 days.

5.2 Introduction

The DOE has set a goal to achieve 20% of wind energy by 2030 [47]. To meet this goal, wind turbines must be extremely efficient and reliable. However, a wind turbine can fail by any structural component, and one of the most common and critical components to fail is the wind turbine blade. [9] Structural Health Monitoring (SHM) [28] is a promising method that can enable preventative maintenance, lower down time and significantly reduce life-cycle costs. [30] In SHM, sensor data are interpreted by an algorithm to detect the onset of damage in the structure. An effective SHM system can provide a warning sign to prevent a catastrophic failure, allowing the operator time to perform appropriate maintenance in advance.

Typical SHM sensing approaches include acoustic emission, thermal imaging, ultrasound, modal analysis, fiber optics, laser Doppler, electrical resistance, and X-rays. [27] The associated algorithms typically require comparison between healthy and damaged conditions, where the healthy states are a priori established for a particular component. For wind turbine applications, SHM approaches are often grouped as either global methods that consider the effect of local damage on overall behavior of the blade or local methods that capture local variations in blade structural properties. Global approaches often incorporate accelerometer data to identify mode shapes and/or deflection, and the system excitation is passive (i.e. derived from operational loads). For example, Adams et al. [87] used accelerometer data to characterize the mode shape of a healthy Horizontal Axis Wind Turbine (HAWT) blade in situ. Changes in the mode shape that are associated with reduced stiffness at the blade root, as simulated by a numerical model, were detected using a statistical approach that accounted for system noise. In a study by White et al. [31], accelerometers and force sensors were mounted side by side with the intent to estimate both the displacement and force data throughout the composite rotor blade. Modal data were extracted and the method was effective in detecting crack growth during dynamic loading. Schulz et al. [36] developed a smart blade concept in which a network of series connected PZT nodes acquired acoustic emissions data during crack growth. This passive system detected damage prior to any indication from surface mounted strain gages but system validation focused on small scale composite beam and plate samples. Earlier work from Schulz and coworkers (Goshal et al. [30]) considered

extracting blade mode shapes using Laser Doppler Vibrometer data, however this approach can not be readily implemented in the field. Rather than depend on a passive SHM approach, others have considered local SHM approaches that incorporate active damage detection: a system of piezo actuators and sensors are combined to evaluate changes in local material properties. One approach is to associate mechanical impedance of the structure with the electrical impedance response of a piezoelectric material. For example, Pitchford et al. [35] developed a self-sensing actuator: a single MFC patch serves as both actuator and sensor. The root mean square impedance response over a range of frequencies was correlated to changes in the local stiffness of the structure. Others (Zayas et al. [33], Light-Marquez et al. [88], Deines et al. [34]) have developed systems comprised of groups of PZT patches: a single patch is an actuator and multiple, nearby patches are sensors. Damage is detected by one of several signal processing approaches, such as time series analysis and frequency transfer functions, that consider the sensor responses given the input excitation. While there has been success in detecting damage using either global or local SHM approaches (Rumsey and Paquette [12]) there are some common challenges including: (1) establishing a baseline healthy state, either from a model or from the newly manufactured wing; (2) establishing a threshold that can account for system noise from temperature, wind variations, composite build data; (3) locating the sensors on the blade to ensure a high probability of detecting damage; and (4) achieving success requires high sampling rates with a number of sensors.

It is particularly challenging to use wired SHM for wind turbine blades: (1) the blades are quite long and an extensive network of sensors is required; and (2) the blades are rotating, posing challenges to delivering power to and receiving data from the sensor network. There are several examples of wireless SHM in civil infrastructure applications, [41–44] but these systems rely on batteries to power the sensors and signal transmission components. The primary drawback to using self powered energy sources is the combined power required for the sensors and the wireless transmitter/signal conditioning components. Lim et al. [89] proposed a novel, wireless SHM system for wind turbine blades that uses an energy harvester as both a sensor and power source. Low frequency strain energy, associated with gravity and wind loading, is captured by an energy harvester mounted on the blade surface and stored in a capacitor. A pulse is transmitted to a central receiver once the energy stored in the capacitor is sufficient to

power a wireless transmitter circuit. The timing of the pulses indicates the strain energy at the blade surface. The transmission time is compared for energy harvesters located on the three blades. Damage is identified by a model free SHM algorithm that utilizes the triple redundancy of the three blades. In the paper [89], the damage threshold was set as a 10% above the baseline “healthy” state transmission ratio data. While the approach is promising, performance metrics such as the probability of a false alarm or detection were not addressed.

In the present paper, a method to determine a threshold level that meets particular performance metrics for false alarm rates and detection probability is presented. The SHM sensors consist of the wireless energy harvester proposed in Lim et al. [89], but instead of a ratio of transmission times, the accumulated strain energy difference data (residuals) are used. This approach allows for the development of a stochastic model for structural health that can accommodate the inherent noise in sensor data. The fault detection scheme is comprised of two parts: a filter that generates scalar residuals carrying the information of the occurrence signal indicating the status of the monitored system and a decision logic to determine whether there is a damaged blade or not. The remainder of the paper is organized as follows. Section 2 reviews the hardware construction of the proposed SHM system and its working mechanism with an explanation for the EH. Section 3 presents a method designing an SHM system to satisfy probabilistic performance indices. To demonstrate its usefulness, section 4 gives a case study to apply the method developed in section 3 to full scale wind turbine blades. Finally, concluding remarks are provided in section 5.

5.3 Overview of Wireless SHM System

The SHM system consists of discrete sensor nodes installed at various points along the span of each blade (Figure 5.1). The sensing nodes consist of an EH, RF transmitter, and capacitor for energy storage. These nodes are installed at identical locations on each blade to enable cross-comparison of the measurements. Figure 5.2 shows the basic signal flow in the proposed SHM system. Each blade vibrates with a dominant harmonic related to the rotational frequency of the turbine rotor. This vibrational blade strain energy (top panel in Figure 5.2) is accumulated as a stored electrical charge (second

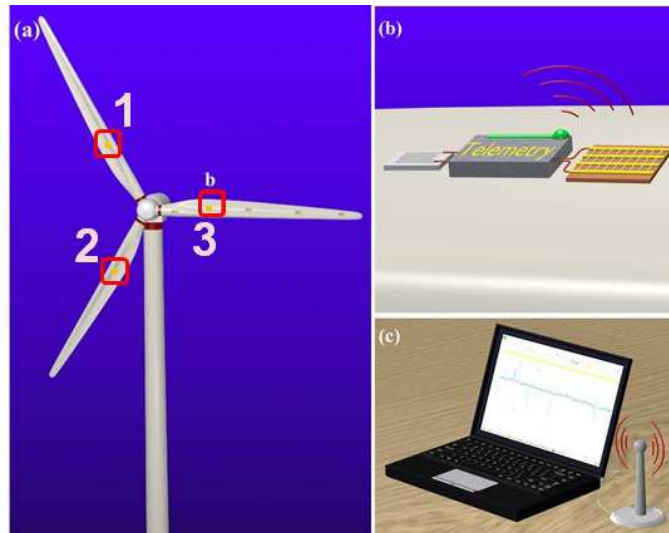


Figure 5.1: Schematic drawing of a vibration-based SHM system: (a) three identical sensor nodes mounted on blades, (b) node with energy harvester and telemetry, and (c) remote-sited data acquisition and health monitoring.

panel in Figure 5.2) by means of an EH. Once sufficient charge has been stored, the RF transmitter sends a binary signal pulse to a centralized monitoring system located in the turbine nacelle (third panel in Figure 5.2). The centralized monitoring system processes the binary pulses from all three blades to determine if a blade has been damaged (bottom of Figure 5.2). The premise of this sensing approach is that the timing of binary pulses from the RF transmitters, which are tied to the EH charging time, is indicative of the local blade structural health. Changes in local stiffness, associated with blade damage, lead to a change in local blade strain [90] and, consequently, a change in the timing of the RF pulses. These pulses are processed to estimate strain energy accumulated at the location of each EH. The health of the blade is determined based on the estimated strain energy. It is important to note that the blade damage will only cause a small change in the strain and hence the signal to noise ratio is small. The proposed methodology is predicated on accumulating energy over long time periods in order to detect the damage (small signal) in the presence of noise (sensor noise and wind variations).

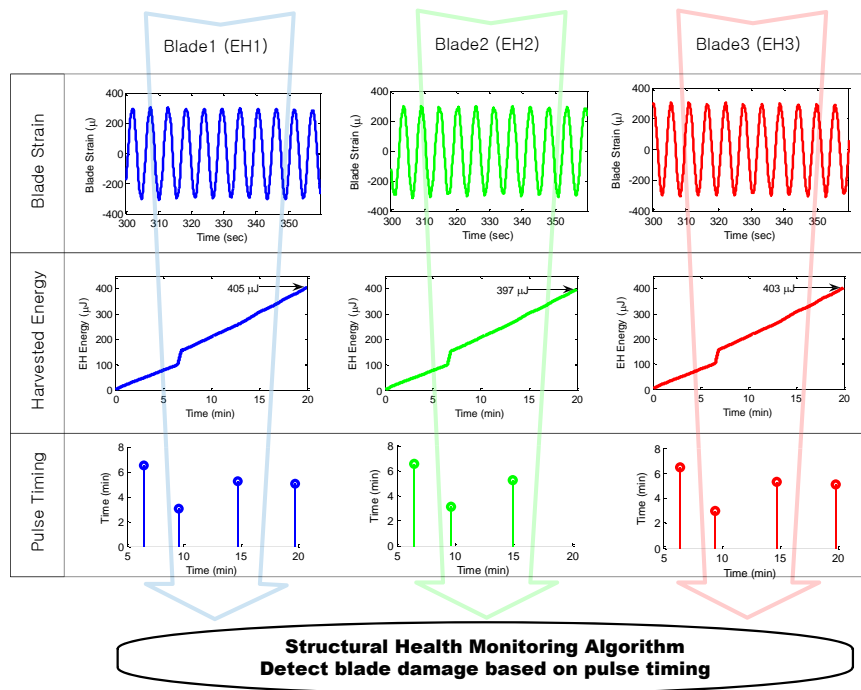


Figure 5.2: Construction of Model-free SHM for Wind Turbine Blades

An EH, when subjected to time-varying strains, converts a fraction of the mechanical strain energy input into usable electrical energy. This paper uses discrete-time steps, Δt , to model the EH behavior. The harvested energy in a single time step B_k is given by

$$B_k = \begin{cases} \eta V E_{EH} \epsilon_k (\epsilon_k - \epsilon_{k-1}) & \text{if } \epsilon_k (\epsilon_k - \epsilon_{k-1}) > 0 \\ 0 & \text{otherwise} \end{cases}, \quad k = 1, 2, 3, \dots \quad (5.1)$$

where V and E_{EH} are the volume (m^3) and Young's Modulus (GPa) of the EH, respectively. [89] The strain of the EH at time step k is ϵ_k . We assume the bond between the EH and the blade is sufficiently strong to treat the EH strain as equal to the blade strain. The EH efficiency η (unitless) is defined as the fraction of mechanical input energy converted into output electrical energy. This efficiency is typically on the order of 10^{-2} . The total harvested energy at time k , W_k , can be expressed in terms of the incremental harvested energy B_k . This relation is given by:

$$W_{k+1} = W_k + (1 + g_D) \cdot B_k. \quad (5.2)$$

Equation (5.2) models the accumulated energy W_{k+1} at time step $k + 1$ as the sum of the energy from the previous step W_k plus the energy harvested between time steps k and $k + 1$. In addition, Eq. (5.2) incorporates a parameter g_D as a simple multiplicative damage model. For example, matrix cracking or delamination/debonding lead to stiffness loss in the material and can be modeled with a multiplying parameter to the stiffness. [82] Hence, increased strain energy due to damage is expected and the degradation parameter $g_D \geq 0$ accounts for this increase in harvested energy. The estimated value g_D for a particular laminate failure model is provided in a later section.

An overview diagram of the proposed SHM system is provided in Figure 5.3. The hardware setup described previously consists of the EH and RF transmitter. This block, labeled "EH", transmits binary pulses once sufficient blade strain energy has been harvested. The remaining blocks constitute the health monitoring algorithm which is performed by a centralized computer in the turbine nacelle. First, a data acquisition system records the pulses with a logged time of receipt. The harvested strain energy at each blade location is estimated based on these pulses using a least squares estimation.

A key difficulty is that the three blades are subjected to unknown inputs such as the wind forces, gravity, tower shadow effects, etc. As a result, the strain energy accumulated at each blade is difficult to model a priori. However, the inherent triple redundancy of the blades can be used to detect damage with a model-free algorithm. Specifically, the strain data obtained from the same locations on each blade can be cross-compared to generate *residual* signals. A residual at time k , r_k , is defined as the difference between the strain energy accumulated on two of the three blades. Three possible residuals can be generated for each span-wise location by comparing all combinations of strain energy estimates from blades 1, 2, and 3. The residuals have the property that they should be small when neither blade is damaged and large when at least one blade is damaged. A simple threshold logic can be used to determine if one or more residuals is sufficiently large to indicate the presence of damage. Details on this algorithm are provided in the next section. The algorithm includes several parameters: probabilistic performance metrics including false-alarm and missed detection rates are used in the next section to specify these algorithm parameters.

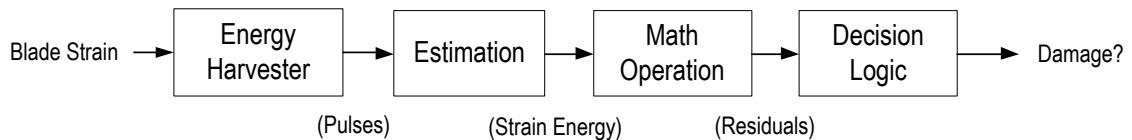


Figure 5.3: An overview of the proposed SHM system: The hardware consists of the EH block (Section 2) and the algorithm consists of the remaining blocks (Section 3).

5.4 SHM Design for Probabilistic Performance

5.4.1 Energy Harvester as a Sensor—Problem Set-up

The energy harvested by each sensor node is a stochastic process and this section describes a simple model that is used in the subsequent sections for probabilistic analysis. Assume the three turbine blades have identical EHs installed at the same spanwise location. Let $W_k^{(i)}$ denote the energy harvested up to time k by a particular sensing node at the same spanwise location on blade i ($i = 1, 2, 3$). Three residuals can be defined by

cross-comparing all possible combinations of the harvested energies:

$$r_k^{(12)} = W_k^{(1)} - W_k^{(2)}, \quad r_k^{(23)} = W_k^{(2)} - W_k^{(3)}, \quad r_k^{(31)} = W_k^{(3)} - W_k^{(1)}. \quad (5.3)$$

As noted above, the basic premise of the SHM algorithm is that a residual with large magnitude is indicative of a damaged blade. One issue is that the centralized SHM algorithm must estimate the harvested energy $W_k^{(i)}$ from the pulses transmitted by each node. The harvested energy at the time of pulse arrival is exactly known because a pulse is transmitted when an EH reaches the (known) signal-transmission energy amount. The transmission times for the three EHs are not synchronous as they accumulate energy at slightly different rates (Figure 5.3). Thus cross-comparison of harvested energy (as in Eq. 5.3) requires estimating the strain energy by linearly interpolating two consecutive pulses. Specifically, assume pulses are received from an EH on blade i at time 0 and N . The harvested energies at times 0 and N are thus known. Moreover, the estimated energy at any time $k \leq N$ is given by $\hat{W}_k^{(i)} = \frac{k}{N} (W_N^{(i)} - W_0^{(i)})$. It is assumed that the error introduced by this linear estimate is negligible. Thus in the remainder of the paper, the hat is dropped and the notation $W_k^{(i)}$ is used for the estimated energy for a blade i .

Eq. (5.2) provided a simple relation for the accumulated energy $W_k^{(i)}$ in terms of the energy harvested at each time step $B_k^{(i)}$. In addition, Eq. (5.1) provided a fundamental relation to describe the per time step harvested energy. The statistical model used in this section takes a less fundamental, data-driven approach to modeling the harvested energy. Specifically, the per time step harvested energy is modeled as ($i = 1, 2, 3$)

$$B_k^{(i)} = \bar{B}^{(i)} + v_k^{(i)} \quad (5.4)$$

where $\bar{B}^{(i)}$ is the mean component averaged over a statistical evaluation time τ_s and $v_k^{(i)}$ is the deviation. The statistical time period $\tau_s (=k_s \cdot \Delta t)$ corresponds to an initial operating period that is used to establish the statistical mean and variance of residuals from healthy wind turbine blades. In other words, $\bar{B}^{(i)}$ is given by

$$\bar{B}^{(i)} = \frac{\text{Number of Pulses} \times \text{Energy/Pulse}}{\text{Statistical Evaluation Time } k_s} \quad \text{for } i = 1, 2, 3. \quad (5.5)$$

The mean component can be different on each blade due to slight differences in the EHs and their installation/orientation. However, the differences in the mean component can be removed by calibration during the initial turbine life, e.g. during the

first month. Thus we assume that the mean values are the same in all three blades, i.e. $\bar{B}^{(1)} = \bar{B}^{(2)} = \bar{B}^{(3)}$. For simplicity the superscript is dropped and \bar{B} denotes this common mean component of the harvested energy. The variational component $v_k^{(i)}$ contains harmonic components due to the rotational frequencies of the blades, e.g. harmonic strain components induced by the gravity on the rotating blades. The variational component also contains a random component due to fluctuations in the wind. The accumulated energy in Eq. (5.2) can be rewritten as

$$W_{k+1}^{(i)} = W_k^{(i)} + \left(1 + g_D^{(i)}\right) \left(\bar{B} + v_k^{(i)}\right) \quad \text{for } i = 1, 2, 3 \quad (5.6)$$

This relation can be substituted into Eq. (5.3) to obtain a stochastic model for the residuals. For example, consider the comparison between blades 1 and 2:

$$r_{k+1}^{(12)} = r_k^{(12)} + \delta_k^{(12)} + \left(g_D^{(1)} - g_D^{(2)}\right) \bar{B} + \left(g_D^{(1)} v_k^{(1)} - g_D^{(2)} v_k^{(2)}\right) \quad (5.7)$$

where $\delta_k^{(12)} := v_k^{(1)} - v_k^{(2)}$ denotes the difference between the two variational terms. The degradation parameters and variational terms are typically small and hence the last term can be neglected. Thus, the residual (approximately) accumulates according to the following relation

$$r_{k+1}^{(12)} = r_k^{(12)} + \delta_k^{(12)} + \left(g_D^{(1)} - g_D^{(2)}\right) \bar{B}. \quad (5.8)$$

The term $\delta_k^{(12)}$ contains harmonic and stochastic components. The relation in Eq. (5.8) effectively integrates (sums) $\delta_k^{(12)}$ over time. The sum of the harmonic components remains bounded in time but the stochastic component has a standard deviation that grows proportionally to the square root of time. Thus, over long time intervals, the stochastic component dominates the harmonic component, and the variational component can be modeled as a white, Gaussian process: $\delta_k^{(12)} \sim N(0, \sigma^2)$ for all k . The use of a Gaussian process can be justified by the central limit theorem. [91] The use of zero mean is justified since \bar{B} contains the mean component of B_k . Note that the variance is denoted with no superscript, i.e. it is assumed that the three residuals have identical variance. In fact, the variance of each residual will be different since, as noted above, the energy harvested by each sensor will be slightly different. However, calibration in the initial life of the turbine can again be used to normalize the statistical properties to

justify this assumption. The residuals (23) and (31) take a similar form as that given in Eq. (5.8).

Figure 5.4 shows a sample case of the three energy residuals. In the figure, the residuals are shown as if blade 3 is damaged and blades 1 and 2 are healthy. As a result, the two residuals $r^{(23)}$ and $r^{(31)}$ tend to drift from their nominal zero mean value. This occurs because $g_D^{(3)}$ is assumed to be larger than $g_D^{(1)}$ and $g_D^{(2)}$. A bias is introduced to the residual process described by Eq. (5.8) that causes these residuals to drift. On the other hand, the remaining residual $r^{(12)}$ remains close to zero mean indicating a healthy status for blades 1 and 2. The basic premise of the SHM algorithm is that residuals exceeding a specified threshold T , e.g. $|r_k^{(23)}| > T$ and $|r_k^{(31)}| > T$, are indicative of a damaged blade. The precise logic is described below. The main design task is to properly select this threshold T based on a fundamental design trade-off between false alarms and missed detections. In addition, the cross-comparison is only performed at specified times separated by k_d time samples. This decision time $\tau_d (= k_d \cdot \Delta t)$ must also be selected to ensure a high probability of damage detection and a low probability of declaring a false alarm.

5.4.2 Threshold Design

The energy accumulated by each of the three blades will be similar but not precisely equal due to environmental and installation variations. As a result the three residuals will not be identically zero in the absence of damage. For example, the model for the residual between blades 1 and 2 (Eq. 5.8) reduces to the following if there is no damage on either blade

$$r_{k+1}^{(12)} = r_k^{(12)} + \delta_k^{(12)} \quad (5.9)$$

where $\delta_k^{(12)} \sim N(0, \sigma^2)$. The monitoring system must be designed to be robust to such variations and not have excessive false alarms.

On the other hand, if there is significant damage in a single blade then the residuals associated with that blade will drift away from zero. For example, if there is damage only in blade 1 ($g_D^{(1)} > 0$ but $g_D^{(2)} = g_D^{(3)} = 0$), then the simple model in Eq. (5.8) indicates that the residual $r_k^{(12)}$ will have a bias that accumulates over time. Similarly the damage in blade 1 will also cause $r_k^{(31)}$ to drift from zero. In this example, the

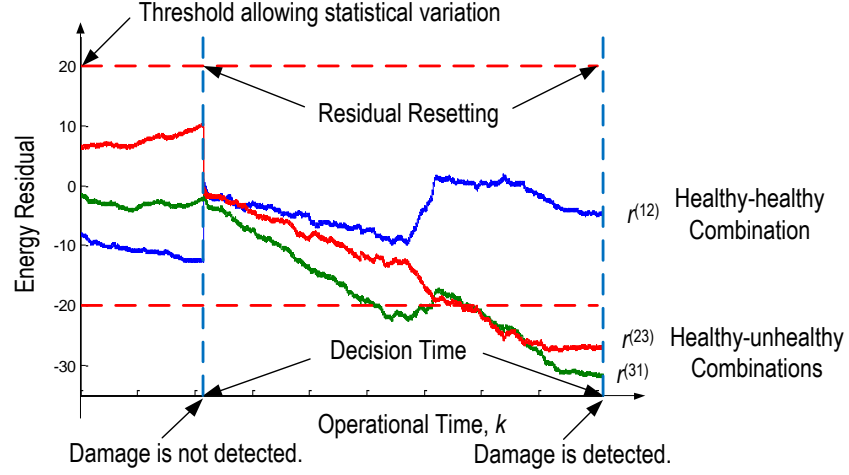


Figure 5.4: A sample case of harvested strain energy residuals is depicted. For each decision time interval, the three residuals are initialized to zero. The residuals $r_k^{(13)}$ and $r_k^{(23)}$ exceed the threshold at the decision time k_d , indicating that blade three is damaged.

residual $r_k^{(23)}$ cross-compares the two healthy blades and this residual will remain small. In general, damage in any single blade will cause the two residuals associated with that single blade to drift.

The monitoring system is designed to check the residuals every τ_d seconds. At this decision time (every k_d steps) the magnitude of the residuals is compared against a threshold T using the following logic based on the discussions above:

$$d := \begin{cases} 0, & \text{if } |r_{k_d}^{(12)}| < T, |r_{k_d}^{(23)}| < T, |r_{k_d}^{(31)}| < T \\ 1, & \text{if } |r_{k_d}^{(12)}| \geq T, |r_{k_d}^{(23)}| < T, |r_{k_d}^{(31)}| \geq T \\ 2, & \text{if } |r_{k_d}^{(12)}| \geq T, |r_{k_d}^{(23)}| \geq T, |r_{k_d}^{(31)}| < T \\ 3, & \text{if } |r_{k_d}^{(12)}| < T, |r_{k_d}^{(23)}| \geq T, |r_{k_d}^{(31)}| \geq T \\ 4, & \text{otherwise.} \end{cases} \quad (5.10)$$

The signal d indicates the status of the blades at the decision time. The decision value $d = 0$ indicates all three blades are healthy and $d = j$ ($j = 1, 2, 3$) indicates damage in blade j . Finally, $d = 4$ indicates the blade health could not be determined from the

residuals. This case could be caused by noisy/corrupted data, possible packet losses, and/or significant damage to more than one blade. Our focus is the incipient damage due to fatigue loading. For this type of damage, the most probable scenario is that only one blade is in failure while the other two blades remain healthy. Thus, it is assumed that the occurrence of $d = 4$ is negligible although further investigation would be required in this case.

The threshold T is designed to ensure a low probability of false alarms. A False Positive (FP) occurs when the SHM algorithm declares a fault ($d = 1, 2$, or 3) but none of the blades is damaged ($g_D^{(i)} = 0$ for $i = 1, 2, 3$). The probability of false positive p_{FP} is thus defined as:

$$p_{FP} = \text{P} \left(d = 1 \text{ or } d = 2 \text{ or } d = 3 \mid g_D^{(i)} = 0 \text{ for } i = 1, 2, 3 \right). \quad (5.11)$$

A simplified form for p_{FP} is derived for use in the threshold selection. First, note that the damage indicators $d = i$ for $i = 1, 2, 3$ are mutually exclusive, i.e. at most one of these cases can occur at the decision time. Thus, the false-alarm probability can be expressed as:

$$p_{FP} = \text{P} \left(d = 1 \mid g_D^{(1)} = 0 \right) + \text{P} \left(d = 2 \mid g_D^{(2)} = 0 \right) + \text{P} \left(d = 3 \mid g_D^{(3)} = 0 \right) \quad (5.12)$$

Next, we note that the three residuals are independent and identically distributed (i.i.d.) in the absence of damage ($g_D^{(i)} = 0$ for $i = 1, 2, 3$). Thus, the three terms in Eq. (5.12) are equal and hence we obtain $p_{FP} = 3\text{P}(d = 1 \mid g_D^{(i)} = 0 \text{ for } i = 1, 2, 3)$. Based on the decision logic defined in Eq. (5.10), this can be explicitly written as:

$$p_{FP} = 3\text{P} \left(|r_{k_d}^{(12)}| \geq T \mid g_D^{(1)} = 0 \right) \cdot \text{P} \left(|r_{k_d}^{(31)}| \geq T \mid g_D^{(1)} = 0 \right) \cdot \text{P} \left(|r_{k_d}^{(23)}| < T \mid g_D^{(1)} = 0 \right) \quad (5.13)$$

As noted above, the residual should be small when there is no damage. Thus, a well-chosen threshold will satisfy

$$\begin{aligned} \text{P} \left(|r_{k_d}| \geq T \mid g_D = 0 \right) &\ll 1, \\ \text{P} \left(|r_{k_d}| < T \mid g_D = 0 \right) &\approx 1. \end{aligned} \quad (5.14)$$

The superscript is dropped in Eq. (5.14) because the relations should hold for any of the three residuals in the condition of no damage in all three blades. Based on this

approximation, the false-alarm probability can finally be expressed as

$$p_{FP} \approx 3\text{P}\left(|r_{k_d}| \geq T \mid g_D = 0\right)^2. \quad (5.15)$$

The approximate relation in Eq. (5.15) is used to appropriately select the decision logic threshold. Let $p_{FP,max}$ denote the maximum allowable probability of false positive probability. The threshold is selected to ensure $p_{FP} \leq p_{FP,max}$. Based on Eq. (5.15), the threshold must be chosen to satisfy

$$\text{P}\left(|r_{k_d}| \geq T \mid g_D = 0\right) \leq \sqrt{\frac{1}{3}p_{FP,max}}. \quad (5.16)$$

Next note that in the absence of a fault the residuals are governed by a stochastic process as given in Eq. (5.9) where $\delta_k^{(12)}$ is an i.i.d. Gaussian process with $\delta_k^{(12)} \sim N(0, \sigma^2)$ at each k . In the absence of damage the residual at the decision time satisfies $r_{k_d} = \sum_{k=1}^{k_d} \delta_k$. Thus, the residual is zero mean and satisfies $r_{k_d} \sim N(0, k_d\sigma^2)$ at the decision time. Eq. (5.16) can be expressed as with an explicit integral based on the fact that r_τ is a Gaussian random variable:

$$1 - \int_{-T}^T \frac{1}{\sqrt{k_d}\sigma\sqrt{2\pi}} \exp^{-\frac{x^2}{2k_d\sigma^2}} dx \leq \sqrt{\frac{1}{3}p_{FP,max}}. \quad (5.17)$$

The smallest threshold satisfying this constraint is chosen such that Eq. (5.17) holds with equality. With a chosen $p_{FP,max}$, T is solved for in Eq. (5.17). The decision time k_d —to be determined simultaneously along with this step—is the only free variable in the equation, and so a series of T is obtained corresponding to a range of k_d . A lower $p_{FP,max}$ or larger σ requires higher T . Larger values of the threshold consequently make it more difficult to detect damage. Thus the selection of the threshold T involves a basic design trade-off between false positives and damage detection.

5.4.3 Probabilistic Analysis at the Decision Time, τ_d

The blade residuals are checked periodically every k_d time steps (τ_d seconds). This section describes the method used to choose this decision time τ_d . Larger values of τ_d increase the probability of detection. Specifically, the blade structural damage does not improve over time or most likely degrades further. We assume the decision time period is short relative to the damage progression time. This assumption, valid in the initial

phase of damage when it is small in size and growing slowly, implies that the degradation parameter g_D in Eq. (5.8) can be treated as a constant bias. As a consequence, a longer decision time τ_d gives more time for this bias to cause the residuals to drift away from zero hence increasing the likelihood of detection. A True Positive (TP) occurs when the SHM declares a fault (e.g. $d = 1, 2$ or 3) and the corresponding blade is damaged (e.g. $g_D^{(1)} = g_D$ and $g_D^{(2,3)} \approx 0$ for $d = 1$). The drawback of a large value of τ_d is that it delays the detection of damage in the blade. The objective of the design is to choose the smallest possible value of τ_d (to ensure fast detection) while still ensuring that τ_d is large enough to yield a high probability of true positive.

For concreteness, consider the case where blade 1 is damaged while blades 2 and 3 are healthy. The cases where only blades 2 or 3 are damaged can be treated similarly to the analysis that follows. Assume the degradation parameter on blade 1 is a constant g_D . The Damage Model section will discuss how the smallest detectable damage g_D should be chosen to prevent more severe blade damage. With $g_D^{(1)} = g_D$ and $g_D^{(2,3)} = 0$, Eq. (5.8) becomes

$$\begin{aligned} r_{k+1}^{(12)} &= r_k^{(12)} + g_D \cdot \bar{B} + \delta_k \\ r_{k+1}^{(23)} &= r_k^{(23)} + \delta_k \\ r_{k+1}^{(31)} &= r_k^{(31)} - g_D \cdot \bar{B} + \delta_k \\ \delta_k &\sim N(0, \sigma^2). \end{aligned} \quad (5.18)$$

The probability of true positive p_{TP} for ($d = 1$) is defined as:

$$p_{TP}(d = 1) = \text{P} \left(d = 1 \mid g_D^{(1)} = g_D, g_D^{(2,3)} = 0 \right). \quad (5.19)$$

The true positive probability can be rewritten in terms of the residuals. To shorten the notation, let $g_D^{(1,2,3)} = (g_D, 0, 0)$ denote the blade damage state. Then the true positive probability is expressed as:

$$p_{TP}(d = 1) = \text{P} \left(\{|r_{k_d}^{(12)}| \geq T, |r_{k_d}^{(23)}| < T, |r_{k_d}^{(31)}| \geq T\} \mid g_D^{(1,2,3)} = (g_D, 0, 0) \right). \quad (5.20)$$

As in the Threshold Design section, a simplified form for p_{TP} is derived for the decision time selection. First, note that $r^{(23)}$ in Eq. (5.18) is independent of $r^{(12)}$ and $r^{(31)}$. Thus, based on the decision logic defined in Eq. (5.10), the detection probability can be

expressed as:

$$p_{TP}(d=1) = \mathbb{P} \left(\{|r_{k_d}^{(12)}| \geq T, |r_{k_d}^{(31)}| \geq T\} \mid g_D^{(1,2,3)} = (g_D, 0, 0) \right) \cdot \mathbb{P} \left(|r_{k_d}^{(23)}| < T \mid g_D^{(1,2,3)} = (g_D, 0, 0) \right). \quad (5.21)$$

To further simplify this relation, the conditional probability formula is applied for two correlated events A and B occurring together and conditioned on event C : $\mathbb{P}(A, B \mid C) = \mathbb{P}(A \mid B, C)\mathbb{P}(B \mid C)$. Applying this fact to Eq. (5.21) yields:

$$\begin{aligned} & \mathbb{P} \left(\{|r_{k_d}^{(12)}| \geq T, |r_{k_d}^{(31)}| \geq T\} \mid g_D^{(1,2,3)} = (g_D, 0, 0) \right) \\ &= \mathbb{P} \left(\{|r_{k_d}^{(12)}| \geq T\} \mid \{|r_{k_d}^{(31)}| \geq T, g_D^{(1,2,3)} = (g_D, 0, 0)\} \right) \cdot \mathbb{P} \left(|r_{k_d}^{(31)}| \geq T \mid g_D^{(1,2,3)} = (g_D, 0, 0) \right). \end{aligned} \quad (5.22)$$

From the discussion in the Threshold Design section, a well-chosen threshold should cause a small residual for no damage but a large one for damage. Thus,

$$\begin{aligned} & \mathbb{P} \left(\{|r_{k_d}^{(12)}| \geq T\} \mid \{|r_{k_d}^{(31)}| \geq T, g_D^{(1,2,3)} = (g_D, 0, 0)\} \right) \\ & \approx \mathbb{P} \left(\{|r_{k_d}^{(31)}| \geq T\} \mid \{|r_{k_d}^{(12)}| \geq T, g_D^{(1,2,3)} = (g_D, 0, 0)\} \right) \approx 1 \end{aligned} \quad (5.23)$$

From Eqs. (5.14) and (5.18), $r_k^{(23)}$ should be small by considering the independence of g_D . Hence,

$$\mathbb{P} \left(|r_{k_d}^{(23)}| < T \mid g_D^{(1,2,3)} = (g_D, 0, 0) \right) = \mathbb{P} \left(|r_{k_d}^{(23)}| < T \mid g_D^{(1,2,3)} = (0, 0, 0) \right) \approx 1 \quad (5.24)$$

Finally, substitute the results of Eqs.(5.22 and 5.24) into Eq. (5.21) to yield the following approximation for the probability of TP:

$$\begin{aligned} p_{TP}(d=1) & \approx \mathbb{P} \left(|r_{k_d}^{(31)}| \geq T \mid g_D^{(1,2,3)} = (g_D, 0, 0) \right) \\ & \text{or} \approx \mathbb{P} \left(|r_{k_d}^{(12)}| \geq T \mid g_D^{(1,2,3)} = (g_D, 0, 0) \right) \end{aligned} \quad (5.25)$$

Eq. (5.25) is used to appropriately select the decision time. Let $p_{TP,min}$ denote the minimum allowable probability of true positive probability. The decision time is selected to ensure $p_{TP} \geq p_{TP,min}$:

$$\mathbb{P} \left(|r_{k_d}^{(ij)}| \geq T \mid |g_D^{(i)} - g_D^{(j)}| = g_D \right) \geq p_{TP,min}, \quad \text{for } i, j = 1, 2, 3 \text{ and } i \neq j. \quad (5.26)$$

In this damage case, Eq. (5.26), the residuals are also governed by a stochastic process with a mean component due to g_D , i.e, Gaussian process with $N(g_D \cdot \bar{B}, \sigma^2)$ at each k time step. Thus, the residual satisfies $r_{k_d} \sim N(k_d \cdot g_D \cdot \bar{B}, k_d \cdot \sigma^2)$ at k_d time step. Eq. (5.26) can be expressed as an explicit integral because r_{k_d} is a Gaussian random variable:

$$1 - \int_{-T}^T \frac{1}{\sqrt{k_d} \sigma \sqrt{2\pi}} \exp^{-\frac{(x - g_D \cdot k_d \cdot \bar{B})^2}{2k_d \sigma^2}} dx \geq p_{TP, min}. \quad (5.27)$$

A similar form of Eq. (5.27) is derived for $p_{TP}(d = 2 \text{ or } 3)$ given the assumption that damage to more than one blade occurs rarely often. As noted earlier, the bias term $g_D \cdot \bar{B}$ appears in (5.8) due to the damage. Larger values of g_D make the residual r_k drift faster from zero and hence a damage decision can be made more quickly with the same level of $p_{TP, min}$.

5.5 Case Study: Application of SHM

In this section the applicability of the proposed SHM algorithm is explored for full scale wind turbines. We establish harvested strain energy, residuals and statistical characteristics for a single sensor location on all three blades that is not at the damage site. The sensor configuration is selected such that the (harvester) step time Δt and transmitter pulse interval are much smaller than the statistical evaluation time τ_s and the decision time τ_d . Given these conditions, Eqs. (5.17 and 5.27) are utilized to determine a threshold and a decision time that are adequate to identify blade damage within user specified probabilities ($p_{FP, max}$ and $p_{TP, min}$). Estimates of the blade degradation parameter g_D and strain energy characteristics \bar{B} and σ are developed in the following sections. Results are presented for a range of model parameters including the probability of false positive p_{FP} , the probability of true positive p_{TP} , and the decision time τ_d .

5.5.1 Damage Model: Estimate Degradation Parameter g_D

To estimate the degradation parameter g_D , we consider damage associated with matrix cracking at a discrete location in the blade. As the blade undergoes cyclic loading, the crack density increases and the stiffness of the damaged region (referred to as the local stiffness) E' decreases relative to the original stiffness E . [90] A dynamic finite element

analysis is performed to compare the effect of the local reduction in stiffness $\frac{E'}{E}$ on the surface strain (and hence strain energy) along the length of a wind turbine blade. Similarly, ϵ' is defined as the damaged beam strain while ϵ is the intact beam strain. Because the EH and wireless transmitter assembly may not be located exactly at the damage location, the estimate of g_D is based on strain energy far from the damage site.

One challenge in creating the finite element model is that the exact geometry and layup of full scale wind turbine blades are proprietary data. There are, however, open access input data files for several FAST wind turbine models. [3] While these data files do not include layup or material properties, overall geometry and cross sectional stiffness along the length of the blade are provided. In the present study, the blade geometry and cross sectional properties were selected to be comparable with FAST model input for a 5MW wind turbine. [92] The blade is modeled as a 61.5 m long (x axis) thin walled tapered beam with an elliptical cross section fabricated from glass epoxy composite. The elliptical cross section dimensions and layup were selected such that the stiffness about the major axis (y) of the hollow elliptical beam at the root and tip is approximately the same as the flapwise stiffness at the root and tip of the 5 MW wind turbine blades. At the root of the beam the cross section has a major axis length of 3 m and minor axis length of 2.25 m. At the tip the major axis is 0.62 m and the minor axis is 0.46 m. The thin-walled outer skin is 20 mm with a quasi-isotropic layup such that, for a shell element with local in plane axes 1 and 2, $E_1 = E_2 = 20.45$ GPa. Given the beam geometry and material properties, the cross section bending stiffness about the major axis (EI_{yy}) is $229e7$ Nm² at the root and $2e7$ Nm² at the tip. The finite element model of the beam consists of composite elements, with 24 elements around the circumference of the beam and 246 elements along the length of the beam. The beam element includes in plane and out of plane displacements, rotation and warping. Orthotropic material properties may be specified.

The damaged blade was modeled by reducing the stiffness of several shell elements located at 20.5 m from the root on the top surface (Figure 5.5). To quantify the stiffness loss that can occur as a result of matrix cracking, test data for wind turbine blades [90] and models of thin walled helicopter rotor blades [93] were considered. These studies indicate that the local reduction in stiffness associated with matrix cracking ranges from 13 to 40%. In estimating g_D , the size of the damaged region is varied as well as

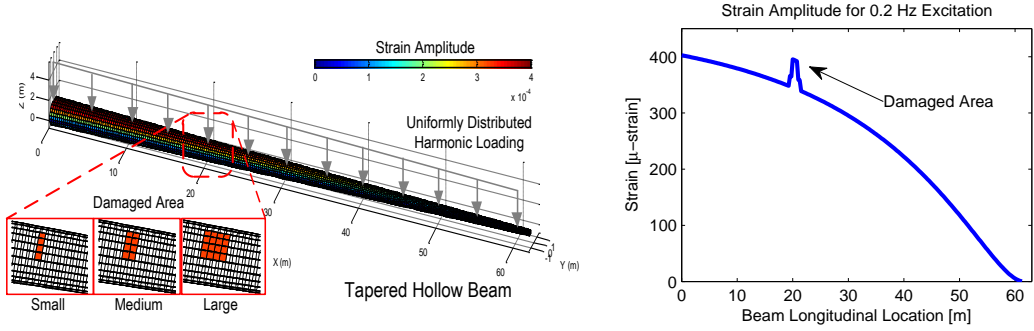


Figure 5.5: Strain Amplitude of an Intact Thin-Walled Finite Element Beam and Degradation Area: The beam is 61.5 m long and three sizes of degradation are considered at 20.5 m location as shown in the insets.

the extent of damage. For the most severe case of damage imposed in the beam finite element model, the damaged area is approximately 1 m wide by 1.1 m long and with $E' = 0.6E$. For the least damaged case, the damaged area is 0.25 m wide and 1.1 m long with $E' = 0.8E$. Both laminate directions 1 and 2 are degraded because the laminate is quasi-isotropic. In all, six combinations of size and extent of damage were evaluated.

The hollow beam was subjected to a 0.2 Hz uniformly distributed sinusoidal load in the xz plane. The load frequency corresponds to the FAST 5 MW wind turbine rotational speed in region 3. The load magnitude is such that strain amplitude ϵ_{zz} at the root of the beam is approximately 400 μ -strain—a strain level comparable to strain that occurs for full scale wind turbines under operational conditions. [81] The model output includes stresses, strains, rotation and displacement at all element nodes. Figure 5.5 shows the strain amplitude of a damaged beam along the length of the beam for the case where the damage area is 1 m \times 1.1 m and the extent of damage ratio $\frac{E'}{E}$ is 0.6. For this case the surface strain ratio $\frac{\epsilon'}{\epsilon}$ along the top surface reaches a value of 1.15 at the damage location and approaches 1.0018 away from the damage location. This asymptotic strain level is referred to as the far field strain. The g_D is obtained by comparing ϵ' to ϵ :

$$g_D = \left(\frac{\epsilon'}{\epsilon} \right)^2 - 1. \quad (5.28)$$

The degradation parameters for the far-field strain change between intact beams and

Table 5.1: Degradation Parameter g_D

	$E' = 0.8E$	$E' = 0.6E$
Small Size (0.25 m \times 1 m)	0.0005	0.0011
Medium Size (0.5 m \times 1 m)	0.0008	0.0018
Large Size (1 m \times 1 m)	0.0017	0.0035

damaged beams are reported in Table 5.1. The parameter ranges from 0.0005 to 0.0035 for the cases considered.

5.5.2 Characterization of the strain data: \bar{B} and σ

The algorithm requires strain energy characteristics for a healthy blade: the average of harvested energy per time step \bar{B} (Eq. 5.5) and the noise in the strain pulse data σ (Eq. 5.9). To quantify these characteristics for a full scale wind turbine, we evaluated strain data from a 2.5 MW C96 Clipper Liberty Wind Turbine [86] that is operated by the Eolos Wind Research Consortium [56] at the University of Minnesota. The 2.5 MW clipper wind turbine is relatively new and the assumption is that the strain data are representative of healthy turbine blades. The turbine has a rotor diameter of 96 m and tower hub height of 80 m. The three blades are instrumented with ten fiber optic strain gages installed at various points of each blade for research purposes. They are located at the leading edge, trailing edge, high, and low pressure sides of the blade root; and high and low pressure sides of 25%, 37.5%, and 45% blade span length. For each sensor, strain is continuously recorded at a frequency of 20 Hz. The strain data include several sensing errors such as bias, bias drift, scale error, high frequency chatter and signal drop-outs. Therefore, a data cleansing step is required to remove these errors.

Once the strain data are conditioned, then the accumulated energy $W_k^{(i)}$ and incremental change in energy $B_k^{(i)}$ are evaluated for a common sensor location across the three blades. The harvested energy (and hence $W_k^{(i)}$ and $B_k^{(i)}$) depends on the EH characteristics (Eq. 5.1). In the case study, we consider an MFC EH with efficiency $\eta = 0.4\%$, [89] surface area 28 mm by 15 mm by 0.3 mm thick, and stiffness $E = 30$ GPa. The statistical characteristics of the harvested energy \bar{B} and σ are obtained over the evaluation time τ_s , such that τ_s is of the same order of magnitude as the decision time

and much greater than the pulse interval. In the present study, $\tau_s = 1$ month and the values of \bar{B} and σ are calculated for each month of Eolos wind turbine data from May through November 2013. The accumulated energy for each blade $W_k^{(i)}$ is scaled such that the three energy increment averages are approximately equal, i.e. $\bar{B}^{(1)} \approx \bar{B}^{(2)} \approx \bar{B}^{(3)}$. This step compensates for the slight differences in the harvested strain energy between the three blades. For the Eolos wind turbine, \bar{B} ranges from 0.008 $\mu\text{J}/\text{step}$ in June to 0.0121 $\mu\text{J}/\text{step}$ in September 2013.

The noise depends on the variability in the residual at each time step r_k based on the variance in the data over the statistical evaluation time τ_s . The τ_s is divided into m time windows. The residual for the i th window $r_{k,i}$ (where $i = 1, 2, 3, \dots, m$) is a discrete data set. Each data set is shifted by a constant such that the initial residual value is 0. The variance across all of the residual data sets at the k th time step is

$$\rho_k^2 = \frac{\sum_{i=1}^m r_{k,i}^2}{m}, \quad k = 1, 2, 3, \dots, k_f. \quad (5.29)$$

Because r_k is assumed to be a random variable, $r_{k_f} \sim N(0, \rho_{k_f})$, σ satisfies the relation,

$$\sigma^2 = \frac{\rho_{k_f}^2}{k_f}. \quad (5.30)$$

The validity of this approach is demonstrated in Figure 5.6. EOLOS strain data for the month of August 2013 are divided into 10 windows ($m = 10$) with the initial strain energy for each window set to zero (Figure 5.6 a). The individual variances for each time step k (i.e. ρ_k , Eq. 5.29) are calculated and compared to the stochastic model (Eq. 5.9). In Figure 5.6 (b), the solid smooth curve is drawn from the standard deviation of r_k , $\sqrt{k}\sigma$, where σ is calculated from Eq. (5.30). There is a good agreement between the stochastic model and the data (Figure 5.6 b). Following this approach, the noise in the Eolos strain data σ ranges from 0.102 μJ in August to 0.392 μJ in November 2013 (see appendix C). The monthly σ data are compared to the real power output and wind speed at the same month in Figure 5.7. As shown, the trend of σ is reflected by the wind turbine operation and wind speed. This observation confirms the legitimacy of the earlier assumption—the energy difference between blades is mainly due to the stochastic nature of the wind.

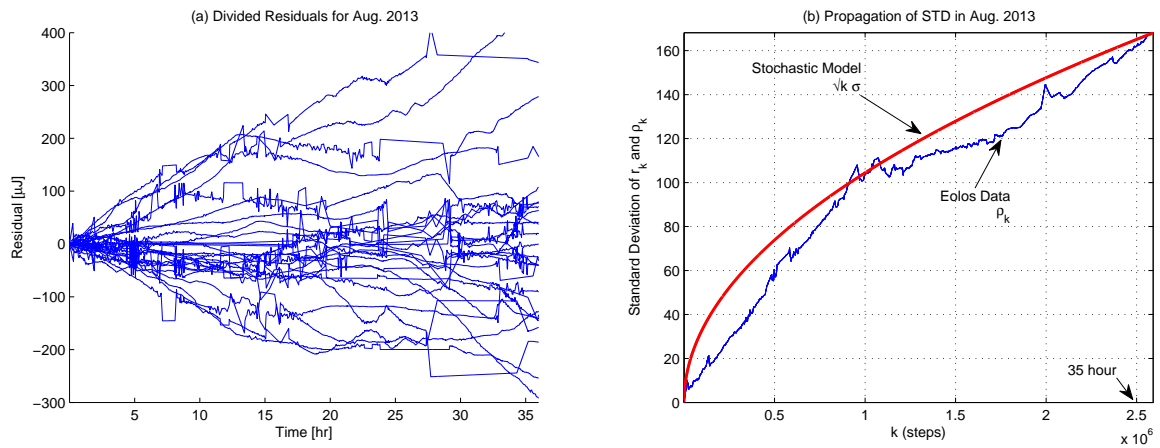


Figure 5.6: (a) Division of residuals in August 2013 for three blades into ten windows superimposed, (b) Propagation of the standard deviation of the residuals for August 2013

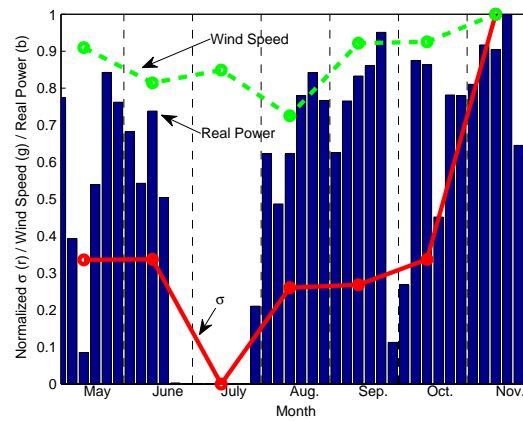


Figure 5.7: Normalized real power output of the Eolos turbine compared to the normalized σ : The residual variance follows the trend of the turbine power output.

5.5.3 Results

The SHM algorithm provides a statistical approach to detect damage based on the variation in the energy harvested over the decision time. In earlier sections, numerical values for g_D ($0.0005 \sim 0.0035$), \bar{B} ($0.0104 \mu\text{J}/\text{step}$) and σ ($0.102 \mu\text{J}$) were obtained

for full scale wind turbine blades operated in August 2013. Given these system characteristics, the monitoring performance (p_{TP} and p_{FP}) as a function of decision time was determined by simultaneous solution of Eqs. (5.17 and 5.27). The trade-off relationship between damage level and decision time is investigated.

In evaluating the performance, target limits for $p_{FP,max}$ and $p_{TP,min}$ are established as follows. To limit $p_{FP,max}$ to one false positive over the turbine service life τ_L for a decision time (in units of seconds) τ_d , then

$$p_{FP,max} = \frac{\tau_d}{\tau_L}. \quad (5.31)$$

In the study, decision times ranging from 13 to 50 days are considered and the turbine service life is 20 years. Thus, $p_{FP,max}$ ranges from 0.18% to 0.68%. The $p_{TP,min}$ is set to 90%. This limit results in a nearly 100% detection rate, the total probability of a true positive $p_{TP,total}$, after several consecutive inspections. The total probability after n consecutive decision cycles is the sum of a geometric series with a common ratio of $1 - p_{TP,min}$:

$$p_{TP,total} = p_{TP,min} \cdot \frac{1 - (1 - p_{TP,min})^n}{p_{TP,min}}. \quad (5.32)$$

For example, if $n = 8$, the $p_{TP,total}$ is approximately 1. For comparison, consider that commercial flight control electronics are required to have no more than 10^{-9} catastrophic failures per flight hour. [85, 94].

One approach to evaluate the sensitivity of the SHM algorithm is to plot the Receiver Operating Characteristic (ROC) curves, p_{TP} as a function of p_{FP} , for constant decision times. These ROC curves at each decision time are constructed by varying the threshold T from 0 to ∞ (see Eqs. 5.17 and 5.27). Figures 5.8 and 5.9 show ROC curves for two cases of blade damage, $g_D = 0.0008$ and $g_D = 0.0035$, for decision times ranging from 13 to 200 days. The ideal position in the ROC space is in the upper left corner of the plot, when p_{TP} is the highest and p_{FP} is the least. This optimal configuration is approached as the decision time increases. For $g_D=0.0008$, a decision time much greater than 200 days is required to achieve a 90% p_{TP} with p_{FP} less than 1%. For a higher level of damage, such as $g_D=0.0035$, the target performance of 90% p_{TP} with $p_{FP} < 1\%$ is achieved with a decision time of 50 days. The effect of threshold level is also apparent. While it is feasible to achieve a high p_{TP} as T approaches 0 (along an ROC curve), p_{FP} also increases: both p_{TP} and p_{FP} are likely when the T is small. The combination of

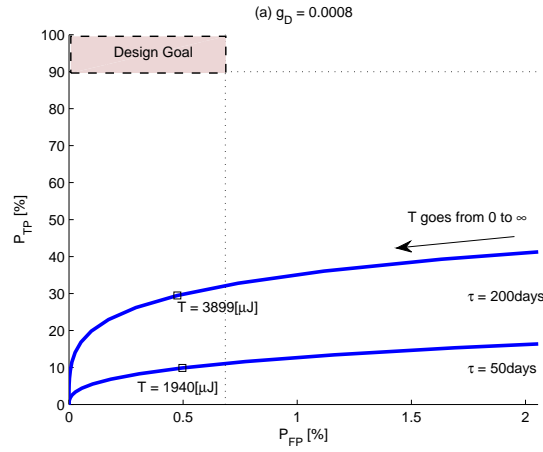


Figure 5.8: Receiver Operating Characteristic Curves for damage $g_D = 0.0005$. To meet the performance targets of 90% p_{TP} with $p_{FP} < 1\%$, the decision time increases significantly when the degradation parameter is small.

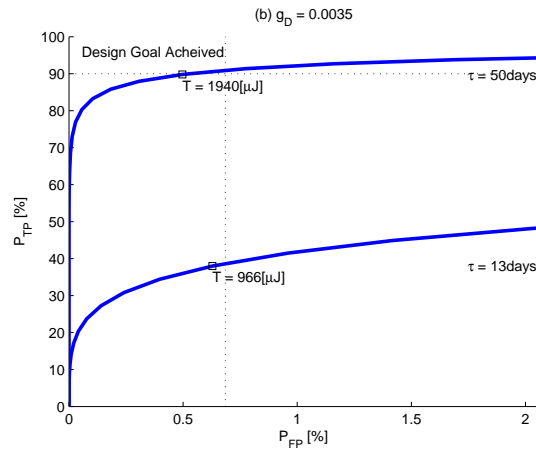


Figure 5.9: Receiver Operating Characteristic Curves for damage $g_D = 0.0035$.

both a high threshold and long decision time leads to an optimal combination of p_{TP} and p_{FP} .

The challenge in detecting damage when τ_d is short is illustrated in Figures 5.10 and 5.11. Both figures show the decision time as a function of the degradation parameter for $p_{TP,min} \geq 50\%$ when $p_{FP,max} = 0.7\%$. Figure 5.10 is for the baseline case where

$\bar{B} = 0.0104$, and Figure 5.11 is for the case where $\bar{B} = 0.0416$ (a factor of 4 increase). For either scenario, the decision time increases significantly when either the target p_{TP} increases or the degradation parameter decreases. Consider the lower energy case Figure 5.10. When $g_D = 0.0035$, the decision time to achieve 90% p_{TP} is 50 days. If a higher p_{TP} is desired, the decision times to achieve 99% and 99.9% p_{TP} are 90 and 180 days respectively. Decreases in the level of damage have a similar effect. If the damage decreases by a factor of 2, such that $g_D = 0.0017$, then the decision time required to achieve a 90% p_{TP} is 200 days. For a utility-scale wind turbine, a time period of 200 days is approximately 3 % of the 20-year life. This ratio can be compared to the fatigue testing result of 9 meter carbon fiber blades by Paquette et. al [90]. They simulated the 20-year turbine life in a 2×10^6 cycle test. The number of cycles from crack initiation to noticeable surface cracks was 0.25×10^6 , which is approximately 12.5% of the 20-year lifetime. If the SHM must detect damage on the order of 0.0017 within 25 days, then p_{TP} is less than 50%, a performance level that may be unacceptable. In sum, a high detection probability or a small level of damage requires more time for the damage bias to accumulate and cause a detectable drift in the residual.

A proportional reduction in decision time can be achieved by increasing the quantity of energy harvested \bar{B} . For example, the potential effect of increasing the energy harvested by a factor of 4 with $\bar{B} = 0.04$ (while σ is increased to 0.204) can reduce the decision time. In this case, noise which comes from the EH could become less effective relatively due to increased harvested energy. As expected, the decision time to detect damage with $g_d = 0.0017$ with a p_{TP} of 90% is reduced from 200 days to 50 days. Higher levels of harvested energy can be achieved by increasing the energy harvester surface area and/or improving the energy harvester efficiency.

5.6 Summary and Conclusions

This paper investigated an SHM algorithm to detect damage in wind turbine blades. The algorithm utilizes model-free monitoring, which does not require information about blade geometry, blade material type or accurate external force. The system relies on the accumulated strain-energy difference between EH sensors installed on the same locations of three blades. The sensors harvest low frequency (< 0.2 Hz) vibrational energy from

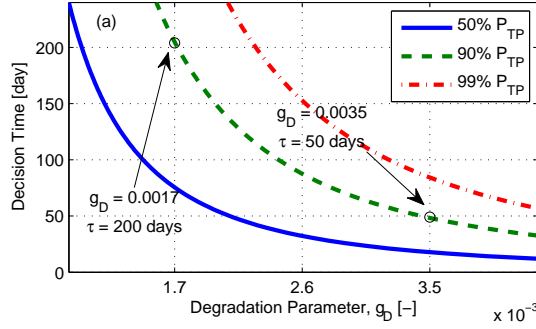


Figure 5.10: Decision time versus degradation parameter with $p_{FP} = 0.7\%$ for the baseline $\bar{B} = 0.0104 \mu\text{J}/\text{step}$ and $\sigma = 0.102 \mu\text{J}$

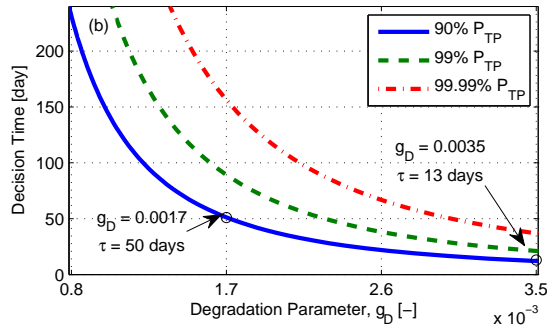


Figure 5.11: Decision time versus degradation parameter with $p_{FP} = 0.7\%$ for the enhanced EH by increasing surface area, $\bar{B} = 0.0416 \mu\text{J}/\text{step}$ and $\sigma = 0.204 \mu\text{J}$

the blades and wirelessly transmit a pulse once sufficient energy has been stored. The premise of this sensing approach is that the timing of signal transmissions is indicative of the structural health of the blade. Signal transmission timings of a damaged blade differ from the timings of undamaged blades so that damage can be detected.

The SHM was developed specifically for a self-powered wireless system. The sensors consist of a Piezo-electric EH, and RF transmitter. Because blade damage causes local stiffness loss that leads to a change in blade strain, strain-energy quantities are compared between blades based on received pulses. To compare strain energies, a residual was defined as the difference between two blades. A residual remains small (but not zero due to noise σ) when neither blade is damaged but becomes large when one blade is

damaged.

The key feature of the algorithm is to discern damage from noise. Noise creates false alarms even when there is no damaged blade. A stochastic model for the residual incorporated the noise—using an i.i.d. Gaussian random variable—and enabled a theoretical SHM design methodology. A satisfactory SHM design was obtained for good detection performance: a low false alarm rate (Probability of the False Positive p_{FP}) and high detection rate (Probability of the True Positive p_{TP}). Damage detection depends on the strain energy available \bar{B} and the level of degradation g_D . If either \bar{B} or g_D (or both) is large, the damage can be more quickly detected.

To design an SHM system, estimation of g_D for targeted damage types and statistics (\bar{B} and σ) were obtained. Appropriate damage scenarios—0.25, 0.5 and 1 m \times 1.1 m damage size with 20% and 40% degradation—were applied to a thin-walled tapered hollow beam. Global degradation was found from 0.0005 to 0.0035. And \bar{B} and σ were obtained from a full scale wind turbine, called Eolos, during the period from May to November 2013. The calculated σ followed well the trend of wind speed and turbine power output. And propagation of standard deviation from Eolos data was well matched with the proposed stochastic model. Using August 2013 data, large damage of $g_D = 0.0035$ could be detected after 50 days with $p_{FP} = 0.7\%$ and $p_{TP} = 90\%$ by a stamp-sized EH. As noted, the decision time can be reduced with the increased harvested energy. When the size of the EH was scaled up by four times, then the decision time could be decreased to 13 days for the same size of damage with the same level of probabilities. Half the size of the damage, $g_D = 0.0017$, could be detected after 50 days by the scaled-up EH. Thorough research regarding the EH design and EH's effects on the statistics of a residual is left for future work.

Nomenclature

\bar{B}	=	Average of strain energy one-step increment, [$\mu\text{J}/\text{step}$]
B_k	=	Strain energy one-step increment, [$\mu\text{J}/\text{step}$]
E	=	Young's Modulus of a composite blade, [GPa]
E'	=	Degraded Young's Modulus, [GPa]
E_{EH}	=	Young's Modulus of an EH, [GPa]

g_D	=	Degradation parameter, [-]
k_d	=	Decision Time, [step]
k_f	=	Last time step of the given time frame, [step]
k_s	=	Statistical Evaluation Time, [step]
m	=	Number of divided windows from the evaluation time, [-]
p_{FP}	=	Possibility of False Positive, [%]
p_{TP}	=	Possibility of True Positive, [%]
$r_k^{(ij)}$	=	Residual of i, j blades at time k , [μJ]
T	=	Threshold, [μJ]
V	=	Volume of an EH, [m^3]
v_k	=	Variational term in B_k , [μJ]
$W_k^{(i)}$	=	Strain energy of the EH in the blade i , [-]
n	=	Integer, [-]
Δt	=	Step time, [sec/step]
δ_k	=	Random Variable in the residual, [μJ]
ϵ	=	Strain of a composite blade, [μ -strain]
ϵ'	=	Strain of a damaged composite blade, [μ -strain]
σ^2	=	Variance of δ_k , [μJ^2]
ρ_k^2	=	Variance of r_k , [μJ^2]
η	=	EH Efficiency, [-]
τ_d	=	Decision time, [sec]
τ_L	=	Wind turbine's life time, [sec]
τ_s	=	Statistical evaluation time, [sec]

Chapter 6

Conclusions & Future Work

This dissertation presents a novel wireless structural health monitoring (SHM) methodology for wind turbine blades. A wireless sensor node, comprised of an energy harvester (EH) and telemetry module, can be attached to the surface of the blades. The proposed system employs an off-the-shelf EH, telemetry, and signal conditioning unit. Once an EH captures sufficient electricity, the transmitter generates a pulse. The SHM algorithm was specifically designed to utilize the pulse intervals and to compare a set of intervals from three blades. The focus of this thesis was to demonstrate the feasibility of this SHM approach. In particular, feasibility requires: 1) an estimation of the strain energy available from a healthy rotor blade; 2) evaluation of EH efficiency to convert strain energy at low frequency of blade loading; 3) design of the detection algorithm; and 4) demonstration of the capability of the algorithm.

It is important to evaluate strain energy, because blade damage is associated with stiffness loss, which changes the strain energy. The strain energy was quantified for typical sizes of full-scale wind turbines over three levels of turbulence intensity. The FAST (Fatigue, Aerodynamics, Structures, and Turbulence) simulator was used to determine blade bending moments by which strains were calculated. Based on the simulation, the maximum strain occurs at about half the first modal frequency of the blades in a distance of approximately one third of the blade length from the hub. For the three turbine models, the maximum strain amplitude is ~ 550 μ -strain at 0.2 Hz for the 5 MW offshore turbine. For the 5 MW model at the rated wind speed (11.4 m/s), ~ 400 μ -strain can be expected.

An EH converts the strain energy into usable electricity. The converted electric energy could be estimated by available strain energy multiplied by a conversion efficiency, which depends on an input frequency. This efficiency was studied analytically and experimentally. In the experiments, a 20 cm long aluminium beam with a triangle area from the middle to the root was designed so that a uniform strain field could be secured. For a commercial EH (MFC M2814 P2 type from Smart Material), approximately a 0.48% efficiency was obtained at the typical wind turbine's rotational speed of 0.2 Hz. The study provided a methodology to calculate the charging time for any type of piezoelectric EHs working for wind turbine blades. For example, the working condition of ~ 400 μ -strain at 0.2 Hz with the 0.48% efficiency requires ~ 8 minutes for a transmitter to send one strain measurement (which requires ~ 280 μ J).

Intermittent sampling of measurements—due to low power availability—is challenging for signal analysis. To overcome this challenge, the SHM algorithm was based on the performance evaluation of pulse timings of the three EHs—installed at the same locations on the three blades (i.e. the hardware redundancy). When three EHs are compared, a strain measurement is not necessary. As a result, the energy requirement could be reduced from ~ 280 to ~ 100 μ J for one signal transmission. Thus, the timing of signal transmissions was used as an indicator of the structural health.

To process pulse data, two metrics were suggested: the ratios of signal timings (i.e. transmission ratio) and the difference between signal timings (i.e. residuals). For either method, damage is indicated when the energy ratio or residual exceeds a threshold level for 2 out of the 3 blade comparisons. The algorithm that is based on transmission ratios requires minimal data processing but is not robust, because system noise cannot be incorporated. Noise is unavoidable, and is the term which creates false alarms even when there is no blade damage. The residual algorithm utilizes a stochastic model that incorporates noise (using an i.i.d. Gaussian random variable), and reduces false alarming.

The effectiveness of the proposed SHM algorithms was evaluated using strain data from the 2.5 MW Eolos wind turbine. Using the transmission ratio approach, simulated damage of 20% increase in harvested energy (due to local stiffness loss) could be detected by a heuristically chosen 10% threshold. For the residual stochastic approach, statistics data during the period from May to November 2013 of the 2.5 MW turbine

were used to characterize the system noise. The propagation of standard deviation from the Eolos data was well matched with the proposed Gaussian model of noise. The standard deviation of the residual followed the trend of wind speed and turbine power output. Damage detection also depends on the available strain energy \bar{B} and the level of degradation g_D . If either \bar{B} or g_D (or both) is large, the damage can be more quickly detected. To quantify g_D , a finite element model of a thin-walled tapered hollow beam was simulated for appropriate damage scenarios of 0.25-1.1 m² damage size with 20% and 40% loss in stiffness. The calculated damage factor ranged from 0.0005 to 0.0035. For a damage factor of 0.0017, blade damage could be detected after 200 days with $p_{FP} = 0.7\%$ and $p_{TP} = 90\%$ by a stamp-sized EH. An enhanced energy harvester by either increasing the EH surface area or efficiency can reduce the decision time.

The proposed SHM system can provide early warning of the onset of damage even with this basic algorithm. Using a redundant approach, the algorithm does not require detailed design or operating conditions such as loading, the blade geometry, composite material properties, and boundary conditions. The SHM algorithm that is based on residuals allows for a user to define the detection accuracy, and a high detection probability can be expected with limited information.

This dissertation provided fundamentals to design an SHM system. Based on this study, further investigations on harvested strain energy and noise can improve the SHM system. The decision time can be reduced by increasing harvested energy and decreasing noise. Harvested energy depends on the capability of the EH, and lower noise can be expected by an enhanced EH. The source of noise needs to be studied thoroughly. Dynamic correlation of noise to environmental factors including an EH and wind loading can provide a key to reduce noise. The study of applying a non-stationary random variable with various distribution functions is left for future work.

The system can be also improved by a multiple-sensor network. Because the proposed system is wireless, the sensing nodes can be installed on a currently operational turbine (retrofit). Unlike other wire-based methods, wireless SHM offers installation flexibility at low cost, and the sensor-network can be easily expanded. With multiple sensors on a blade along the longitudinal direction, the algorithm can potentially locate damage and quantify the severity of damage (prognosis), comparing neighboring EHs.

Due to its low cost and easy installation, the sensor-network can be expanded to an entire wind farm. Expanding the sensor network to include SCADA (supervisory control and data acquisition) data or multiple turbine EH/sensor data could lead to improved statistical performance (p_{FP} and p_{TP}).

Chapter 7

References

- [1] Lucy Y Pao and Kathryn E Johnson. A tutorial on the dynamics and control of wind turbines and wind farms. In *American Control Conference, 2009. ACC'09.*, pages 2076–2089. IEEE, 2009.
- [2] Lord Microstrain. [http://files.microstrain.com/EH-Link_Datasheet_\(8400-0071\).pdf](http://files.microstrain.com/EH-Link_Datasheet_(8400-0071).pdf). Accessed: 2015-01-01.
- [3] Jason M Jonkman and Marshall L Buhl Jr. Fast user's guide. *Golden, CO: National Renewable Energy Laboratory*, 2005.
- [4] Department of Defense. *2014 Climate change adaptation roadmap*. Department of Defense, 2014.
- [5] Global Wind Energy Council. *Global Wind Energy Outlook*. Global Wind Energy Council, 2014.
- [6] Report of the US Energy Information Administration (EIA). *Levelized Cost of New Generation Resources in the Annual Energy Outlook 2013*. The U.S. Department of Energy (DOE), 2013.
- [7] Global Wind Energy Council. *Global Wind Statistics 2013*. Global Wind Energy Council, 2014.
- [8] Steve Lindenberg. 20% wind energy by 2030. *Energy Efficiency and Renewable Energy Department, TN, USA*, 2008.

- [9] M Mohsin Khan, M Tariq Iqbal, and Faisal Khan. Reliability and condition monitoring of a wind turbine. In *Electrical and Computer Engineering, 2005. Canadian Conference on*, pages 1978–1981. IEEE, 2005.
- [10] Caithness windfarm information forum, wind turbine accident data to december 31st 2005. <http://www.caithnesswindfarms.co.uk/>. Accessed: 2015-01-01.
- [11] Berthold Hahn, Michael Durstewitz, and Kurt Rohrig. Reliability of wind turbines. In *Wind energy*, pages 329–332. Springer, 2007.
- [12] Mark A Rumsey and Joshua A Paquette. Structural health monitoring of wind turbine blades. In *The 15th International Symposium on: Smart Structures and Materials & Nondestructive Evaluation and Health Monitoring*, pages 69330E–69330E. International Society for Optics and Photonics, 2008.
- [13] Hoon Sohn, Charles R Farrar, Francois M Hemez, Devin D Shunk, Daniel W Stinemat, Brett R Nadler, and Jerry J Czarnecki. *A review of structural health monitoring literature: 1996-2001*. Los Alamos National Laboratory Los Alamos, NM, 2004.
- [14] Anders Rytter and Poul Henning Kirkegaard. *Vibration based inspection of civil engineering structures*. Aalborg Universitetsforlag, 1994.
- [15] Mark Bolinger. 2008 wind technologies market report. *Lawrence Berkeley National Laboratory*, 2010.
- [16] Flemming Moeller Larsen and Troels Sorensen. New lightning qualification test procedure for large wind turbine blades. In *Proceedings of International Conference on Lightning and Static Electricity, Blackpool, UK*, 2003.
- [17] R. Poore and T. Lettenmaier. Alternative design study report: Windpact advanced wind turbine drive train designs study; november 1, 2000–february 28, 2002. Technical report, National Renewable Energy Laboratory (NREL), Golden, CO., 2003.
- [18] Eric Rosenbloom. A problem with wind power. *linked table Size Specifications of Common Industrial Wind Turbines*. <http://www.aweo.org/windmodels.html> (accessed February 20, 2013), 2006.

- [19] M. Jureczko, M. Pawlak, and A. Mezyk. Optimisation of wind turbine blades. *Journal of Materials Processing Technology*, 167(2):463–471, 2005.
- [20] D.R.V. Van Delft, G.D. De Winkel, and P.A. Joosse. Fatigue behaviour of fibreglass wind turbine blade material under variable amplitude loading. In *1997 ASME Wind Energy Symposium*, pages 180–188, 1997.
- [21] J.F. Mandell. Fatigue behavior of short fiber composite materials. *Fatigue of composite materials*, 4:231–337, 1990.
- [22] Herbert Sutherland. On the fatigue analysis of wind turbines. 1999.
- [23] Gyuhae Park, Tajana Rosing, Michael D Todd, Charles R Farrar, and William Hodgkiss. Energy harvesting for structural health monitoring sensor networks. *Journal of Infrastructure Systems*, 14(1):64–79, 2008.
- [24] Jerome P Lynch, Kincho H Law, Anne S Kiremidjian, John E Carryer, Thomas W Kenny, Aaron Partridge, and Arvind Sundararajan. Validation of a wireless modular monitoring system for structures. In *SPIE's 9th Annual International Symposium on Smart Structures and Materials*, pages 124–135. International Society for Optics and Photonics, 2002.
- [25] Jerome P Lynch and Kenneth J Loh. A summary review of wireless sensors and sensor networks for structural health monitoring. *Shock and Vibration Digest*, 38(2):91–130, 2006.
- [26] Jerome P Lynch, Kincho H Law, Anne S Kiremidjian, Thomas W Kenny, Ed Carryer, and A Partridge. The design of a wireless sensing unit for structural health monitoring. In *Proceedings of the 3rd International Workshop on Structural Health Monitoring*, pages 12–14, 2001.
- [27] Chia Chen Ciang, Jung-Ryul Lee, and Hyung-Joon Bang. Structural health monitoring for a wind turbine system: a review of damage detection methods. *Measurement Science and Technology*, 19(12), Dec 2008.
- [28] E. Peter Carden and Paul Fanning. Vibration based condition monitoring: a review. *Structural Health Monitoring*, 3(4):355–377, 2004.

- [29] Diogo Montalvao, Nuno Manuel Mendes Maia, and António Manuel Relógio Ribeiro. A review of vibration-based structural health monitoring with special emphasis on composite materials. *Shock and Vibration Digest*, 38(4):295–326, 2006.
- [30] Anindya Ghoshal, Mannur J Sundaresan, Mark J Schulz, and P Frank Pai. Structural health monitoring techniques for wind turbine blades. *Journal of Wind Engineering and Industrial Aerodynamics*, 85(3):309–324, 2000.
- [31] Jonathan White, Douglas Adams, Mark Rumsey, Jeroen Van Dam, and Scott Hughes. Impact, loading and damage detection in carbon composite tx-100 wind turbine rotor blade. In *AIAA Aerospace Sciences Meeting and Exhibit Laboratory*, 2008.
- [32] Abraham Light-Marquez, Alexandra Sobin, Gyuhae Park, and Kevin Farinholt. Structural damage identification in wind turbine blades using piezoelectric active sensing. *Structural Dynamics and Renewable Energy, Volume 1*, pages 55–65, 2011.
- [33] Jose R Zayas, Joshua Paquette, and Rudolph J Werlink. Evaluation of nasa pzt sensor/actuator for structural health monitoring of a wind turbine blade. In *Conference paper AIAA*, volume 1020, 2007.
- [34] Krystal Deines, Timothy Marinone, Ryan Schultz, Kevin Farinholt, and Gyuhae Park. Modal analysis and SHM investigation of CX-100 wind turbine blade. *Rotating Machinery, Structural Health Monitoring, Shock and Vibration, Volume 5*, pages 413–438, 2011.
- [35] Corey Pitchford, Benjamin L Grisso, and Daniel J Inman. Impedance-based structural health monitoring of wind turbine blades. In *The 14th International Symposium on: Smart Structures and Materials & Nondestructive Evaluation and Health Monitoring*, pages 65321I–65321I. International Society for Optics and Photonics, 2007.
- [36] Mark J. Schulz and Mannur J. Sundaresan. *Smart sensor system for structural condition monitoring of wind turbines*, volume 2011. National Renewable Energy Laboratory, Golden, Colo., 2006.

- [37] Lars Lading, Malcolm McGugan, Peder Sendrup, Jørgen Rheinländer, and Jens Rusborg. *Fundamentals for remote structural health monitoring of wind turbine blades-a preproject. Annex B. Sensors and non-destructive testing methods for damage detection in wind turbine blades*. 2002.
- [38] A.G. Dutton, M.J. Blanch, P. Vionis, D. Lekou, D.R.V. van Delft, P.A. Joosse, A. Anastassopoulos, D. Kouroussis, T. Kossivas, T.P. Philippidis, T.T. Assimakopoulou, G. Fernando, C. Doyle, and A. Proust. Acoustic emission condition monitoring of wind turbine rotor blades: Laboratory certification testing to large scale in-service deployment. In *European Wind Energy Conference-EWEC*, 2003.
- [39] Seth Stovack Kessler. *Piezoelectric-based in-situ damage detection of composite materials for structural health monitoring systems*. PhD thesis, Massachusetts Institute of Technology, 2002.
- [40] Sukun Kim, Shamim Pakzad, David Culler, James Demmel, Gregory Fenves, Steven Glaser, and Martin Turon. Health monitoring of civil infrastructures using wireless sensor networks. In *Information Processing in Sensor Networks, 2007. IPSN 2007. 6th International Symposium on*, pages 254–263. IEEE, 2007.
- [41] Ning Xu, Sumit Rangwala, Krishna Kant Chintalapudi, Deepak Ganesan, Alan Broad, Ramesh Govindan, and Deborah Estrin. A wireless sensor network for structural monitoring. In *Proceedings of the 2nd international conference on Embedded networked sensor systems*, pages 13–24. ACM, 2004.
- [42] Alan Mainwaring, David Culler, Joseph Polastre, Robert Szewczyk, and John Anderson. Wireless sensor networks for habitat monitoring. In *Proceedings of the 1st ACM international workshop on Wireless sensor networks and applications*, pages 88–97. ACM, 2002.
- [43] Shigeru Aoki, Yozo Fujino, and Masato Abe. Intelligent bridge maintenance system using mems and network technology. In *Smart Structures and Materials*, pages 37–42. International Society for Optics and Photonics, 2003.
- [44] Jerome P Lynch, Kincho H Law, Anne S Kiremidjian, Thomas W Kenny, Ed Carryer, and A Partridge. The design of a wireless sensing unit for structural health

- monitoring. In *Proceedings of the 3rd International Workshop on Structural Health Monitoring*, pages 12–14, 2001.
- [45] Steven W Arms, Christopher P Townsend, David L Churchill, SM Moon, and N Phan. Energy harvesting wireless sensors for helicopter damage tracking. In *ANNUAL FORUM PROCEEDINGS-AMERICAN HELICOPTER SOCIETY*, volume 62, page 1336. AMERICAN HELICOPTER SOCIETY, INC, 2006.
- [46] Lord Microstrain. <http://www.microstrain.com/energy-harvesting/eh-link>. Accessed: 2015-01-01.
- [47] Randall Swisher. Keys to achieving 20 percent wind by 2030. *Cogeneration and Distributed Generation Journal*, 24(3):66–77, 2009.
- [48] Josef Kryger Tadich and Jakob Wedel-Heinen. Optimisation of blade testing - a practical application of damage tolerance. In *Proceedings of EWEC 2008*. European Wind Energy Conference & Exhibition, 2008.
- [49] Kerstin Schroeder, Wolfgang Ecke, Jörg Apitz, Elfrun Lembke, and Gerhard Lenschow. A fibre bragg grating sensor system monitors operational load in a wind turbine rotor blade. *Measurement Science and Technology*, 17(5):1167, 2006.
- [50] Sandia National Laboratory, NuMAD (Numerical Manufacturing and Design tool). <http://http://energy.sandia.gov/energy/renewable-energy/wind-power/rotor-innovation/numerical-manufacturing-and-design-tool-numad/>. Accessed: 2015-01-01.
- [51] NWTC design codes (aerodyn by dr. david j. laino). <http://wind.nrel.gov/designcodes/simulators/aerodyn/>. Accessed: 2015-01-01.
- [52] A.D. Wright and L.J. Fingersh. Advanced control design for wind turbines, 2008.
- [53] D.J. Malcolm and A.C. Hansen. *WindPACT Turbine Rotor Design Study: June 2000–June 2002*. National Renewable Energy Laboratory, 2002.
- [54] Jason Mark Jonkman, Sandy Butterfield, Walter Musial, and G Scott. *Definition of a 5-MW reference wind turbine for offshore system development*. National Renewable Energy Laboratory Golden, CO, 2009.

- [55] Rusen Yang, Yong Qin, Liming Dai, and Zhong Lin Wang. Power generation with laterally packaged piezoelectric fine wires. *Nature Nanotechnology*, 4(1):34–39, 2008.
- [56] Eolos wind energy reserach consortium. <http://www.eolos.umn.edu>. Accessed: 2015-01-01.
- [57] Jerome P Lynch, Yang Wang, Kenneth J Loh, Jin-Hak Yi, and Chung-Bang Yun. Performance monitoring of the geumdang bridge using a dense network of high-resolution wireless sensors. *Smart Materials and Structures*, 15(6):1561, 2006.
- [58] Yang Wang, Kenneth J Loh, Jerome P Lynch, Michael Fraser, KH Law, and Ahmed Elgamal. Vibration monitoring of the voigt bridge using wired and wireless monitoring systems. In *Proceedings of the 4th China-Japan-US Symposium on Structural Control and Monitoring*, pages 16–17, 2006.
- [59] Jerome Peter Lynch. An overview of wireless structural health monitoring for civil structures. *Philosophical Transactions of the Royal Society A: Mathematical, Physical and Engineering Sciences*, 365(1851):345–372, 2007.
- [60] N.C. Batista, R. Melício, J.C.O. Matias, and J.P.S. Catalão. Photovoltaic and wind energy systems monitoring and building/home energy management using zigbee devices within a smart grid. *Energy*, 49:306–315, 2013.
- [61] Andrea Sanchez Ramirez, Richard Loendersloot, and Tiedo Tinga. Helicopter rotor blade monitoring using autonomous wireless sensor network. *Key engineering materials*, 569:775–782, 2013.
- [62] Stuart G Taylor, Kevin M Farinholt, Gyuhae Park, Charles R Farrar, and Michael D Todd. Application of a wireless sensor node to health monitoring of operational wind turbine blades. In *Structural Dynamics and Renewable Energy, Volume 1*, pages 45–53. Springer, 2011.
- [63] Mark Mollineaux, Konstantinos Balafas, Kim Branner, Per Nielsen, Angelo Tesauro, Anne Kiremidjian, and Ram Rajagopal. Damage detection methods on wind turbine blade testing with wired and wireless accelerometer sensors. In *EWSHM-7th European Workshop on Structural Health Monitoring*, 2014.

- [64] Gangbing Song, Hui Li, Bosko Gajic, Wensong Zhou, Peng Chen, and Haichang Gu. Wind turbine blade health monitoring with piezoceramic-based wireless sensor network. *International Journal of Smart and Nano Materials*, 4(3):150–166, 2013.
- [65] Lan Xin Hu, Hai Bo Feng, and Hai Meng Yin. Remote wireless monitoring system for wind turbine. *Applied Mechanics and Materials*, 385:614–617, 2013.
- [66] Clinton P Carlson, Alexander D Schlichting, Scott Ouellette, Kevin Farinholt, and Gyuhae Park. Energy harvesting to power sensing hardware onboard wind turbine blade. In *Structural Dynamics and Renewable Energy, Volume 1*, pages 291–304. Springer, 2011.
- [67] Niell G Elvin, Nizar Lajnef, and Alex A Elvin. Feasibility of structural monitoring with vibration powered sensors. *Smart Materials and Structures*, 15(4):977, 2006.
- [68] Kevin M Farinholt, Stuart G Taylor, Gyuhae Park, and Charles R Farrar. Wireless energy transmission to supplement energy harvesters in sensor network applications. In *Proceedings SPIE7645, Industrial and Commercial Applications of Smart Structures Technologies*, pages 764505–764505. International Society for Optics and Photonics, 2010.
- [69] Russel Torah, Peter Glynne-Jones, M Tudor, T O’Donnell, S Roy, and Steve Beeby. Self-powered autonomous wireless sensor node using vibration energy harvesting. *Measurement Science and Technology*, 19(12):125202, 2008.
- [70] Noël E Dutoit, Brian L Wardle, and Sang-Gook Kim. Design considerations for mems-scale piezoelectric mechanical vibration energy harvesters. *Integrated Ferroelectrics*, 71(1):121–160, 2005.
- [71] Alper Erturk and Daniel J Inman. Piezoelectric power generation for civil infrastructure systems. In *SPIE Smart Structures and Materials+ Nondestructive Evaluation and Health Monitoring*, pages 798326–798326. International Society for Optics and Photonics, 2011.
- [72] Joseph Davidson and Changki Mo. Recent advances in energy harvesting technologies for structural health monitoring applications. *Smart Materials Research*, 2014, 2014.

- [73] Stephen R Platt, Shane Farritor, and Hani Haider. On low-frequency electric power generation with pzt ceramics. *Mechatronics, IEEE/ASME Transactions on*, 10(2):240–252, 2005.
- [74] Chengliang Sun, Jian Shi, and Xudong Wang. Fundamental study of mechanical energy harvesting using piezoelectric nanostructures. *Journal of Applied Physics*, 108(3):034309, 2010.
- [75] Cecilia D Richards, Michael J Anderson, David F Bahr, and Robert F Richards. Efficiency of energy conversion for devices containing a piezoelectric component. *Journal of Micromechanics and Microengineering*, 14(5):717, 2004.
- [76] Michael Goldfarb and Lowell D Jones. On the efficiency of electric power generation with piezoelectric ceramic. *Journal of Dynamic Systems, Measurement, and Control*, 121(3):566–571, 1999.
- [77] Y.C. Shu and I.C. Lien. Efficiency of energy conversion for a piezoelectric power harvesting system. *Journal of micromechanics and microengineering*, 16(11):2429, 2006.
- [78] Nesbitt W Hagood and Andreas von Flotow. Damping of structural vibrations with piezoelectric materials and passive electrical networks. *Journal of Sound and Vibration*, 146(2):243–268, 1991.
- [79] F. Lu, H.P. Lee, and S.P. Lim. Modeling and analysis of micro piezoelectric power generators for micro-electromechanical-systems applications. *Smart Materials and Structures*, 13(1):57, 2004.
- [80] Smart Material corp. <http://www.smart-material.com/MFC-product-main.html>. Accessed: 2015-01-01.
- [81] Dong-Won Lim, Susan C. Mantell, Peter J. Seiler, and Rusen Yang. Wind turbine blades as a strain energy source for energy harvesting. In *51st AIAA Aerospace Sciences Meeting including the New Horizons Forum and Aerospace Exposition*, 2013.

- [82] Douglas Adams. *Health monitoring of structural materials and components: methods with applications*. John Wiley & Sons, 2007.
- [83] Y.C. Yeh. Triple-triple redundant 777 primary flight computer. In *Aerospace Applications Conference, 1996. Proceedings., 1996 IEEE*, volume 1, pages 293–307. IEEE, 1996.
- [84] Y.C. Yeh. Safety critical avionics for the 777 primary flight controls system. In *Digital Avionics Systems, 2001. DASC. 20th Conference*, volume 1, pages 1C2–1. IEEE, 2001.
- [85] Richard PG Collinson. *Introduction to avionics systems*. Springer, 2011.
- [86] The liberty 2.5 mw wind turbine: Clipper design. <http://www.clipperwind.com>. Accessed: 2014-06-01.
- [87] Douglas Adams, Jonathan White, Mark Rumsey, and Charles Farrar. Structural health monitoring of wind turbines: method and application to a hawt. *Wind Energy*, 14(4):603–623, 2011.
- [88] Abraham Light-Marquez, Alexandra Sobin, Gyuhae Park, and Kevin Farinholt. Structural damage identification in wind turbine blades using piezoelectric active sensing. In *Structural Dynamics and Renewable Energy, Volume 1*, pages 55–65. Springer, 2011.
- [89] Dong-Won Lim, Susan C. Mantell, and Peter J. Seiler. Wireless structural health monitoring of wind turbine blades using an energy harvester as a sensor. In *AIAA 52nd Aerospace Sciences Meeting, National Harbor Maryland*, 2014.
- [90] Joshua Paquette, Scott Hughes, Jeroen van Dam, and Jay Johnson. Fatigue testing of 9 m carbon fiber wind turbine research blades. In *46th AIAA Aerospace Sciences Meeting and Exhibit, Reno, NV*, pages 1–2, 2008.
- [91] John Rice. *Mathematical statistics and data analysis*. Cengage Learning, 2006.
- [92] Jason Mark Jonkman, Sandy Butterfield, Walter Musial, and G Scott. *Definition of a 5-MW reference wind turbine for offshore system development*. National Renewable Energy Laboratory Golden, CO, 2009.

- [93] Prashant M Pawar and Ranjan Ganguli. Modeling progressive damage accumulation in thin walled composite beams for rotor blade applications. *Composites science and technology*, 66(13):2337–2349, 2006.
- [94] Robert J Bleeg. Commercial jet transport fly-by-wire. *AIAA/IEEE Digital Avionics Systems Conference*, pages 399–406, 1988.

Appendix A

Examples and Validation for Energy Harvesting

A.1 Examples of Input Energy Calculation

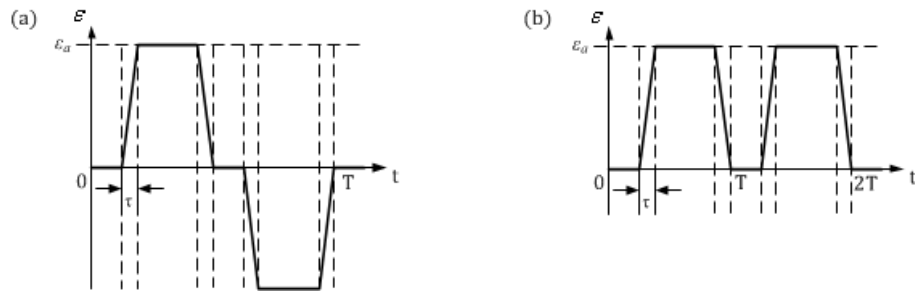


Figure A.1: Two Excitations of Strain Input to EHs

Example 1. Consider two harmonic excitation modes as shown in Figure A.1. For the case (a), an EH is under a fully reversed excitation. The available strain energy $W_{in,a}$ for one cycle as in the figure can be obtained by

$$W_{in,a}^{(1)} = 2 \cdot \frac{1}{2} V E \frac{\epsilon_a^2}{\tau} \tau = 1 \cdot V E \epsilon_a^2. \quad (\text{A.1})$$

Eq. A.1 can be generalized for n cycles as

$$W_{in,a}^{(n)} = n \cdot V E \epsilon_a^2. \quad (\text{A.2})$$

For the case (b), an EH is stretched only in one direction by ϵ_b for two cycles. In this case, ϵ_b is a peak-to-peak value, and a root-mean-square (RMS) amplitude is used in the form of Eq. A.2 in the same way. $W_{in,b}$ can be calculated as

$$W_{in,b}^{(2)} = 2 \cdot \frac{1}{2} VE \frac{\epsilon_b^2}{\tau} \tau = 2 \cdot \left(\frac{\epsilon_b}{\sqrt{2}} \right)^2 VE. \quad (\text{A.3})$$

A general equation for a peak-to-peak amplitude ϵ_b with n cycles can be expressed as

$$W_{in,b}^{(n)} = n \cdot VE \left(\frac{\epsilon_b}{\sqrt{2}} \right)^2. \quad (\text{A.4})$$

In Figure A.2, available strain energy is depicted for each case. The figure confirms

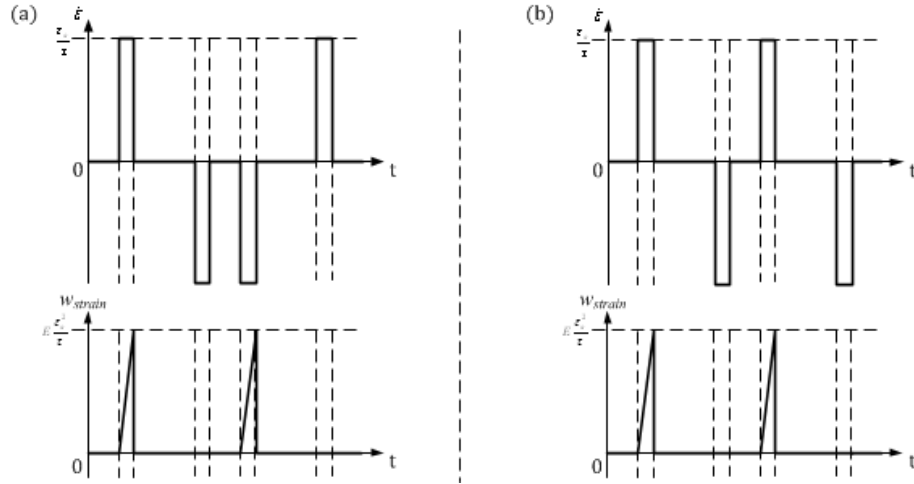


Figure A.2: Two Excitations of Strain Input to EHs

that two cases for a mean-to-peak and peak-to-peak amplitude have identical amount of input energy in the same expression as Eqs. (A.2 and A.4).

Example 2. Consider a singular harmonic strain function $\epsilon(t)$ for thirty cycles (60 secs).

$$\epsilon(t) = 2 \sin 2\pi \frac{1}{2} t. \quad (\text{A.5})$$

The strain energy can be calculated by the discretized method in Eq. 3.16, and the result is compared to an analytic value in Eq. 3.14 as follows.

Solution From Eq. (3.14),

$$W_{exact} = 60 \times 2 \frac{1}{2} \times \frac{1}{2} VE \times 2^2 = 120VE \quad (\text{A.6})$$

Using Eq. (3.16) and 10^3 discrete steps, then

$$\Delta t = \frac{6}{10000} = 0.006 \quad (\text{A.7})$$

$$\epsilon_k = 2 \sin(0.006\pi k), \quad (k = 0, 1, \dots, 10000), \quad (\text{A.8})$$

and

$$W_{num} = VE \sum_1^{10000} \epsilon_k \cdot (\epsilon_k - \epsilon_{k-1}) \quad , \text{ if } \epsilon_k \cdot (\epsilon_k - \epsilon_{k-1}) > 0 \quad (\text{A.9})$$

$$W_{num} = 0 \quad , \text{ else } . \quad (\text{A.10})$$

Numeric simulation gives W_{num} of $121.78VE$. The simulation result will become close to the exact solution W_{exact} of $120VE$ with increased step number.

A.2 Validation of the Experiment Set-up

This section presents the strain calculation for the design and strain validation. First, the way to obtain a uniform strain field is explained. While the bending moment $M(x)$ increases to the root, the width $b(x)$ also increases as shown in the diagrams. The longitudinal position variable x in $b(x)$ cancels the x in $M(x)(=Fx)$ of the strain equation. The strain in the span of $\frac{L}{2} \leq x \leq L$ is found by

$$\epsilon(x) = \frac{My}{EI} = \frac{Fx \frac{h}{2}}{E \frac{b_0 x h^3}{12L}} = \frac{6FL}{Eb_0 h^2} (= \epsilon_L) \quad \left(\frac{L}{2} \leq x \leq L\right). \quad (\text{A.11})$$

As in Eq. A.11, the strain $\epsilon(x)$ is independent of x , and this implies that the strain is constant.

Second, the set-up is validated by discrete strain values calculated both analytically (Figure A.3) and numerically (Figure A.4) using commercial software. Calculated values were matched to strain gage measurements as well. A desired strain value in the triangle area is set by a tip displacement (which is measured and controlled easily rather than using tip forces). Then, strain needs to be expressed in terms of a tip displacement $\delta(0)$ that can be specified by the exciter. $\delta(0)$ can be obtained from displacements $\delta(x)$ over the length of the beam as

$$\delta(x) = \frac{1}{EI} \int \int M(x) dx^2 = \frac{F}{E \frac{b_0 x h^3}{12L}} \left(\frac{1}{6} x^3 - \frac{1}{2} L^2 x + \frac{1}{3} L^3 \right). \quad (\text{A.12})$$

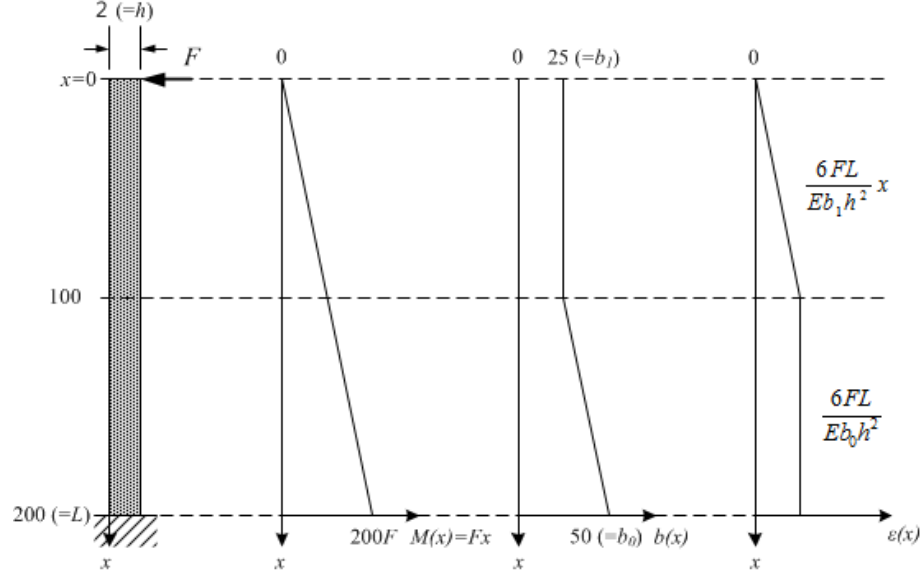


Figure A.3: Strain and Moment Distribution Charts for an Experimental Beam

The tip displacement is at $x = 0$ as

$$\delta(0) = \frac{8FL^3}{Eb_0h^3} \quad (\text{A.13})$$

which equates the tip force F as

$$F = \frac{Eb_0h^3}{8L^3}\delta(0). \quad (\text{A.14})$$

Substitute F into the strain Eq. A.11 and we get the strain in terms of the tip displacement $\delta(0)$ is the formula from the strain to the displacement.

$$\epsilon(L) = \frac{6L}{Eb_0h^2} \cdot \frac{Eb_0h^3}{8L^3}\delta(0) = \frac{3h}{4L^2}\delta(0). \quad (\text{A.15})$$

The command input $\delta(0)$ of the tip actuation can be dictated by a desired $\epsilon(L)$ as

$$\delta(0) = \frac{4L^2}{3h}\epsilon(L). \quad (\text{A.16})$$

From Eq. A.15, the analytic strain value is 370 μ -strain in the triangular area when $\delta(0) = 10\text{mm}$. Numerical analysis gave strain values from 510 to 552 μ -strain (42 μ -strain (8%) difference) in the area. Measured values are 311 (bottom) and 349 (top)

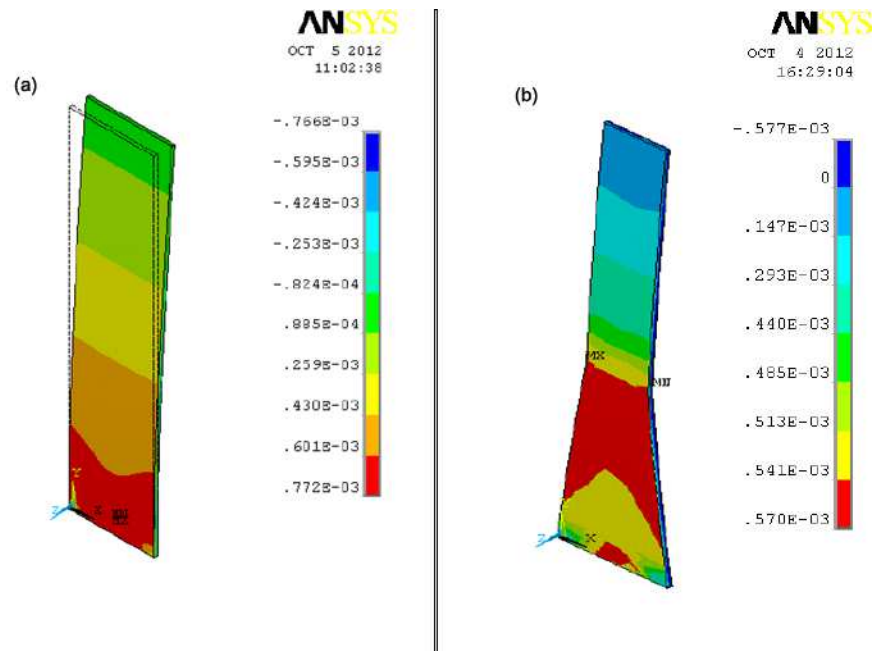


Figure A.4: ANSYS simulation validates beam design to have uniform strain field. A straight beam (a) has greater strain gradient from its root to the tip than a tapered beam (b), which has smaller variation in the one-third area.

μ -strain with 38 μ -strain difference (12%). Both the simulation and experiment showed top and bottom values in a good agreement with small difference ($\sim 10\%$). Particularly, the simulation results have higher values than the analytic or experimental values. The thickness of the beam is only 2 mm and thin, and the width decreases to the tip. While the analytic solution is derived from a beam theory, the design beam had been actually behaving like a plate, and the radius of curvature approaching to the notches inevitably increased while bending. On the contrary, a linear beam has a uniform radius of curvature in any longitudinal location. But measurements were smaller than numeric simulation results (or were close to the analytic solution), because the root constraint does not perfectly hold the beam, and material properties may not be exact to numbers simulated.

Figure A.4 (a) shows also the strain gradient of a straight beam which is bent by the same amount of the tip displacement to the designed beam in (b). For this straight

beam, a top gage and a bottom gage—of the same locations of the triangular beam (b)—gives 495 μ -strain and 697 μ -strain respectively (difference of ~ 200 μ -strain, 40%). This result confirms the validity of the new design proposed in Figure 3.4.

Appendix B

Strain Energy Estimation

Wireless sensor nodes generate pulses when electricity converted from strain energy by an EH is sufficient. Three sensor nodes installed in each blade are cross-compared, yielding a strain-energy residual. In general, pulses generated by three nodes are not only asynchronous but also infrequent as shown in Figure B.1. Thus, strain energy is estimated from pulses, and this section explains the procedure of the estimation and the size of the estimation error.

B.1 Least Square Estimation

Let W° be the amount of energy use for one time transmission, n the number of pulses received during the inspection window and θ the total interval (steps) between the inspection times. Then, \bar{B} is a mean of strain increments from the previous inspection time to the current time.

$$\bar{B} = \frac{\text{Number of Pulses} \times \text{Energy/Pulse}}{\text{Statistical Evaluation Time}} = \frac{n \cdot W^\circ}{n \cdot \theta} = \frac{W^\circ}{\theta}. \quad (\text{B.1})$$

And the per time step harvested energy B_k can be rewritten having \bar{B} and a time variational term v_k such as

$$B_k = \bar{B} + v_k. \quad (\text{B.2})$$

When v_k is Gaussian and IID, the best estimate of strain energy at step k is

$$\hat{W}_k = \left(\frac{1}{\theta} k + n - 1 \right) \cdot W^\circ. \quad (\text{B.3})$$

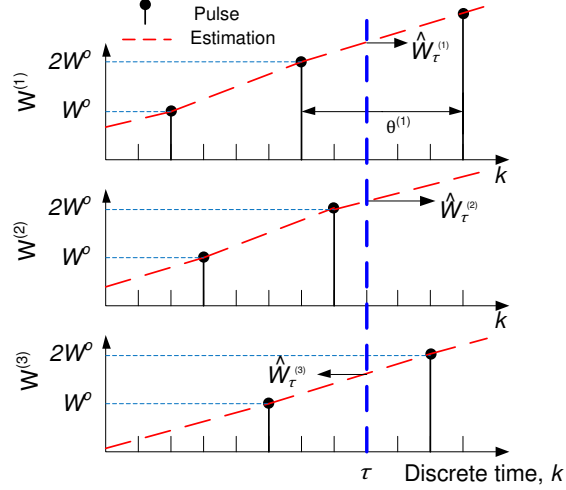


Figure B.1: Discrete Pulses over Time: Asynchronous pulses of three EHs are shown, and accumulated strain energy can be estimated by interpolation between two neighboring pulses.

Proof. Let $\mathbf{B} \in \mathfrak{R}^{\theta \times 1}$, $\bar{\mathbf{W}} = W^0 \mathbf{1}^{\theta \times 1}$, $x \in \mathfrak{R}$, $\mathbf{v} \in \mathfrak{R}^{\theta \times 1}$, $k \in [1, 2, \dots, \theta]$, and strain energy time increment equation is

$$\mathbf{B} = \bar{\mathbf{W}} \cdot x + \mathbf{v}. \quad (\text{B.4})$$

If we get the best estimate of the strain increment, then we can get the best estimate of the strain energy. So, let's find the best estimate of energy increment instead of \bar{W} .

$$\hat{\mathbf{B}} = \bar{\mathbf{W}} \cdot \hat{x} \quad (\text{B.5})$$

where

$$x \in \left\{ \frac{1}{1}, \frac{1}{2}, \dots, \frac{1}{\theta} \right\}. \quad (\text{B.6})$$

Let a cost function J be

$$J = (\mathbf{B} - \hat{\mathbf{B}})^T \cdot (\mathbf{B} - \hat{\mathbf{B}}) = (\mathbf{B} - \hat{\mathbf{W}} \cdot \hat{x})^T \cdot (\mathbf{B} - \bar{\mathbf{W}} \cdot \hat{x}) \quad (\text{B.7})$$

$$= \mathbf{B}^T \mathbf{B} - \hat{x}^T \bar{\mathbf{W}}^T \mathbf{B} - \mathbf{B}^T \bar{\mathbf{W}} \hat{x} + \hat{x}^T \bar{\mathbf{W}}^T \bar{\mathbf{W}} \hat{x}. \quad (\text{B.8})$$

And minimize the cost function J over a free variable \hat{x} as

$$\frac{\partial J}{\partial \hat{x}} = -\mathbf{B}^T \bar{\mathbf{W}} - \mathbf{B}^T \bar{\mathbf{W}} + 2\hat{x}^T \bar{\mathbf{W}}^T \bar{\mathbf{W}} = 0. \quad (\text{B.9})$$

$$\bar{\mathbf{W}}^T \bar{\mathbf{W}} \hat{x} = \bar{\mathbf{W}}^T \mathbf{B}. \quad (\text{B.10})$$

Thus, the best estimate \hat{x} can be obtained as

$$\hat{x} = \left(\bar{\mathbf{W}}^T \bar{\mathbf{W}} \right)^{-1} \bar{\mathbf{W}}^T \mathbf{B} \quad (\text{B.11})$$

$$= \left(W^{\circ 2} \begin{bmatrix} 1 & 1 & \dots & 1 \end{bmatrix} \begin{bmatrix} 1 \\ 1 \\ \vdots \\ 1 \end{bmatrix} \right)^{-1} \cdot W^{\circ} \begin{bmatrix} 1 & 1 & \dots & 1 \end{bmatrix} \cdot \begin{bmatrix} B_1 \\ B_2 \\ \vdots \\ B_{\theta} \end{bmatrix} \quad (\text{B.12})$$

$$= \frac{W^{\circ}}{W^{\circ 2}(1 + 1 + \dots + 1)} \cdot \Sigma_1^{\theta} B_i \quad (\text{B.13})$$

$$= \frac{1}{\theta W^{\circ}} \cdot W^{\circ} = \frac{1}{\theta}. \quad (\text{B.14})$$

Thus,

$$\hat{\mathbf{B}} = \bar{\mathbf{W}} \cdot \frac{1}{\theta} = \bar{B} \cdot \mathbf{1}^{\theta \times 1} \quad (\text{B.15})$$

, and total energy is aggregated from the initial pulse for n pulses as

$$\hat{W}_k = (k \cdot + (n - 1)\theta) \bar{B} = \left(\frac{k}{\theta} + n - 1 \right) \cdot W^{\circ}. \quad (\text{B.16})$$

■

Figure B.2 is provided to illustrate how estimated quantities are compared to true values by using the least square estimation in the above method.

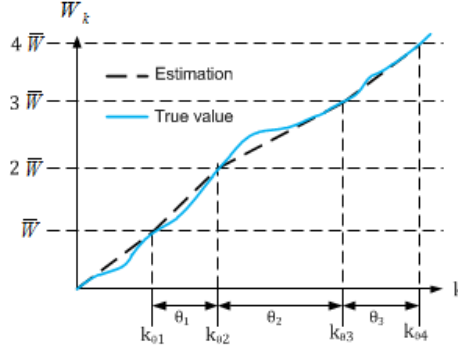


Figure B.2: Concept of Estimated Strain Energy Over Discrete Time, k

B.2 Propagation Error of Estimation

The size of estimation error can be obtained by calculating the covariance P_k of the error.

$$P_k = E[(W_k - \hat{W}_k) \cdot (W_k - \hat{W}_k)^T] \quad (\text{B.17})$$

$$= E\left[\left(\sum_{i=1}^k B_i - k\bar{B}\right) \cdot \left(\sum_{i=1}^k B_i - k\bar{B}\right)^T\right] \quad (\text{B.18})$$

$$= E\left[\sum_{i=1}^k v_i \cdot \sum_{i=1}^k v_i^T\right] \quad (\text{B.19})$$

For a scalar system, having the property of the variance v_i as

$$E[v_i] = 0, \text{ and } E[v_i^2] = \sigma^2, \quad (\text{B.20})$$

(B.17) becomes

$$P_k = k\sigma^2 + 2\{E[v_1v_2] + E[v_1v_3] + \dots + E[v_{k-1}v_k]\}. \quad (\text{B.21})$$

Note the fact that the sum of variations v s in one interval becomes zero:

$$\sum_{i=1}^{\theta} v_i = 0 \quad (\text{B.22})$$

From (B.22),

$$\sum_{i,j=1}^{\theta} E[v_iv_j] = -\frac{\theta\sigma^2}{2}, \text{ for } i \neq j. \quad (\text{B.23})$$

If any two noise terms are equally correlated, and then from (B.23)

$$E[v_i v_j] = -\frac{\sigma^2}{\theta - 1}, \quad (i \neq j). \quad (\text{B.24})$$

Therefore, P_k becomes

$$P_k = k\sigma^2 - 2\frac{k(k-1)}{2}\frac{\sigma^2}{\theta-1} = \frac{k(\theta-k)}{\theta-1}\sigma^2 \quad (\text{B.25})$$

The maximum error occurs at $k = \frac{\theta}{2}$ as

$$\max[P_k] = \frac{\theta^2}{4(\theta-1)}\sigma^2 \quad (\text{B.26})$$

Thus, the error is maximum in the half of a pulse interval, and there is no error at the moments of pulse receipt.

Appendix C

Monthly statistics for residuals

To design an SHM system (a threshold T and decision time τ), a random walk model with a Gaussian random variable was used for a residual. The variance σ^2 and mean strain energy increment \bar{B} in this model are needed. From the Eolos 2013 strain database, strain energy residuals are calculated. Based on the processed data, σ^2 and \bar{B} were obtained in Table xx for a long-term time scale of a month. Standard deviation propagation of a residual for each month from May to November 2013 is shown in Figures C.1 to C.6

C.1 Statistics Results

Table C.1: Monthly σ and \bar{B} for the SHM system design

Month	\bar{B} [$\mu\text{J}/\text{step}$]	σ [μJ]
May	0.0082	0.1314
June	0.008	0.1321
July	N/A	N/A
August	0.0104	0.1020
September	0.0121	0.1050
October	0.0063	0.1319
November	0.0117	0.3916
December	0.0099	0.5096

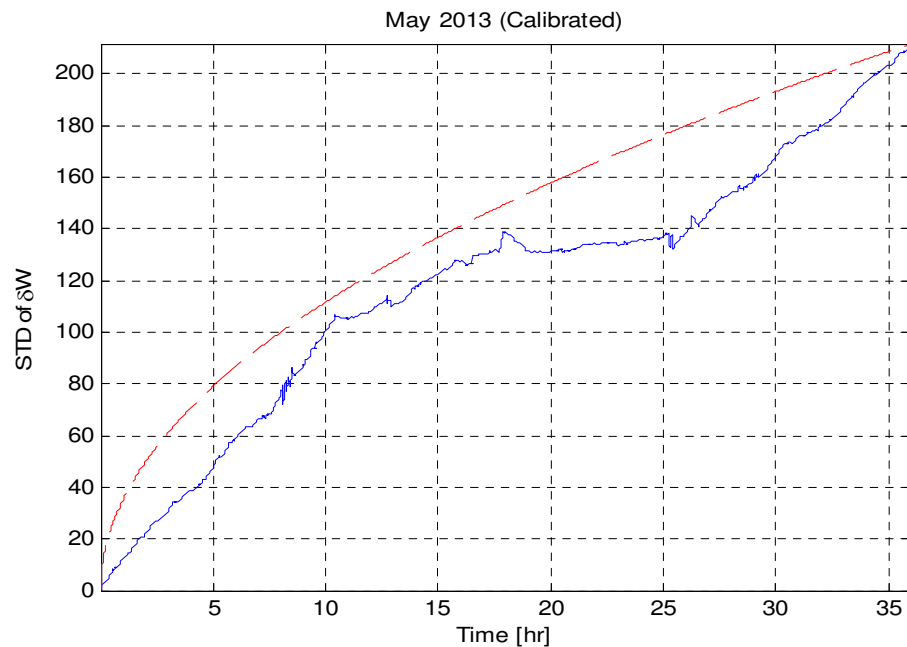


Figure C.1: Standard deviation propagation of a residual over 36 hours in May 2013 for Eolos Turbine Blades.

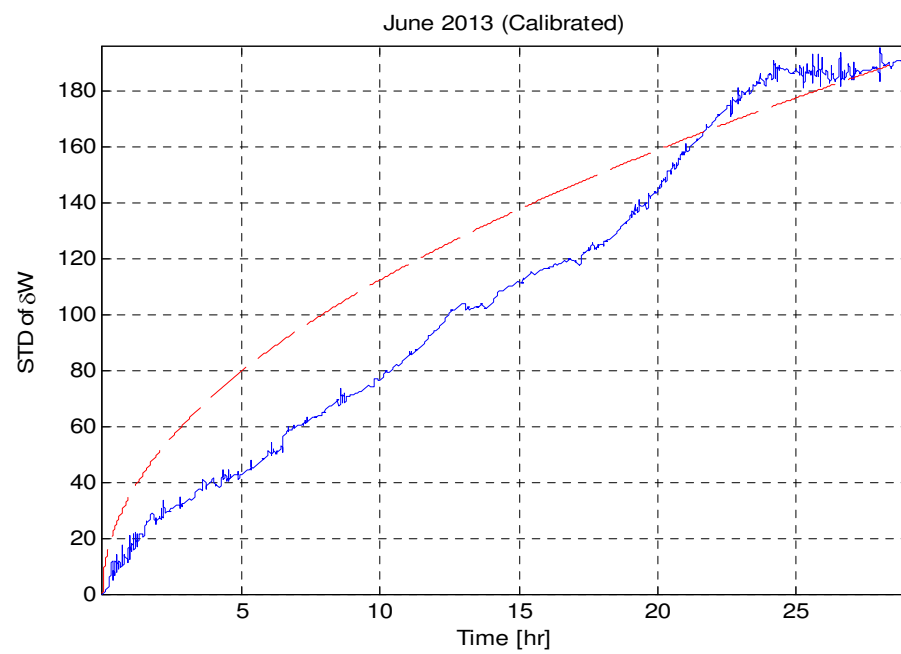


Figure C.2: Standard deviation propagation of a residual over 36 hours in June 2013 for Eolos Turbine Blades.

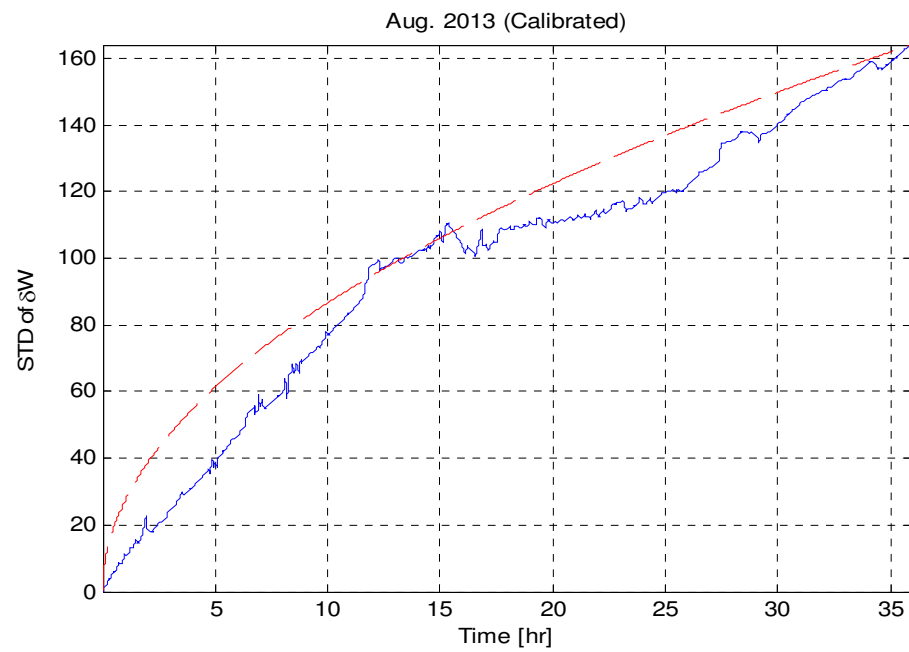


Figure C.3: Standard deviation propagation of a residual over 36 hours in August 2013 for Eolos Turbine Blades.

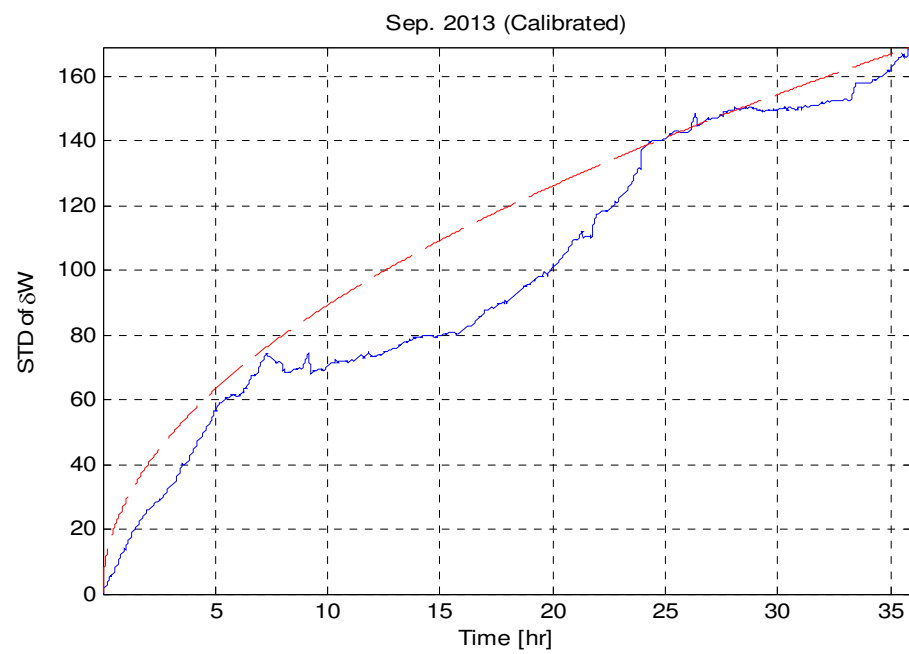


Figure C.4: Standard deviation propagation of a residual over 36 hours in September 2013 for Eolos Turbine Blades.

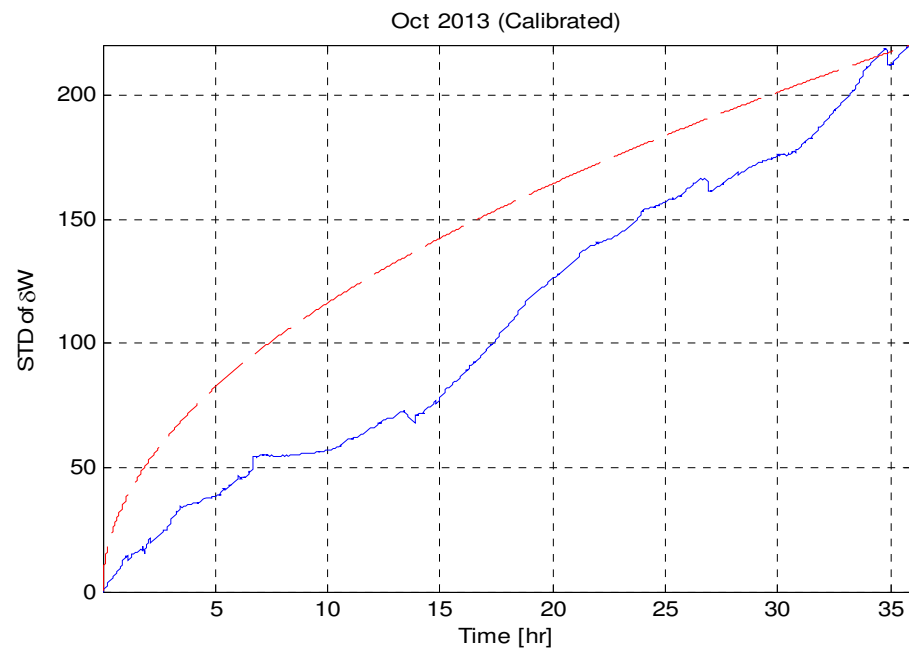


Figure C.5: Standard deviation propagation of a residual over 36 hours in October 2013 for Eolos Turbine Blades.

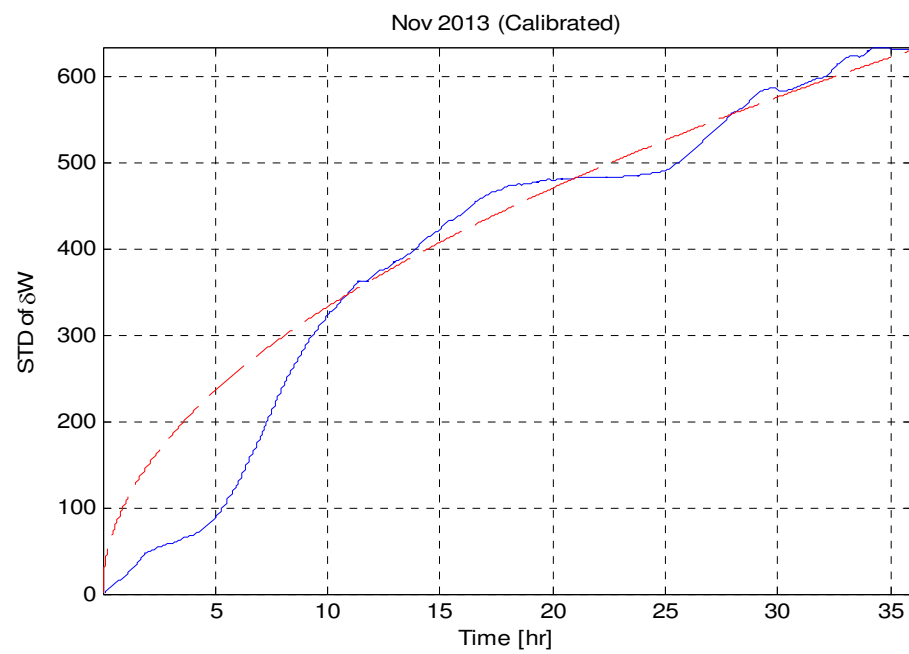


Figure C.6: Standard deviation propagation of a residual over 36 hours in November 2013 for Eolos Turbine Blades.

Appendix D

Matlab Codes

D.1 Pulse Calculation (EH an Telemetry)

```
function return_dT = PulseCal(BldST,Keh,W)
% Pulse Calculation by EH and Energy Demand W
%
%   EW = PulseCal(BldST,Keh,W,dix) simulates wireless transmission
%   with an energy demand W powered by an EH with Keh.
%   This returns pulse timing.
%   2013-11-13
%   Modified 2014/06/15
%   Dongwon Lim

k = 0:length(BldST)-1;

% Parameter setting
dBldST = [zeros(3,1) BldST(:,2:end) - BldST(:,1:end-1)];

%% Initialization
jx = [1 1 1];
[bldn,tend] = size(BldST);
EW = zeros(bldn,tend);
h = zeros(bldn,tend);
% Ix = h;
```

```

% dT = h;
%%
for j=2 : tend
    for i=1:bldn          % Blade #
        if BldST(i,j)*dBldST(i,j) > 0
            EW(i,j) = EW(i,j-1) + Keh*BldST(i,j)*dBldST(i,j)*1e6; % [uJ]
        else
            EW(i,j) = EW(i,j-1);
        end
    end
    h(:,j) = EW(:,j)/W;
    for i=1:bldn
        if floor(h(i,j)) - floor(h(i,j-1)) == 1
            Ix(i,jx(i)) = j;
            dT(i,jx(i)) = k(j);
            jx(i) = jx(i) + 1;
            EW(i,j) = 0;
        end
    end
end

%% Time diff.
% DdT = [dT(:,1) diff(dT,1,2)];
% M1 = interp1(dT,DdT,k);
% derv = diff(DdT)./diff(dT);

%% Checking
% figure; hold on;
% stem(dT(1,1:end-2),DdT(1,1:end-2),'b');
% stem(dT(2,1:end-2),DdT(2,1:end-2),'g');
% stem(dT(3,1:end-2),DdT(3,1:end-2),'r');

return_dT = dT;
end

```

D.2 Strain Energy Estimation

```

function EWtilde = EHest(dT,W,k)
% Energy Estimation Estimation of strain Energy
% EWtilde = EHest(dT,W), EWtilde contains three blades' estimated
% strain energy as a vector row, [EWtilde1; EWtilde2; EWtilde3].
% dT is a matrix consisting of three timing vectors of blades.
% W is required energy.
%
% Dongwon Lim 2014/02/04

nPul = length(dT);
EnW1 = 0;EnW2 = 0;EnW3 = 0;
nan1 = 0;nan2 = 0;nan3 = 0;
for i=1:nPul
    if dT(1,i) ~= 0
        EnW1 = [EnW1 i*W];
    else
        nan1 = nan1 + 1;
    end
    if dT(2,i) ~= 0
        EnW2 = [EnW2 i*W];
    else
        nan2 = nan2 + 1;
    end
    if dT(3,i) ~= 0
        EnW3 = [EnW3 i*W];
    else
        nan3 = nan3 + 1;
    end
end
EWtilde1 = interp1([0 dT(1,1:end-nan1)],EnW1,k);
EWtilde2 = interp1([0 dT(2,1:end-nan2)],EnW2,k);
EWtilde3 = interp1([0 dT(3,1:end-nan3)],EnW3,k);
EWtilde = [EWtilde1; EWtilde2; EWtilde3];

```

D.3 Harvested EH Strain Energy Simulation

```

function EW = EHCAL(BldST,Keh)
% Harvested EH Strain Energy Simulation Caculation
%
%   EW = EHCAL(BldST,Keh,dix) calculates harvested energy by an EH
%   with Keh efficiency and dix damage factor in Blade 3.
%   BldST is blade strain from raw data.
%   2013-11-13
%   Dongwon Lim

% Parameter setting
dBldST = [zeros(3,1) BldST(:,2:end) - BldST(:,1:end-1)];

% Energy accumulation Test
[bldn,tend] = size(BldST);
EW = zeros(bldn,tend);
for j=2 : tend
    for i=1:bldn          % Blade #
        if BldST(i,j)*dBldST(i,j) > 0
            EW(i,j) = EW(i,j-1) + Keh*BldST(i,j)*dBldST(i,j)*1e6; % [uJ]
        else
            EW(i,j) = EW(i,j-1);
        end
    end
end
end

```

D.4 Eolos Strain Calibration

```

% Calibration by Automation
% find c1 and c2 for minimum Bbar differences
% Dongwon Lim
% 2014/06/27

disp('--- Calibration is initiated ---');
c1 = 1; c3 = 1;
i = 1;
Bout12 = 1; Bout31 = 1;
T = 1e-5;
while abs(Bout12) > T || abs(Bout31) > T
    TotSTc(1,:) = c1*TotST(1,:);
    TotSTc(2,:) = TotST(2,:);
    TotSTc(3,:) = c3*TotST(3,:);
    EW = EHCal(TotSTc,Keh); % [uJ]
    dW1 = diff(EW(1,:)); dW2 = diff(EW(2,:)); dW3 = diff(EW(3,:));
    Bbar1 = mean(dW1); Bbar2 = mean(dW2); Bbar3 = mean(dW3);
    Bout12 = Bbar1-Bbar2;
    Bout23 = Bbar2-Bbar3;
    Bout31 = Bbar3-Bbar1;
    disp(['Round ' num2str(i) '| Bbar = ' num2str(Bout12) ' : ' ...
        num2str(Bout23) ' : ' num2str(Bout31)]);
    c1 = c1*(1-Bout12*20);
    c3 = c3*(1-Bout31*20);
    i = i + 1;
end
disp(['Correction c1 & c3 : ' num2str(c1) ', ' num2str(c3)]);

```

D.5 Eolos Strain Data Import

```

function [EdgST t] = EolosDataImporting(filename,delim,ix,hr)

% EolosDataImporting imports data from Eolos Wind Turbine.
%
% EolosDataImporting(filename,delim,ix) imports file with filename as csv
% or txt(tab) file with the delimiter delim (either ',' or '\t').
% ix is used for the size of data (0: Small 1: Large data)
% hr is testing hours for Large data. hr = 0 is used for ix = 0;
% [EdgST t] = EolosDataImporting(filename,delim,ix)
% returns the edgewise strains of three blades at the same location.
% EdgST is [EdgST1 EdgST2 EdgST3] (Watch out the dimension)
%
% Dongwon Lim
% Created: 11/14/2013
% Modified: 05/23/2014

if ix          % 0: Small 1: Large data
    block_size = 6*20*60*60;      % 6 hours => 4 segs for 24 hours
    format = '%s %d %d %f32 %f32 %f32 %f32 %f32 %f32 %f32 %f32 %f32 ...
              %f32 ...
              %f32 %f32 %f32 %f32 %f32 %f32 %f32';
    file_id = fopen(filename);
    id=1;
    C_header = textscan(file_id, '%s', 33,'delimiter',delim);      %% 33 ...
                columns
%    hr = 8*24;
    nwindow = hr*(20*60*60)/block_size;
    t = 0.05:0.05:hr*60*60-0.05;
%    sD = 1.0120;                % Damage factor to the strain, gD = 2*sD
    sD = 1;
    EdgST1 = zeros(1,hr*60*60*20);
    EdgST2 = zeros(1,hr*60*60*20);
    EdgST3 = zeros(1,hr*60*60*20);
    for i = 1:nwindow
        segarray = textscan(file_id, format, block_size,'delimiter',delim);
        Data = [segarray{9} segarray{19} segarray{29}];
    end
end

```

```

BldST = EolosDatafilter(Data,20);
% Without filtering
%   BldST = [Data1(3001:end)'; Data2(3001:end)'; Data3(3001:end)'];
BldST(3,:) = sD*BldST(3,:);

EdgST1(1,1+(block_size-3000)*(id-1):(block_size-3000)*id) = ...
    BldST(1,:);
EdgST2(1,1+(block_size-3000)*(id-1):(block_size-3000)*id) = ...
    BldST(2,:);
EdgST3(1,1+(block_size-3000)*(id-1):(block_size-3000)*id) = ...
    BldST(3,:);
%   Time(1,1+block_size*(id-1):10+block_size*(id-1)) = segarray{8};
id = id + 1;
if rem(id*block_size,20*60*60) == 0
    disp(id*block_size/(20*60*60));
end
end
fclose(file_id);
else
A = importdata(filename,delim,1);
EdgST1 = A.data(:,8)';
EdgST2 = A.data(:,18)';
EdgST3 = A.data(:,28)';
t = 0:0.05:0.05*length(A.data)-0.05;
end

%% Return
EdgST = [EdgST1; EdgST2; EdgST3];

```

D.6 Strain Data Error Correction

```

function BldST = EolosDatafilter(Data,samplef)
% EolosDatafilter(Data1,Data2,Data3) corrects Eolos Strain Data
% errors: bias, scaling, chattering noise, drifting, salt and pepper noise
% Errors are corrected by demeaning for the bias error; descaling;
% applying low pass filter for chattering and high pass filter for
% drifting; and interpolation for salt/pepper noise.
%
% Dongwon Lim
% Modified 02/22/2014

% For bandpass filter design from 0.01 to 10Hz
% B = [0 0.3934 -0.3934];
% A = [1 -1.6062 0.6062];

    EdgST1t = Data(:,1); EdgST2t = Data(:,2); EdgST3t = Data(:,3);
% Correcting Sensor Errors
    % Remove drop-outs and interpolate for three strains
    NANIx1 = find(abs(EdgST1t) > 5000);
    NANIx2 = find(abs(EdgST2t) > 5000);
    NANIx3 = find(abs(EdgST3t) > 5000);
    ko = (0:length(Data)-1)'; kn1 = ko; kn2 = ko; kn3 = ko;
    EdgST1t(NANIx1) = [];    kn1(NANIx1) = [];
    EdgST2t(NANIx2) = [];    kn2(NANIx2) = [];
    EdgST3t(NANIx3) = [];    kn3(NANIx3) = [];
    EdgST1 = interp1(kn1,EdgST1t,ko);
    EdgST2 = interp1(kn2,EdgST2t,ko);
    EdgST3 = interp1(kn3,EdgST3t,ko);
    % Find nan entries
    K1 = any(isnan(EdgST1),2);
    K2 = any(isnan(EdgST2),2);
    K3 = any(isnan(EdgST3),2);
    K = or(K1,K2);
    K = or(K,K3);
    % Remove common nan entries
    EdgST1(K) = [];
    EdgST2(K) = [];

```

```

EdgST3(K) = [];

if samplef == 20
    % Apply Low-pass filter
    EdgST1 = filter(0.05/0.1, [1 0.05/0.1-1], EdgST1);
    EdgST2 = filter(0.05/0.1, [1 0.05/0.1-1], EdgST2);
    EdgST3 = filter(0.05/0.1, [1 0.05/0.1-1], EdgST3);
    % Apply High-pass filter
    EdgST1 = filter([1 -1], [1 0.05/100-1], EdgST1); % 20Hz Sampling
    EdgST2 = filter([1 -1], [1 0.05/100-1], EdgST2);
    EdgST3 = filter([1 -1], [1 0.05/100-1], EdgST3);

    % Cutting out first 3000 time steps
    EdgST1 = EdgST1(3001:end);
    EdgST2 = EdgST2(3001:end);
    EdgST3 = EdgST3(3001:end);
else
    EdgST1 = filter([1 -1], [1 1/100-1], EdgST1); % 1Hz Sampling Freq.
    EdgST2 = filter([1 -1], [1 1/100-1], EdgST2);
    EdgST3 = filter([1 -1], [1 1/100-1], EdgST3);

    % Cutting out first 3000/20 =150 time steps
    EdgST1 = EdgST1(151:end);
    EdgST2 = EdgST2(151:end);
    EdgST3 = EdgST3(151:end);
end

% % Apply Band-pass filter from 0.01Hz to 10Hz
% EdgST1 = filter(B, A, EdgST1);
% EdgST2 = filter(B, A, EdgST2);
% EdgST3 = filter(B, A, EdgST3);
% Find strain rate for each blade
dB1 = diff(EdgST1);
dB2 = diff(EdgST2);
dB3 = diff(EdgST3);
dE1 = norm(dB1);dE2 = norm(dB2);dE3 = norm(dB3);

% Find where there is oscillation
ix1 = find(abs(dB1)>1);ix2 = find(abs(dB2)>1);ix3 = find(abs(dB3)>1);
% Demean to fix bias error

```

```

mEdgST1 = mean(EdgST1(ix1));
mEdgST2 = mean(EdgST2(ix2));
mEdgST3 = mean(EdgST3(ix3));
%   BldST = BldST - mean(BldST(:,ix),2)*ones(1,length(BldST));      ...
% demean (Bias)
% Desacle to fix scale error
%   if i == 1
%       E1 = norm(EdgST1(ix1)-mEdgST1); E2 = norm(EdgST2(ix2)-mEdgST2); ...
%       E3 = norm(EdgST3(ix3)-mEdgST3);
%   end
EdgST1=EdgST1-mEdgST1;EdgST2=EdgST2-mEdgST2;EdgST3=EdgST3-mEdgST3;
% Final signal for blade strains
%   BldST = [EdgST1'; EdgST2'; EdgST3']*10^-6;
%   BldST = [EdgST1'*E1/E1; EdgST2'*E1/E2; EdgST3'*E1/E3*0.989]*10^-6;
BldST = [EdgST1'*E1/E1; EdgST2'*E1/E2; EdgST3'*E1/E3]*10^-6;

end

```

D.7 Find Strain Residual Variance

```

% Find Pk for Eolos Data
% Main objective of this script is to find the variance of the strain
% Energy Residue of two blades i and j.
% Input: Eolos large strain data is divided into small segments and
%       process one segment by one at each time.
% Output: Estimated strain energy residue for small inspection time
%       window. The collected (processed data) will be collected
%       and processed for calculating the variance.
%
% Dongwon Lim 2014/02/04

clear all; close all;

% Import data for the size of a given segment
filename = 'D:\Eolos2013\Strain0501.0510.csv';
delim = ',';
% block_size = 3*20*60*60;      % 3 hours => 8 segs for 24 hours
block_size = 6*20*60*60;      % 6 hours => 4 segs for 24 hours
format = '%s %d %d %f32 %f32 %f32 %f32 %f32 %f32 %f32 %f32 %f32 ...
         %f32 ...
         %f32 %f32 %f32 %f32 %f32 %f32';
file_id = fopen(filename);
id=1;
C_header = textscan(file_id, '%s', 33, 'delimiter', delim);      %% 33 columns
hr = 10*24;
nwindow = hr*(20*60*60)/block_size;
t = 0.05:0.05:hr*60*60-0.05;
k = 3001:block_size;
SE1 = zeros(1,block_size-3000);
SE2 = zeros(1,block_size-3000);
SE3 = zeros(1,block_size-3000);
Keh = 0.004*117.60*30.34; % [mm3] eta = 7% EH size = 0.38 mm3 E=30GPa
% sD = 1.0120;          % Damage factor to the strain, gD = 2*sD
sD = 1;
W = 100;
% Threshold

```

```

PFP = 1/(20*365*24/6);
T1 = abs(norminv(sqrt(PFP/3)/2,0,sqrt(k)*0.0444318));

%%
disp('The strength ratio between blade strains 1,3');
for i = 1:nwindow
    segarray = textscan(file_id, format, block_size, 'delimiter', delim);
    Data = [segarray{9} segarray{19} segarray{29}];
    BldST = EolosDatafilter(Data,20);
    BldST(3,:) = sD*BldST(3,:);
    % Energy Calculation Pulse generation
    EW = SdataImport(BldST);
    % Three cases
    r1 = EW(1,:) - EW(2,:); r2 = EW(3,:) - EW(2,:); r3 = EW(3,:) - EW(1,:);

    k1 = 1:length(r1); k2 = 1:length(r2); k3 = 1:length(r3);
    dT = PulseCal(BldST,Keh,W);
    EWtilde = EHest(dT,W,k);
    nx1 = EWtilde(1,:) - EWtilde(2,:);
    Plotting for checking
    if i == 10 || i == 11
        figure(1); ...
            plot(k/20,Data1(3001:end),k/20,Data2(3001:end),k/20,Data3(3001:end));
        figure(2); plot(k/20,EdgST1,k/20,EdgST2,k/20,EdgST3);
        figure(3); ...
            plot(k/72e3,BldST(1,:)*1e6,k/72e3,BldST(2,:)*1e6,k/72e3,BldST(3,:)*1e6);
        xlabel('Time (hr)'); ylabel('Strain (\mu-\epsilon)');
        figure(4); plot(k(2:end)/20,dB1,k(2:end)/20,dB2,k(2:end)/20,dB3);
        figure(5); plot(k/20,EW(1,:),k/20,EW(3,:));
        xlabel('Time (sec)'); ylabel('Strain (\mu-\epsilon)');
        title('Strain (\mu-\epsilon)');
        figure(1); subplot(211); plot(k/20,Data3(3001:end)-mEdgST3);
        ylabel('Before low-pass filter');
        figure(1); subplot(212); plot(k/20,EdgST3);
        ylabel('After low-pass filter');
        xlabel('Time (sec)');
    end

    figure(7);

```

```

plot(k1/72e3,r1,k2/72e3,r2,k3/72e3,r3),grid;
axis([k(1)/72e3 k(end)/72e3 -150 150]); hold on;
plot(k/72e3,T1,'r--',k/72e3,-T1,'r--','LineWidth',2);
hold off;
title(['Energy Diff at ' num2str(i) 'th time window']);
text(k(end)/72e3,T1(end),'Avg');
xlabel('Time (hr)'); ylabel('\deltaW(k) [\muJ]');
% legend('W_1-W_2','W_3-W_2','W_3-W_1');

B1 = diff(EW(1,:));
B2 = diff(EW(2,:));
B3 = diff(EW(3,:));
mBk1 = mean(B1); mBk2 = mean(B2); mBk3 = mean(B3);
disp(['dE Avg at Blade1,2,3 of ' num2str(i) 'th time, ' ...
      num2str(mBk1) ', ' num2str(mBk2) ', ' num2str(mBk3)]);

SE1(i,1:length(r1)) = r1; % Accumulating estimated Strain ...
      Energy(SE) into SE Matrix
SE2(i,1:length(r2)) = r2; % Accumulating estimated Strain ...
      Energy(SE) into SE Matrix
SE3(i,1:length(r3)) = r3; % Accumulating estimated Strain ...
      Energy(SE) into SE Matrix
pause(0.2);
end

[nr,nc] = size(SE1);
fclose(file_id);
%% Statistics

% Find the variance
for i=1:block_size-3000
    sigN(i) = nanstd(SE1(:,i));
end

% Find the mean
muN = nanmean(SE1(:,end));
muavg = muN/block_size;

figure(26); plot(sigN);
Nsigmax = max(sigN);

```

```

sig = Nsigmax/sqrt(block_size);
xlabel('Time step [-]');ylabel('STD of \deltaW');
hold on;
plot(k,sqrt(k)*sig,'r--');
hold off;
disp(['The variance for Harvested Energy Residue time increment: ' ...
      num2str(sig)]);
% disp('Theoretical ');
% disp(sqrt(N)*sig0);
disp(['The mean for Harvested Energy Residue time increment: ' ...
      num2str(muavg)]);

%% Post-processing
figure(35);
% sig = 0.05;
% PFP = 1.929e-8;      %[1.929e-8 1.586e-9 5.285e-10];      % 1/30days ...
      1/1year 1/3years
% T = abs(norminv(PFP/2,0,sqrt(k)*sig));

for i = 1:length(x)
    hold on;
    title(['Energy Diff upto ' num2str(i) 'th time window']);
    plot(k/72e3,SE1(x(i),:));
    text(k(end)/72e3,SE1(x(i),end),num2str(i));
    hold off;
    axis([k(1)/72e3 k(end)/72e3 -1.47*sig*sqrt(k(end)) ...
          1.47*sig*sqrt(k(end))]);
    pause(0.1);
end

grid on;
hold on;      ...
    plot(k/72e3,sig*sqrt(k),'r--',k/72e3,-sig*sqrt(k),'r--','Linewidth',2.5);
hold off;
xlabel('Time (hr)');ylabel('\deltaW_c(k)=W_3-W_1 (\muJ)');

```

D.8 Synthetic Damage Simulation for Eolos Data

```

% Eolos Data Simulation with a synthetic damage, gD
% Main objective of this script is to find detection time for
% specific damage size gD
% Input: Eolos large strain data is divided into small segments and
%         process one segment by one at each time.
% Output: Estimated strain energy residual for small inspection time
%         window. The collected (processed data) will be collected
%         and processed for calculating the variance.
%
% Dongwon Lim 2014/03/13

clear all; close all;

%% Import data for the size of a given segment
filename = 'd:\2013\BladeStrain20130501_20130510.csv';
delim = ',';
% block_size = 3*20*60*60;      % 3 hours
block_size = 9*20*60*60;
format = '%s %d %d %f32 %f32 %f32 %f32 %f32 %f32 %f32 %f32 %f32 ...
         %f32 ...
         %f32 %f32 %f32 %f32 %f32 %f32';
file_id = fopen(filename);
id=1;
C_header = textscan(file_id, '%s', 33,'delimiter',delim);      %% 33 columns
hr = 8*24;
nwindow = hr*(20*60*60)/block_size;
t = 0.05:0.05:hr*60*60-0.05;
k = 3001:block_size;
SE = zeros(1,block_size-3000);
Keh = 0.004*117.60*30.34; % [mm3] eta = 7% EH size = 0.38 mm3 E=30GPa
gD = [1.50    1.75    2.00    2.25    2.50]*0.01;
W = 100;
% Threshold
PFP = 1.929e-8;      %[1.929e-8 1.586e-9 5.285e-10];      % 1/30days ...
         1/1year 1/3years
% Tl = abs(norminv(PFP/2,0,sqrt(k)*0.041304));

```

```

T2 = abs(norminv(PFP/2,0,sqrt(k)*0.05355));      % May
% T3 = abs(norminv(PFP/2,0,sqrt(k)*0.02958));
% Detectible Damage Size
mBk = 0.01;
PTP = 0.9;
X2 = norminv(1-PTP(1),0,sqrt(k)*0.05355);
fdam2 = (T2 + 0 - X2)./k/mBk;
% BldST = zeros(3,(block_size-3000)*nwindow);
%% Data Loading
tic
%     figure(7); grid on;     hold on;

for i = 1: nwindow
    segarray = textscan(file_id, format, block_size, 'delimiter', delim);
    Data1 = segarray{9};
    Data2 = segarray{19};
    Data3 = segarray{29};
    BldST = EolosDatafilter(i,Data1,Data2,Data3,block_size);
    BldST(3,:) = (1+gD(3))*BldST(3,:);
    EW = EHCa1(BldST,Keh,1);      % [uJ]
    nx1 = EW(1,:) - EW(2,:); nx2 = EW(3,:) - EW(2,:); nx3 = EW(3,:) - ...
        EW(1,:);
    k_dtc1 = min(find(nx1>T2));
    k_dtc2 = min(find(nx2>T2));
    k_dtc3 = min(find(nx3>T2));
%     plot(k/72e3,nx1,k/72e3,nx2,k/72e3,nx3);
%     axis([k(1)/72e3 k(end)/72e3 -350 350]);
%     plot(k/72e3,T2,'r--',k/72e3,-T2,'r--','LineWidth',2);

    disp([num2str(i) 'th window: ' num2str(k_dtc1/72e3) ', ' ...
        num2str(k_dtc2/72e3) ', ' num2str(k_dtc3/72e3)])
end
toc
fclose(file_id);

% Three cases
figure(7);     hold on;
plot(k/72e3,nx1,k/72e3,nx2,k/72e3,nx3),grid;
axis([k(1)/72e3 k(end)/72e3 -350 350]);

```

```

plot(k/72e3,T1,'r--',k/72e3,-T1,'r--','LineWidth',2);
plot(k/72e3,T2,'r--',k/72e3,-T2,'r--','LineWidth',2);
plot(k/72e3,T3,'r--',k/72e3,-T3,'r--','LineWidth',2);
hold off;
title(['Energy Diff at ' num2str(i) 'th time window']);
text(k(end)/72e3,T1(end),'Avg');
text(k(end)/72e3,T2(end),'May');
text(k(end)/72e3,T3(end),'Sep');
xlabel('Time (hr)'); ylabel('\deltaW(k) [\muJ]');
% legend('W_1-W_2','W_3-W_2','W_3-W_1');

B3 = diff(EW(3,:));
mBk3 = mean(B3);
disp(['dE Avg at Blade3 of ' num2str(i) 'th time, ' num2str(mBk3)]);

SE(i,:) = nx3; % Accumulating estimated Strain Energy(SE) into SE ...
Matrix
% pause(0.2);
end

[nr,nc] = size(SE);
fclose(file_id);
%% Statistics

% Find the variance
for i=1:block_size-3000
    sigN(i) = nanstd(SE(:,i));
end

% Find the mean
muN = nanmean(SE(:,end));
muavg = muN/block_size;

figure(26); plot(sigN);
Nsigmax = max(sigN);
sig = Nsigmax/sqrt(block_size);
xlabel('Time step [-]');ylabel('STD of \deltaW');
hold on;
plot(k,sqrt(k)*sig,'r--');
hold off;

```

```

disp(['The variance for Harvested Energy Residue time increment: ' ...
      num2str(sig)]);
% disp('Theoretical ');
% disp(sqrt(N)*sig0);
disp(['The mean for Harvested Energy Residue time increment: ' ...
      num2str(muavg)]);

%% Post-processing
figure(35);
% sig = 0.05;
% PFP = 1.929e-8;      %[1.929e-8 1.586e-9 5.285e-10];      % 1/30days ...
      1/1year 1/3years
% T = abs(norminv(PFP/2,0,sqrt(k)*sig));

for i = 1:length(x)
    hold on;
    title(['Energy Diff upto ' num2str(i) 'th time window']);
    plot(k/72e3,SE(x(i),:));
    text(k(end)/72e3,SE(x(i),end),num2str(i));
    hold off;
    axis([k(1)/72e3 k(end)/72e3 -1.47*sig*sqrt(k(end)) ...
          1.47*sig*sqrt(k(end))]);
    pause(0.1);
end

grid on;
hold on;      ...
    plot(k/72e3,sig*sqrt(k),'r--',k/72e3,-sig*sqrt(k),'r--','Linewidth',2.5);
hold off;
xlabel('Time (hr)');ylabel('\deltaW_c(k)=W_3-W_1 (\muJ)');

```

D.9 SHM Design by Threshold and Decision Time

```

% Monitoring System Design by Threshold and Time wait
% Dongwon Lim
% 2013/09/25
% Modified: 2014/08/10

clear all;% close all;
sizeF = 1;
sig = sqrt(sizeF)*[0.102/2 0.102 0.102*2];
B = sizeF*0.0104;

PFP = 50/(20*365);
k = linspace(12,240)*24*60*60*20;
T = zeros(length(sig),length(k));
for i = 1 :length(sig)
    T(i,:) = abs(norminv(sqrt(PFP/3)/2,0,sqrt(k)*sig(i)));
end
figure(1);
semilogx(k,T(1,:), '- ',k,T(2,:), '-- ',k,T(3,:), '-.', 'LineWidth',2.5),grid
xlabel('Time (step)'); ylabel('Threshold [\muJ]');
legend('1\sigma', '2\sigma', '3\sigma');
axis([k(1) k(end) 0 max(max(T))]);

PTP = [0.9 0.99 0.9999]; % 80% 99% 99.99%
fdam = zeros(length(PTP),length(k));
T = abs(norminv(sqrt(PFP/3)/2,0,sqrt(k)*sig(2)));
for j = 1 : length(PTP)
    X = norminv(1-PTP(j),0,sqrt(k)*sig(2));
    % Misc = normcdf(X-2*T,0,sqrt(k)*sig);
    % fdam(3*(i-1)+j,:) = (T(i,:) - X)./k/(B); % For strain ...
    energy factor
    fdam(j,:) = (T - X)./k/B; % For damage factor
end

figure(22);
plot(fdam(1,:),k/72e3/24,fdam(2,:),k/72e3/24,fdam(3,:),k/72e3/24);
xlabel('Degradation Parameter, g_D [-]'); ylabel('Decision Time [day]');

```

```
legend([num2str(PTP(1)*100) '% P- $\tau$ '],[num2str(PTP(2)*100) '% ...  
P- $\tau$ '],[num2str(PTP(3)*100) '% P- $\tau$ ']);  
h=gca;  
set(h,'XTick',[0.0008 0.0017 0.0026 0.0035])  
axis([min(fdam(1,:)) max(fdam(1,:)) 0 k(end)/72e3/24]);  
figure(22); hold on;  
plot([0.0017 0.0035],[51 13],'ko'); hold off;  
annotation('textarrow',[1.5 1.7]/3.5,[120 170]/600,'string','g-D = ...  
0.0017\\ \tau = 180 days','LineWidth',2)
```